Rochester Institute of Technology
RIT Scholar Works

Theses | Thesis/Dissertation Collections

8-14-2012

A Signal processing approach for preprocessing and 3d analysis of airborne small-footprint full waveform lidar data

Jiaying Wu

Follow this and additional works at: http://scholarworks.rit.edu/theses

Recommended Citation
Wu, Jiaying, "A Signal processing approach for preprocessing and 3d analysis of airborne small-footprint full waveform lidar data" (2012). Thesis. Rochester Institute of Technology. Accessed from

This Dissertation is brought to you for free and open access by the Thesis/Dissertation Collections at RIT Scholar Works. It has been accepted for inclusion in Theses by an authorized administrator of RIT Scholar Works. For more information, please contact ritscholarworks@rit.edu.

A SIGNAL PROCESSING APPROACH FOR PREPROCESSING AND 3D ANALYSIS OF AIRBORNE SMALL-FOOTPRINT FULL WAVEFORM LIDAR DATA

by

Jiaying Wu

B.S. University of Shanghai for Science and Technology

(2006)

A dissertation submitted in partial fulfillment of
requirements for the degree of Ph.D.
in the Chester F. Carlson Center for Imaging Science
of the College of Science
Rochester Institute of Technology

August 14, 2012

Signature of author _____

Accepted by _____
Coordinator, Ph.D. Degree Program Date

CHESTER F. CARLSON
CENTER FOR IMAGING SCIENCE
COLLEGE OF SCIENCE
ROCHESTER INSTITUTE OF TECHNOLOGY
ROCHESTER, NEW YORK

CERTIFICATE OF APPROVAL

Ph.D. DEGREE DISSERTATION

The Ph.D. Degree Dissertation of Jiaying Wu
has been examined and approved by
the dissertation committee as satisfactory for the
dissertation requirement for the
Ph.D. degree in Imaging Science

Dr. Jan van Aardt, Thesis Advisor	Date
Dr. John Kerekes	Date
Dr. Harvey Rhody	Date
Dr. Vinny Amuso	Date

DISSERTATION RELEASE PERMISSION
ROCHESTER INSTITUTE OF TECHNOLOGY
COLLEGE OF SCIENCE
CHESTER F. CARLSON
CENTER FOR IMAGING SCIENCE

Title of Dissertation:

A Signal Processing Approach For Preprocessing and 3D Analysis of Airborne Small-Footprint Full Waveform LiDAR Data

I, Jiaying Wu, hereby grant permission to Wallace Memorial Library of R.I.T. to reproduce my thesis in whole or in part. Any reproduction will not be for commercial use or profit.

Signature: _____

Date: _____

A SIGNAL PROCESSING APPROACH FOR PREPROCESSING AND 3D ANALYSIS OF AIRBORNE SMALL-FOOTPRINT FULL WAVEFORM LIDAR DATA

by
Jiaying Wu

A dissertation submitted in fulfillment of
requirements for the degree of Ph.D.
in the Chester F. Carlson Center for Imaging
Science
of the College of Science
Rochester Institute of Technology

Abstract

The extraction of structural object metrics from a next generation remote sensing modality, namely waveform light detection and ranging (LiDAR), has garnered increasing interest from the remote sensing research community. However, a number of challenges need to be addressed before structural or 3D vegetation modeling can be accomplished. These include proper processing of complex, often off-nadir waveform signals, extraction of relevant waveform parameters that relate to vegetation structure, and from a quantitative modeling perspective, 3D rendering of a vegetation object from LiDAR waveforms. Three corresponding, broad research objectives therefore were addressed in this dissertation.

Firstly, the raw incoming LiDAR waveform typically exhibits a stretched, misaligned, and relatively distorted character. A robust signal preprocessing chain for LiDAR waveform calibration, which includes noise reduction, deconvolution, waveform registration, and angular rectification is presented. This preprocessing chain was validated using both simulated waveform data of high fidelity 3D vegetation models, which were derived via the Digital Imaging and Remote Sensing Image Generation (DIRSIG) modeling environment and real small-footprint waveform LiDAR data, collected by the Carnegie Airborne Observatory (CAO) in a savanna region of South Africa. Results showed that the preprocessing approach significantly increased our ability

to recover the temporal signal resolution, and resulted in improved waveform-based vegetation biomass estimation.

Secondly, a model for savanna vegetation biomass was derived using the resultant processed waveform data and by decoding the waveform in terms of feature metrics for woody and herbaceous biomass estimation. The results confirmed that small-footprint waveform LiDAR data have significant potential in the case of this application.

Finally, a 3D image clustering-based waveform LiDAR inversion model was developed for 1st order (principal branch level) 3D tree reconstruction in both leaf-off and leaf-on conditions. These outputs not only contribute to the visualization of complex tree structures, but also benefit efforts related to the quantification of vegetation structure for natural resource applications from waveform LiDAR data.

ACKNOWLEDGEMENTS

First of all I want to thank my advisor Dr. Jan van Aardt. It has been an honor to be his first Ph.D. student. It would not have been possible to write this doctoral thesis without his excellent guidance and support on both an academic and a personal level. I appreciate all his contributions in terms of time, ideas, and funding to make my Ph.D. experience productive and stimulating.

I would also like to acknowledge the financial, academic, and technical support of my department, the Chester F. Carlson Center for Imaging Science, Rochester Institute of Technology towards completing my Ph.D. research, travel, publishing, etc.

This research would not have been possible without the support from Carnegie Institution for Science, Stanford, CA. I am most grateful to my thesis co-advisor, Dr. Gregory P. Asner, for his inputs to the vegetation biomass study, and his extraordinary contribution in building up the Carnegie Airborne Observatory, which is funded by the W.M. Keck Foundation and William Hearst III. Dr. Asner also hosted me at their lab in Stanford, CA for the academic collaboration twice during my Ph.D study. Together with Mr. Ty Kennedy-Bowdoin, Mr. Dave Knapp and Mr. Aravindh Balaji, he provided the airborne waveform LiDAR data and technical support, for which I am extremely grateful. Also, my thanks goes to Dr. Konrad Wessels, Dr. Renaud Mathieu (Council for Scientific and Industrial Research), and Dr. Barend Erasmus (University of the Witwatersrand) for their field data collection support.

I would also like to thank Dr. Michael Long (RIT) for his inputs during discussions on statistical analysis, Dr. Harvey Rhody for his excellent instruction on signal processing, and Dr. John Kerekes for his advising on image processing algorithms.

I want to thank my classmates, also friends, David Kelbe, Paul Romanczyk, Joseph McGlinchy, and Diane Sarrazin, and Dr. Kerry Cawse-Nicholson in our waveform LiDAR study group. I feel so lucky to work with such smart and kind people. Most of my inspirations originate from our team work, discussions, and brainstorming, where we share ideas with each other.

Lastly, I would like to thank my family for all their love and encouragement, especially my parents who raised and supported me in all my pursuits. Thank you all.

Contents

Abstract iv

Acknowledgements vi

List of Figures ix

List of Tables xiv

1 Introduction 1
1.1 LiDAR system and technology …….. 4
1.1.1 Discrete return LiDAR …….. 6
1.1.2 Full-waveform LiDAR …….. 7
1.2 LiDAR waveform data analysis …….. 10
1.2.1 LiDAR radiative transfer modeling …….. 10
1.2.2 Waveform LiDAR preprocessing techniques …….. 11
1.2.3 LiDAR 3D processing for object reconstruction ……..... 17
1.3 Vegetation Applications of waveform LiDAR technology …….. 20

2 LiDAR Waveform preprocessing chain development 23
2.1 Methods …… 24
2.1.1 Available data ……..…. 24
2.1.1.1 Real waveform and associated field data ……. 24
2.1.1.2 Simulated LiDAR waveform data …..……. 27
2.1.2 Noise reduction ……. 29
2.1.3 Deconvolution ……..……. 32
2.1.3.1 Recovering the true cross-section of vegetation ……..…. 32
2.1.3.2 Differentiating herbaceous biomass ……. 36
2.1.4 Waveform-to-ground registration ……..…. 38
2.1.5 Angular rectification ……..…. 40
2.1.6 Approach to preprocessing chain performance validation ……...…. 43
2.2 Results and discussion ……..…. 47
2.2.1 Quantitative comparison of deconvolution algorithms ……..…..... 47
2.2.2 Preprocessing chain validation ……..…. 59
2.3 Conclusions ……..……..…. 68

3 Waveform feature metrics extraction for biomass modeling 71
3.1 Methods ……...……..…. 72
3.1.1 Metrics for woody biomass modeling ……..…. 72
3.1.2 Metrics for herbaceous biomass modeling ……...…. 75
3.2 Results and discussion ……..…. 77
3.3 Conclusions ……..……..…. 81

4 3D tree reconstruction using waveform LiDAR 83
4.1 Methods ……..……. 84
4.1.1 Waveform LiDAR clustering ……..……..... 84
4.1.2 Stem and branches reconstruction ……..……. 86
4.2 Results and discussion ……..……..... 90
4.2.1 Leaf-off scenario ……..……. 90
4.2.2 Leaf-on scenario ……..……..……. 95
4.3 Conclusions ……..……..... 101

5 Conclusions 103

A. Appendix 106
A.1 DIRSIG waveform simulation model .....……..... 106
A.2 DBSCAN .....……..... 110
A.3 Waveform LiDAR processing GUI Tools .....……..... 111
A.4 Matlab source code .....……..... 114

List of References 120

List of Figures

1.1 An overview of the research objectives …….. 3

1.2 Illustration of the discrete return LiDAR signal ……...…….. 7

1.3 Illustration of the full-waveform LiDAR signal ……..... 9

1.4 An example of 3D reconstruction of tree branches based on Gorte and Pfeifer's [14] voxel approach ……..……..... 18

1.5 Probabilistic 3D reconstruction of branches, proposed by Binney and Sukhatme . 18

1.6 3D tree reconstruction proposed by Cote *et al.* [35] …….……...……..... 19

1.7 (a) Typical bimodal waveform. (b) Relationship between field measurements and estimates of maximum canopy height from waveform parameters [36] …..... 20

1.8 Metrics derived from synthetic large-footprint LiDAR waveforms [41] …..... 22

2.1 A flowchart of the waveform LiDAR preprocessing chain ……..... 24

2.2 The study area and associated land use gradient in South Africa ……..... 25

2.3 CAO Alpha system with the ALTM 3100 waveform LiDAR system ……..... 26

2.4 Site-level sampling design with 36 plots/site ……..... 26

2.5 An example of a virtual scene for generating simulated waveform LiDAR … 27

2.6 Histogram of the zenith (a) and azimuth (b) angle distribution based on real waveform LiDAR data collected by CAO ……..... 29

2.7 Illustration of the waveform noise filtering: (a) Real (raw) waveform data collected by the Carnegie Airborne Observatory system and (b) the smoothed waveform following frequency-based noise filtering. Note: a negative noise level shift of 11 units was applied to the raw signal first to avoid the potential frequency leakage caused by the sharp edge at the inflection point (signal on/off) ……..... 31

2.8 A typical frequency representation of a waveform signal. A cut-off frequency threshold of 20GHz was selected based on visual assessment of filtering results; any frequency component above 20GHz was attributed to noise and set to zero. Simulated 3D trees used for waveform simulation and deconvolution assessment ……..……..……..……..... 31

2.9 Simulated 3D trees used for waveform simulation and deconvolution assessment.35

2.10 Workflow of herbaceous biomass classification algorithm …….…..... 36

2.11 An example of a 3D grass patch (the different herbaceous biomass levels were simulated by scaling the relative size of the grass facet while keeping the patch area of 100m^2 constant) ……..……..... 38
2.12 Illustration of the waveform registration principles ……..... 40
2.13 Illustration of a waveform angular vector map based on CAO data collected in a savanna area, South Africa; note the displacement of less than one pixel size (blue) and displacement larger than one pixel size (red). The direction of the vector indicates the azimuth angle and the length is equal the level of waveform displacement ($r_{projection}$) in this angular vector map ……..……..... 41
2.14 An illustration of the gridding process for registered waveform time bins, where (a) shows an example of an off-nadir waveform, (b) shows the vertical sampling plane, and (c) represents the time bins associated with the same absolute height above sea level ……..……..... 43
2.15 Natural neighbor interpolation. Figure taken from the Wikipedia entry on natural neighbor interpolation [52] ……..……..... 43
2.16 Illustration of spectral angle, as calculated using the spectral angle mapper (SAM) approach. Note: only three bands are shown in this example; this metric can be applied to multi-dimensional data ……...….……..... 45
2.17 An illustration of the deconvolved waveforms for an outgoing pulse width of 8ns: RL (a), WF (b), and NNLA (c) ……..……...……..... 49
2.18 A 3D representation of the waveform LiDAR for tree 6 and all deconvolution approaches at 8ns and 16ns outgoing pulse widths ……....……..... 50
2.19 Results of the RMSE comparison for outgoing pulse width 8ns (a) and 16ns (b) ……...……..…….……..... 52
2.20 Point clouds extracted from the local peaks of the waveforms (Tree 5). The point clouds are colored according to the intensity. (a) Extracted from waveform using 2ns outgoing pulse width, (b) Extracted from raw waveform using 8ns pulse width, (c) Extracted from deconvolved waveforms (RL), (d), Matched points between (a) and (c) ……..…….……..... 53
2.21 False discovery rate vs sensitivity for 8ns (a) and 16ns (b) outgoing pulse widths, with raw (black), RL (red), WF (green), and NNLS (blue) waveforms ..…..... 54

2.22 Simulated waveforms from grass patches: (a) before deconvolution, and (b) after deconvolution. Herbaceous biomass ratios from patch 1 to 5 were 0.2^3: 0.4^3: 0.6^3: 0.8^3: 1. The plots are based on the RL deconvolution algorithm with an outgoing pulse width equal to 8ns ……..……....…..... 56

2.23 Plot of the normalized cumulative sum of the eigenvalues for the simulated waveforms from grass patches; (b) Eigenvectors associated with the four largest eigenvalues in descending order ……..……....…..... 57

2.24 (a) Projection on the 1st eigenvector vs. projection on the 2nd eigenvector. (b) Histogram of the projection on the 1st eigenvector ……..……....…..... 58

2.25 Comparison of the classification accuracy for no deconvolution and the three deconvolution algorithms in question ……..……....…..... 59

2.26 A 3D representation of the voxelized waveforms. (a): Raw waveform (8ns pulse width, zenith=5°). (b): Truth waveform (2ns pulse width). (c): Fully processed waveform ….....….….... 61

2.27 Stepwise evaluation of the processing chain performance; 4ns (a), 8ns (b) and 16ns (c) outgoing pulse widths. Raw (Raw data), Nos (Noise Reduction), Dev (Deconvolution), Reg (Registration), Ang (Angular Rectification) …...….... 64

2.28 An illustration of the impact that waveform registration and angular rectification have on the processing of waveform LiDAR signals. The truth waveform (a) is compared to the reconstructed waveform (b) after registration and angular rectification. The various off-nadir waveforms are shown before processing for azimuths 0°, 90°, 180°, and 270°, and a zenith of 10° for all (c,d,e,f) ….... 65

2.29 An example of a waveform LiDAR metric used for woody biomass modeling and the impact of processing steps: (clock-wise, from top left) a panchromatic image of a site within the study area (a), 10-90% duration metric (b), after threshold removal and de-noising (c), deconvolution (d), ground registration and angular rectification (e) ……....…..... 67

2.30 Model R^2 as a function of the waveform processing steps (a). There is a slight decrease at the end of the chain, attributed to interpolation of neighboring waveforms. Model RMSE as a function of waveform processing step (b) 67

2.31 The distribution of allometry-estimated (field-based) woody biomass (kg) for the individual trees used in this study……..…..….....…..... 68
3.1 A graphical representation of the metrics extracted from each LiDAR waveform 72
3.2 3D volumetric waveform visualization at the individual tree level. The presentations show x,y,z coordinates, with waveform intensity color-coded from cool (blue; low) to warm (red; high) ……....…..... 73
3.3 An example of a histogram showing the crown thickness distribution, derived from multiple LiDAR waveforms (0.56 m), for an individual tree canopy …….….... 74
3.4 Modeling the herbaceous biomass by Gaussian decomposition; it was hypothesized that the complexity of the herbaceous layer is correlated to the multiple scattering component ….....…..... 75
3.5 (a) Height, (b) foliar biomass, and (c) woody biomass estimation using waveform LiDAR metrics ……....…..... 78
3.6 Herbaceous biomass estimation using waveform LiDAR-derived metrics …. 80
4.1 (a) 3D tree branches input and associated point clouds extracted from simulated waveform data (b) ……....…..... 84
4.2 An illustration of the DBSCAN algorithm that shows the arbitrary nature of cluster shapes [68] ……....…..... 86
4.3 1st order branch characteristics in terms of L and Θ …..……....…..... 88
4.4 An example of how a first order branch can be reconnected to the stem …..... 89
4.5 Definition of tree azimuth and zenith angle …….…..... 90
4.6 Branch representation using waveform LiDAR data with different intensity thresholds. e.g., all the point clouds intensity are larger >3 while T=3 (this was done based on tree #2) ……..……...….....…..... 91
4.7 A graphical representation of the optimal threshold for clustering ……..... 92
4.8 Results of DBSCAN clustering based on optimal threshold; Different cluster is distinguished by color ….……....…..... 93
4.9 Stem reconstruction for leaf-off case. (a) Leaf-off tree input, (b) reconstructed stem from a side view, (c) reconstructed stem from a top view ……...…..... 93
4.10 1st order branches approximated by cylinders from clusters for a tree model in leaf-off scenario ……...…..... 94

4.11 (a) Leaf-off tree input. (b) Final reconstruction result of the branches for the leaf-off scenario ….…….... 94
4.12 (a) Raw point clouds extract from the waveform, (b) after applying optimal intensity threshold ….....….... 95
4.13 Stem reconstruction for leaf-on condition. (a) Leaf-on tree input, (b) reconstructed stem from a side view, (c) reconstructed stem from a top view ….....….... 95
4.14 1st order branches approximated by cylinders from clusters for a tree model in the leaf-on scenario …….……...…..... 96
4.15 (a) Leaf-on tree input. (b) Final reconstruction result of the branches for the leaf-on scenario.……..….....…….... 97
4.16 Branch reconstruction characterization for leaf-off (a) and leaf-on (b) scenario . 98
4.17 Branch reconstruction results (a) original 3D tree model (leaf-on), (b) original 3D tree model (leaf-off), (c) reconstructed tree branches using waveform simulated from leaf-on tree, (d) quantitative results of 2ns and 4ns pulse width branch reconstruction (leaf-on) accuracy by comparing to the truth data (2ns leaf-off). Note: Azimuth Angle (AA), Title Angle (TA), Normalized Branch Length (BL) 99
A.1 Workflow of waveform LiDAR simulation using DIRSIG …….…..…..... 107
A.2 Outgoing pulses used by CAO system (ALTM 3100EA) ……..…..... 109
A.3 LiDAR_tools main user interface …….……..…..... 111
A.4 LiDAR_tools data viewer …….……..…..... 112
A.5 Waveform LiDAR data viewer …….……..…..... 112
A.6 LiDAR waveform preprocessing window ……...…….……..…..... 113

List of Tables

1.1 Basic LiDAR formula ……...…….. 5

1.2 Specification of six waveform LiDAR systems …….. 9

2.1 A description of the LiDAR system configuration ……..…..... 29

2.2 Specifications of the 3D virtual tress used for waveform simulation…...…..... 35

2.3 Statistics of the peak detection results …….…..... 54

2.4 Illustration of confusion matrix used for assessing the accuracy of herbaceous biomass classification (based on RL) ….....….... 59

3.1 Correlation coefficients between field data (blue) and waveform-derived metrics (yellow) (D= diameter measured above basal swelling; H=measured height) .. 77

3.2 Correlation coefficients between field data and waveform-derived feature metrics for herbaceous biomass estimation ……..…..... 80

4.1 Quantitative comparison of the branch reconstruction for leaf-off and leaf-on condition, Δ represents difference for each metric ……..... 98

Chapter 1: Introduction

The assessment and monitoring of ecosystem change, such as biomass accumulation, typically involve extensive field data collection. Such data collection typically includes sampling of parameters such as foliar area, stem diameter, tree height, and volume or woody biomass. The acquisition of these data can be expensive and time consuming, while leaving the user with a relatively crude approach when modeling intricate dependent variables, such as woody and foliar biomass, volume, etc. In the recent decades, the application of waveform **Li**ght **D**etection **a**nd **R**anging (LiDAR) [1-3] remote sensing technology in forestry has become an effective approach to facilitate in-field measurement and vegetation structure characterization, especially due to its unique capability of providing the three-dimensional (3D) information. However, the waveform LiDAR signal still presents significant challenges to implementers.

Firstly, since waveform LiDAR is a relatively recent technology, researchers and application specialists still lack knowledge related to the interaction between the illuminated object and resulting waveform. For instance, the efficient processing of these novel waveform LiDAR data, especially in terms of signal processing and modeling aspects, remains inadequately addressed in literature. An example is the raw incoming (received) LiDAR waveform, which typically exhibits a stretched, misaligned, and relatively featureless character. In other words, the LiDAR signal is smeared and the effective temporal (vertical) resolution is decreased – this is hypothesized to be attributed to a fixed time span allocated for detection, the sensor's variable outgoing pulse signal, off-nadir scanning, the receiver impulse response impacts, and system noise. Consequently, such uncalibrated raw waveform data limit the potential use of waveform LiDAR and also affect the accuracy-precision of associated applications, especially when fine-scale 3D measurements of above-ground objects are considered.

Secondly, in terms of the vegetation-specific LiDAR application, most of the current waveform LiDAR systems are restricted to large footprint sizes. For example, the LVIS (Laser Vegetation Imaging Sensor), developed at NASA's Goddard Space Flight Center, has been widely used for vegetation characterization and monitoring [4]. The more recent GLAS (Geoscience Laser Altimeter System) sensor onboard the ICESat (Ice,

Cloud, and land Elevation Satellite) was developed for measuring ice sheet mass balance, cloud, and aerosol heights, as well as land topography and vegetation characteristics [5]. Such waveform-based LiDAR systems are typically of the very large footprint type (usually 1~80m, depending on the flight altitude) and useful in coarse scale ecosystem and biodiversity studies. However, spatially coarse resolutions cannot unravel changes in the land surface at the scale at which certain land or vegetation processes actually occur, e.g., meter-scale tree damage caused by animals, nor can they extract vegetation composition, structure, and function at fine scales [6-7]. Therefore, the small-footprint (e.g., <1m) waveform LiDAR can potentially fill this gap and improve our understanding of the land dynamics at such finer scales.

Finally, 3D tree reconstruction algorithms are based on terrestrial laser scans, taken to imply airborne scanning of terrestrial targets, and have been of significant research interest in both the remote sensing and image processing community for decades. The methods reported in the literature are typically focused on discrete return point cloud datasets [8-9], i.e., a sequence of x, y, z coordinate combinations, instead of taking advantage of the full waveform recording of the entire cross section of a target. Existing 3D reconstruction approaches are furthermore primarily focused on branch with leaf-off reconstruction [10-11] and the challenge of 3D leaf-on tree reconstruction has not been addressed adequately. Therefore, analysis of the waveform LiDAR signal for object reconstruction in the 3D space remains another research goal for future waveform LiDAR usage.

The specific objectives of this study, motivated by these gaps in current waveform LiDAR research, can be defined as follows (the overview for the research is illustrated in Figure 1.1):

(i) Develop waveform preprocessing chain approaches that specifically include:
   a. *Noise filtering*: Smooth the raw waveform signal.
   b. *Waveform deconvolution*: The incoming waveform can be modeled as a convolution process of the outgoing waveform, system impulse response, and the cross section of the illuminated object; the challenge is to retrieve the system-independent target cross section from the incoming waveform.

c. *Waveform registration*: Mapping each time bin in the waveform to its absolute 3D (x,y,z) coordinate.

d. *Nadir-waveform reconstruction*: The typical LiDAR waveform is slightly off-nadir, with certain zenith and azimuth angles relative to the ground, which could make the pixel-based assigned waveform actually cross multiple pixels while interacting with ground-level objects.

(ii) Model woody and herbaceous biomass by decoding the waveform in terms of feature metrics. This step serves as an additional performance validation for the developed waveform preprocessing chain and as an example of a vegetation-specific application of waveform LiDAR.

(iii) Study the relationships between the geometry, radiative properties of the illuminated object, and the waveforms associated with the target by using the Digital Imaging and Remote Sensing Image Generation (DIRSIG) model. This includes an investigation of inverse waveform LiDAR modeling. By characterizing the incoming waveform, we can eventually utilize the waveform information, e.g., shape, mutual relationship to the neighbors, etc., along with signal and image processing approaches to reconstruct the 3D structure of vegetation in terms of stems, branches, and potentially foliage.

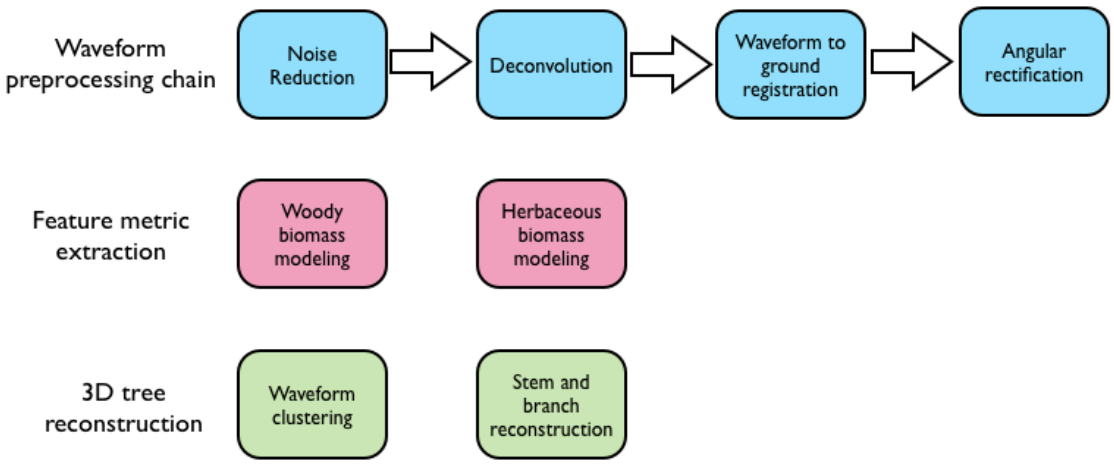

Figure 1.1. An overview of the research objectives

The remainder of Chapter 1 will focus on a comprehensive literature review of the state-of-the-art waveform LiDAR technology in terms of three aspects: (i) Different LiDAR systems, including both discrete return LiDAR and waveform LiDAR systems; (ii) Existing waveform LiDAR data processing approaches; and (iii) Waveform LiDAR-based applications, especially for vegetation studies.

1.1 LiDAR systems and technology

Terrestrial LiDAR technology - whose development can be traced back to the 1970s and 1980s, with an early NASA system and other attempts in the USA - is a well-established optical remote sensing technique for acquiring information about the Earth's topography by measuring the time delay between an emitted and reflected (detected) laser pulse. LiDAR is similar to radar technology, which uses radio waves instead of light. Operational terrestrial LiDAR systems can be divided into two types, namely discrete return (echoes) and waveform LiDAR. Most traditional LiDAR systems measure the first and last return for each emitted laser pulse, while some systems may record up to six returns [1-3].

LiDAR technology has been under rapid development in recent decades. The LiDAR system records the travel time of the return signal - a pulse laser in the green or near–infrared spectral domain - that is reflected or backscattered from the object, then converts the travel time into the distance or range (distance = time × speed of light). With the help of precise kinematic positioning of the platform by global positioning (GPS) and inertial navigation systems (INS), accurate positioning of the object in terms of x,y,z coordinates becomes possible.

Most systems presently operate at flying heights of 1000-2000m above ground. The scan angle is generally $< \pm 30^{o}$, in most cases $< \pm 20^{o}$. The scan frequency usually lies between 2kHz and 25kHz, while pulse frequencies upwards of 150kHz are not unheard of. The actual point sampling density depends on the system and on the trade-off between flying speed, pulse rate, scan angle, and flying height. The geometric sampling

pattern on the ground is pre-determined by the system design; it is not rigidly fixed, as it also depends on the irregular flying path and on the 3D structure of the terrain.

Some basic formulae that apply to laser scanning are listed in Table 1.1 [12]. These formulas are especially helpful in planning and executing a LiDAR mission, as well as determining a LiDAR dataset's properties.

TABLE 1.1. BASIC LIDAR FORMULAE [18]

Characteristic	**Formula**
Range and range resolution	$R = c\frac{t}{2};\ \Delta R = c\frac{\Delta t}{2}$
Vertical resolution (return separation)	$R_{\min} = c\frac{t_{\min}}{2}$
Swath width	$SW = 2h\tan\left(\frac{\theta}{2}\right) = ah$
Along track point spacing	$dx_{along} = \frac{v}{f_{sc}}$
Across track point spacing	$dx_{across} = \frac{SW}{N}$
Point density per unit area	$d = \frac{FnT_s}{A}$

R = Range (m);

c = Speed of light (km/s);

t = Time between sending and receiving a pulse (ns);

SW = Swath width (m);

h = Average flying height over ground (m);

θ = Laser scanning angle (°; FOV);

v = Flying velocity;

$\mathbf{f_{sc}}$ = Scan rate (Hz; scan lines per second);

dx_{along} = Average distance between scan lines, along track (m);

dx_{across} = Average point spacing across track (m);

N = Number of points per scan line;

d = Average point density (points/m^2);

F = Pulse rate (kHz);

n = Number of flying strips to cover area;

$\mathbf{T_s}$ = Flying time per strip (h);

A = Covered area (km^2/h)

1.1.1 Discrete return LiDAR

The physical principle of discrete return LiDAR is based on the emission of short duration laser pulses from an airborne platform at a high temporal repetition rate, after which the two-way runtime to the earth surface and back to the sensor is measured. The reason we call it "discrete" is due to the fact that while the emitted laser pulse hits objects, e.g., canopy, ground, within the footprint path, the multiple returns or echoes appear in the form of discrete (x,y,z) pulse signals. Most discrete return LiDAR systems record the first and last return signals, while more modern designs allow for the detection of up to six returns. Figure 1.2 shows a diagram that illustrates the typical functioning of discrete return LiDAR [13]. We can see that the outgoing laser pulse (red) first interacts with the top of the canopy, after which part of the energy is backscattered by foliage to reach the airborne detector. The remaining signal is transmitted through the canopy and

reflected by the ground. The LiDAR sensor eventually records two individual return signals in this example. These return signals contain the range information of canopy and ground, respectively. By scanning the ground with high pulse rate, the sensor actually samples the ground at a relatively high spatial resolution. The echoes of the outgoing pulses are combined during processing to constitute so-called 3D point clouds with high density, which can be further used to reconstruct the original shape or topography of the ground or an aboveground target.

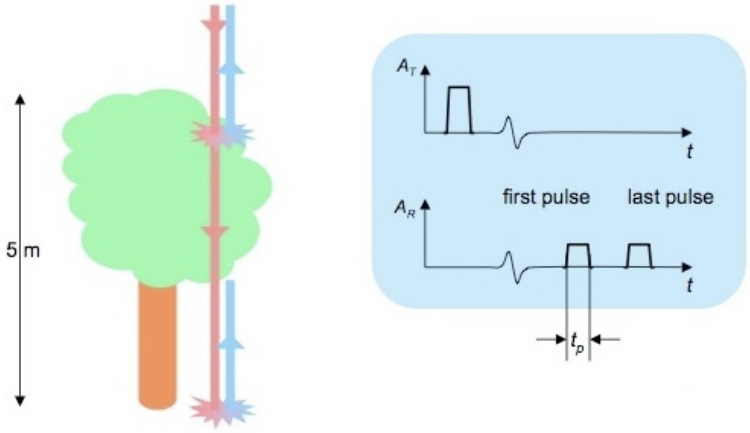

Figure 1.2. Illustration of the discrete return LiDAR signal [19]

1.1.2 Full-waveform LiDAR

The main difference between discrete return and full-waveform LiDAR systems is that waveform LiDAR [14-15] is capable of recording the entire signal of the backscattered laser pulse, followed by digital sampling at high temporal resolution (e.g. 1ns); this is a newer generation of airborne laser scanners developed in the last decades. This advantage over traditional discrete return LiDAR can be used to improve remote sensing applications such as forest volume, biomass estimation, derivation of digital terrain model (DEM), etc. Firstly, unlike the discrete return that usually corresponds to the first and last echoes, the waveform LiDAR actually records all the backscattered signals. It is somewhat analogous to the relationship between multispectral and hyperspectral images, especially in terms of data dimensionality. Waveform data enhance the intensity of cloud points and thus provide much finer structural detail of the target

object in three dimensions. Secondly, additional information associated with the illuminated object can be extracted or decoded from the waveform. This is true because the properties of the waveform, e.g., shape, directly relate to the geometry and radiative properties of the illuminated surface. Consequently, we can see that waveform LiDAR holds much promise for detailed vertical characterization of vegetation structure and improving our management of ecosystem dynamics at fine scales.

We can see from Figure 1.3 [13] that the outgoing laser pulse interacts with the power line, a tree crown, bush, and the ground surface successively, while the entire backscattered signal is digitally sampled by the LiDAR recorder at high temporal resolution (e.g., 1ns). This characteristic amplitude profile of the recorded reflections is usually called a "waveform". The full-waveform LiDAR overcomes certain drawbacks of the conventional discrete return system, such as the issue of a limited number of returns, which results in a lower spatial point density in the discrete case. Detection of structural details, such as the shrub in the understory, also becomes possible when considering waveform systems. Furthermore, the amplitude and the pulse width of the individual returns are available and can be used to derive geometrical and radiative characteristics of the target. Full-waveform LiDAR systems therefore represent the cutting-edge in fine-scale active remote sensing technology for the acquisition of topographic data and mapping of the Earth's surface. As mentioned earlier, the full-waveform LiDAR systems used for large scale ecosystem and biodiversity studies are typically of the large-footprint type (>10m), e.g., the Scanning LIDAR Imager of Canopies by Echo Recovery (SLICER) system built by NASA in 1994, the Laser Vegetation Imaging Sensor (LVIS) developed at NASA's Goddard Space Flight Center, and the more recent Geoscience Laser Altimeter System (GLAS) sensor onboard the Ice, Cloud, and land Elevation Satellite (ICESat) [4-5]. Commercially, the LMS-Q5600 LiDAR system [16], Optech Inc.'s ALTM series systems (www.optech.ca), and the TopEye Mark II system constitute the most common small-footprint airborne waveform-based topographic mapping systems on the market [15]. These novel airborne LiDAR systems can achieve small footprint sizes (< 1m @ 1km flying height) and a high (1ns) sampling rate. Small-footprint data have the benefit of providing spatially concise and explicit returns that enable a tree-specific analysis and management approach. Hence it opens up new

possibilities for in-depth waveform data analysis. To better compare their characteristics, Table 1.2 gives a specification summary of these six waveform LIDAR systems that have been widely used for airborne applications.

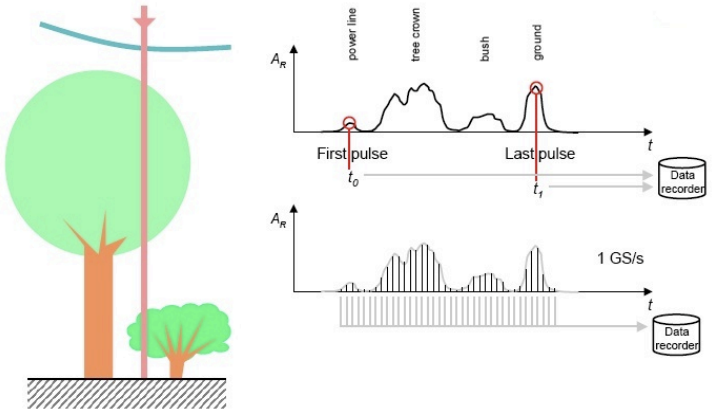

Figure 1.3. Illustration of the full-waveform LiDAR signal

TABLE 1.2 SPECIFICATION OF SIX WAVEFORM LIDAR SYSTEMS [15]

Sensor:	SLICER	LVIS	GLAS	ALTM 3100	MARK II	LMS-Q560
Operational span	1994-1997	1997-	2003-	2004-	2004-	2004-
Platform	Airborne	Airborne	Satellite	Airborne	Airborne	Airborne
Operating altitude	<8 km	<10 km	600 km	<2500 m	<1000 m	<1500 m
Wavelength	1.06um	1.06 um	1.06 um	1.06 um	1.06 um	1.5 um
Pulse width	4ns	10 ns	6ns	8ns	4ns	4ns
Pulse energy	_	5 mJ	75 mJ	<200 uJ	_	8 uJ
Pulse firing rate	75 Hz	100-500Hz	40 HZ	<50 kHz	<50 kHz	<100 kHz
Scan angle range	_	±7º	Fixed at 0º	Up to ±25º	Fixed 20º or 14º	±22.5º
Scan rate	80 Hz	500 Hz	_	<70 Hz	<50 Hz	5-160 Hz
Footprint size	10m@5km	40m@5km	66 m	0.3/0.8 m@ 1km	1 m @ 1km	0.5 m @1km
Laser beam width	2 mrad	8 mrad	0.11-0.17mrad	0.3/0.8 mrad	1 mrad	0.5 mrad
Digitiser	1.35 ns	2 ns	1 ns	1 ns	1 ns	1 ns
Range accuracy	11 cm	30 cm	5-20 cm	1 cm	2-3 cm	2 cm

1.2 LiDAR waveform data analysis

1.2.1 LiDAR radiative transfer modeling

Since LiDAR is based on a similar principle of measurement as that of traditional radar systems, standard LiDAR modeling can be derived from the fundamental radar equation. This equation relates the outgoing (transmitted) LiDAR signal and the return signals, while also taking into account the detector and target characteristics [17-18]. For spatially distributed targets, the return signal (waveform) is a superposition of echoes from scattering surfaces at different ranges, e.g., 1ns or 0.15m vertical resolution in our case. Those scatterers that cannot be discriminated by the sensor due to resolution limitations in the vertical axis, e.g., 0.15m discretization, could also affect the shape of waveform in terms of width, slope, and height characteristics. However, we assume that this effect is relatively minor and focus on the discriminable target for signal modeling. The LiDAR equation can thus be expressed as an integral [19]:

$$P_r(t) = \frac{D^2}{4\pi\lambda^2}\int_0^H \frac{\eta_{sys}\eta_{atm}}{R^4}\cdot P_t\left(t-\frac{2R}{v_g}\right)\cdot \sigma(R)dR \tag{1}$$

where $P_r(t)$ is the received signal as a function of time (waveform), t is the travel time for the transmitted laser pulse, D is the aperture diameter of the receiver optics, $P_t(t)$ is the emitted signal, λ is the wavelength, H is the flying height, R is the distance from the LiDAR system to the target, η_{sys} and η_{atm} are the atmospheric and system transmission factors respectively, v_g is the group velocity of the emitted laser pulse, and $\sigma(t)$ is the cross-section of the illuminated target. Eq.1 can also be seen as the convolution between the system contribution and the environment contribution as shown in Eq.2 [19]:

$$P_r(t) = \frac{D^2}{4\pi\lambda^2 R^4}\underbrace{(P_t * \eta_{sys})(t)}_{\text{System contribution}} * \underbrace{(\eta_{atm} * \sigma)(t)}_{\text{Environment contribution}} \tag{2}$$

This kind of radiative transfer modeling is based on the assumption that only single scattering is taken into account and therefore ignores the contribution of the multiple scattering effect to the return signal.

A more complicated modeling approach that describes multiple scattering events allows for realistic representation of the forest structure, including foliage clumping and gaps, and simulates off-nadir and multi-angular observations, the latter which was proposed based on time-dependent stochastic radiative transfer (RT) theory [20]. The model simulation exhibited good agreement with SLICER data that have a slow decay of the waveform for large footprint capture from conifer forest stands in central Canada and two closed canopy deciduous forest stands in eastern Maryland.

The use of a radiative transfer model that builds on the foundation of ray tracing and fractal models of tree geometry is another alternative for modeling of the airborne laser scanning returns, especially for small footprint data. This is true since the tree models need to be more complex and should explicitly resolve the tree structure at the leaf level. Such an approach enables one to individually simulate the effects of acquisition properties, such as incidence angle, terrain slope, footprint size, laser wavelength, and canopy scattering factors. It is evident from this section that existing LiDAR radiative transfer modeling not only serves as the mathematical basis for the waveform signal processing and data analysis, but also helps us to better understand the physics and scheme behind the waveform properties. However, the efficacy of this modeling is heavily dependent on how the waveform signal is processed before any analysis is attempted.

1.2.2 Waveform LiDAR preprocessing techniques

1) Noise reduction

The raw incoming waveform typically includes a certain noise level due to the LiDAR sensor design and operation, such as dark current noise caused by the detector, thermal noise, etc. There are many LiDAR signal noise reduction approaches reported in the literature. For example, the signal accumulation technique [21] based on the assumption of zero mean random noise is widely used for noise reduction, but the

problem lies in the challenge of determining the properties of the noise component in the actual LiDAR signal in most cases. Approaches like the moving average method, on the other hand, could distort the waveform and smooth out the local details of the waveform signal [22]. Okumura *et al.* [22] proposed the use of Canonical Correlation Analysis (CCA) to perform noise reduction and provide an improved reduction of the noise amplitude component and mean square error against ground level; however, this approach also requires the non-lasing signal with only the noise component for data processing. Frequency-based filtering could impact the local high frequency components of the waveform signal, but by observing instances of real waveform data, we concluded that such an impact is minimal [Figure 2.7]. Furthermore, due to the efficiency of fast Fourier transform implementation, the frequency-based noise reduction is arguably a better approach than those mentioned above for preprocessing of waveform LiDAR signals.

2) Signal deconvolution

The raw LiDAR signal is typically "smeared" and the effective temporal resolution decreased due to a series of convolutions, shown in the mathematical expression (Eq. 2) of the LiDAR waveform model. The ultimate goal is to recover the cross-section $\sigma(t)$ of the illuminated target, which corresponds to the true distribution of optically-active substances along the ray path of the LiDAR pulse. We can first simplify Eq.2 to solve this deconvolution problem, by (i) ignoring the atmospheric factors and (ii) removing the constant terms, since these will not affect the shape of the waveform for a cross-section. Finally, we derived the received LiDAR signal $P(t)$, described by the convolution integral:

$$P(t) = \int_{-\infty}^{+\infty} R(t'-t) P_{\delta}(t') dt' + N(t) = (R * P_{\delta})(t) + N(t) \tag{3}$$

where $R(t)$ is the system contribution term, which is equal to the convolution of the outgoing waveform or transmitted pulse (generally provided by the commercial LiDAR system with waveform digitizing capabilities) and the system impulse response, which can be estimated from the return from flat ground (Lambertian surface), $P_{\delta}(t)$ is the target cross-section, and $N(t)$ is the additive noise term. Theoretically, such a loss of the

resolution can be recovered by using the deconvolution of the measured signal with the system response function. Different deconvolution approaches have been applied in literature to solve for the true cross-section. For example, Jutzi and Stilla [18] proposed the use of the Wiener filter [23] to estimate the surface response from the noisy received waveform by assuming that a plane surface is perpendicular to the pulse propagation direction and the surface is illuminated by an infinitesimal footprint. Nordin [24], on the other hand, mentioned that more canopy and ground echoes can be detected when using a waveform deconvolved via the Richardson-Lucy algorithm [25]. Harsdorf *et al*. [26] presented a deconvolution comparison between a Fourier transform approach and the non-negative least squares [27] and Richardson-Lucy algorithms using single arbitrary simulated waveforms. The authors concluded that the Richardson-Lucy approach performed best, based on visual comparison of the deconvolution results. However, these existing results and conclusions are typically based on the observation of several deconvolution samples, rather than a quantitative comparison. This lack of quantitative comparisons is mainly due to our inability to accurately describe the true target cross-sections from a realistic scene. It is thus evident that the selection of the optimal deconvolution approach for LiDAR waveform preprocessing is inadequately addressed in literature. The following gives a brief review of the three most widely used signal deconvolution algorithms in the literature, all of which will be quantitatively evaluated for comparison.

a. Richardson- Lucy algorithm: The Richardson-Lucy (RL) algorithm is an iterative algorithm originally developed for astronomical image restoration [28]. It is derived directly from the Bayes theorem. The RL algorithm can also be used for deconvolution when we regard a LiDAR waveform profile as an image with the dimension 1xN. The i^{th} iteration solution can be calculated by [26]:

$$P_{\delta}^{i+1}(t) = P_{\delta}^{i}(t) \cdot \left(R(t) * \frac{P(t)}{(R * P_{\delta}^{i})(t)} \right) \tag{4}$$

where the residual of each iteration is computed as:

$$r^{i}(t) = P(t) - (R * P_{\delta}^{i})(t) \tag{5}$$

The residual will converge as the iteration progresses. The user can terminate the iteration, either by selecting a specific residual threshold or by setting a constant iteration number.

b. Wiener filter

The Wiener filter (WF) approach has been used by researchers for the deconvolution of LiDAR waveforms. It assumes that the noise and the signal are statistically independent and results in the Wiener filter, constructed in the frequency domain [18]:

$$W(f) = \frac{\left|\overline{P}(f)\right|^2}{\left|\overline{P}(f)\right|^2 + \left|\overline{N}(f)\right|^2} \tag{6}$$

where $\overline{N}(f)$ (noise signal $N(t)$ in the frequency domain) can be estimated from the background noise and $\overline{P}(f)$ is estimated by low-pass-filtering of the received signal $P(t)$ in the frequency domain. The final estimation of the $P_\delta(t)$ term (target cross-section) is described by Eq. 6, followed by an inverse Fourier transformation to the time domain:

$$\overline{P}_\delta(f) = \frac{P(f)\cdot W(f)}{R(f)} \tag{7}$$

so that the sum of the square error becomes:

$$\left\|\overline{P}_\delta(t) - P_\delta(t)\right\|^2 = \int_t \left(\overline{P}_\delta(t) - P_\delta(t)\right)^2 = \min . \tag{8}$$

c. Non-negative least squares algorithm

The classic form of the non-negative least squares (NNLS) problem can be expressed as follows: Given a matrix $A \in R^{m\times n}$ and the set of observed values, given by $b \in R^m$, find a non-negative vector $x \in R^n$ to minimize the function $f(x) = \frac{1}{2}\left\|Ax - b\right\|^2$, i.e.

$$\min_x f(x) = \frac{1}{2}\left\|Ax - b\right\|^2 \tag{9}$$

$$subject\ to\ x \geq 0$$

We can thus express the deconvolution problem with respect to $P_\delta(t)$ in the form of minimizing the sum of the square error:

$$\left\|(R * P_\delta)(t) - P(t)\right\|^2 = \left\|N(t)\right\|^2 = \min,\ P_\delta(t) \geq 0 \forall t \tag{10}$$

The solution $P_\delta(t)$ can be calculated iteratively as the finite convergence of the error without any prior information about $P_\delta(t)$ and $N(t)$, according to Lawson and Hanson's algorithm. More details about the steps of iterative solution can be found in [27].

3) Waveform decomposition

Waveform decomposition is also of great research interest in the waveform LiDAR signal processing arena. Such decomposition typically implies the parameterization of the waveform as a combination of a series of components, e.g., Gaussian distributions (Eq.12). This processing step effectively reduces the dimensionality of a waveform and also facilitates direct feature extraction for characterizing waveform properties, such as peak position, width, inflection points, local maximum intensity, etc. A number of waveform LiDAR-related signal decomposition approaches have been proposed in the literature in recent decades. For example, Wagner *et al.* [19] used Gaussian decomposition for processing and calibrating small-footprint waveform data and derived the estimates of the backscatter cross-section of each target. Persson *et al.* [29] developed a pulse detection method, based on the Expectation-Maximization (EM) algorithm, to decompose the waveform signal and thus detect the unresolved peaks in the raw waveform. Roncat *et al*. [30], on the other hand, presented an approach to decompose the backscatter cross-section as an individual symmetric scatterer in full-waveform LiDAR data using uniform B-splines. However, these existing waveform processing approaches typically cannot be verified in a direct or quantifiable manner due to our inability to accurately describe the true cross-sections from a realistic scene. For instance, the above-mentioned waveform decomposition algorithms are helpful to recover the loss of the spatial resolution of the raw data and boost the possibility of peak detection, but whether these decomposed components or unveiled weak peaks really exist or contain certain errors, still remains unsolved. The following shows the generic mathematic model for waveform decomposition algorithms:

A waveform $y = f(x_i)$ typically can be modeled as a linear sum of *n* components:

$$y_i = \sum_{k=1}^{n} \phi_k(x_i) + b_i \tag{11}$$

where *f* is the waveform model, ϕ is the echo model, and *b* is the noise. The most frequently used model for full-waveform data decomposition assumes the received signal as a mixture of Gaussian distributions:

$$\phi_k(x) = A_k \exp\left(-\frac{(x-\mu_k)^2}{2\sigma_k^2}\right) \tag{12}$$

where A_k is the pulse amplitude, σ_k is the pulse width, and μ_k is the pulse range. The Gaussian mixture model typically can deal with most signal-target situations, but in the case of received waveforms from urban areas, the components are frequently subject to various effects of geometric (e.g., roof slopes) and radiometric object properties (different materials) [8], which could result in distorted peaks. Consequently, some alternative models have been proposed in the literature. For example, Chauve *et al.* [31] used the generalized Gaussian function to improve the distortion error. The final problem to solve is the estimation of the modeling function (e.g., A_k, σ_k, and μ_k) so that:

$$\left\| f(x_i) - y_i \right\|^2 = \min \tag{13}$$

Several methods have been applied to solve such waveform fitting problems in the literature, including the non-linear least-squares approach using the Levenberg-Marquardt optimization algorithm [32], the maximum likelihood estimate based on the Expectation-Maximization algorithm [33], and stochastic approaches using a reversible jump Monte Carlo Markov chain method [34].

In summary, this literature review shows the main preprocessing methods that have been applied to waveform LiDAR, including noise reduction, deconvolution, and decomposition. However, these approaches are typically application-specific, instead of representing an end-to-end generic processing approach that can be applied to any waveform LiDAR data processing chain. For example, advanced noise reduction techniques typically need additional calibration data, which are not available to most LiDAR users. Additionally, the geometrical information in terms of zenith and azimuth of the laser pulse target interactions has not been taken into account for waveform

calibration. The 3D (x,y,z) location to which a specific waveform LiDAR interaction is assigned therefore could be erroneous if proper processing techniques are not applied to the data. This is especially evident in the case where an off-nadir waveform, such as one associated with a $0.5m^2$ footprint, 0.56mrad beam divergence, and 1km flying altitude, could actually cover a much larger area than that of a purely nadir waveform collected by an airborne LiDAR system. Last but not least, the effect of existing waveform processing approaches, especially for recovering the loss of temporal resolution by decomposition or deconvolution, typically cannot be verified in an absolute and quantitative manner due to our inability to accurately describe the true cross-sections from a realistic scene. The above-mentioned waveform decomposition and deconvolution algorithms can recover the loss of the temporal resolution in the raw data and thus boost the accuracy of peak detection rate, but whether these estimated cross-sections or unveiled peaks really exist or what their associated errors are, remains undetermined.

These concerns and the lack of an end-to-end, validated small-footprint waveform LiDAR preprocessing chain, served as the motivation for developing and verifying an operational waveform LiDAR preprocessing chain as one of our research objectives. We contend that this chain should include noise reduction, deconvolution, signal registration to a ground surface (digital elevation model or DEM), and angular rectification in order to perform a comprehensive waveform data calibration, which will be discussed in Chapter 2.

1.2.3 Waveform LiDAR processing for 3D object reconstruction

LiDAR-based 3D tree reconstruction allows us to not only retrieve detailed knowledge of three-dimensional tree structure, but could also enable the automation of analyses for accurate estimation of forest woody or foliar biomass. Such research has significant potential to ameliorate the effects of current extensive and expensive field data collection procedures. A number of efforts have been made to reconstruct the stem and branch structures from LiDAR scans. Gorte and Pfeifer [10] proposed a tree stem and branch reconstruction algorithm in 3D voxel space by using point cloud data (sequence of x, y, z triples) captured with Zoller and Frohlich laser scanners. This approach is based on

a variety of basic and advanced 2D raster (image) processing approaches, which are transferred to the 3D domain. The approaches include filtering, mathematical morphology, skeletonization, connected component labeling, and shortest route computation. Figure 1.4 shows an example of branch reconstruction in voxel space.

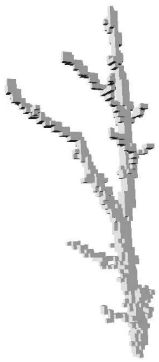

Figure 1.4. An example of 3D reconstruction of tree branches based on Gorte and Pfeifer's [14] voxel approach

Binney and Sukhatme [11] presented a probabilistic 3D tree-branch reconstruction model and applied a generative model of a tree to guide an iterative reconstruction process. Their approach succeeded in recovering parameters such as branch locations, angles, radii, and lengths, as well as connectivity information between branches (Figure 1.5).

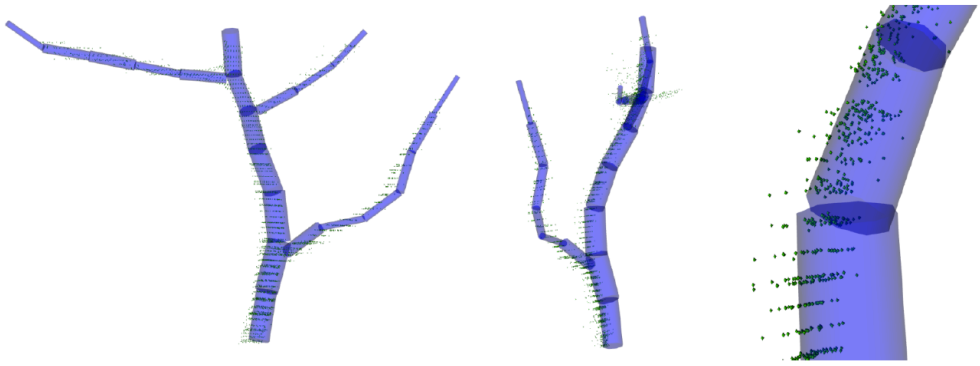

Figure 1.5. Probabilistic 3D reconstruction of branches, proposed by Binney and Sukhatme [15]

More recently, Cote *et al.* [35] proposed a modeling approach to reconstruct plausible tree structures from multiple LiDAR scans (co-registered 3D point cloud data). The main

steps of the algorithm include: (i) Point cloud segmentation in terms of wood and foliage components; (ii) skeleton structural extraction; (iii) growing of finer branching structure; (iv) defining typical foliage structure; and (v) distributing foliage elements within the crown by using a light availability model. The main strength of the proposed reconstruction algorithm lies in its capacity to reconstruct the tree architectures even when the spatial/angular resolutions are low or under non-ideal external conditions, e.g., in the presence of wind and/or occlusions of the interior of the tree crowns (Figure 1.6).

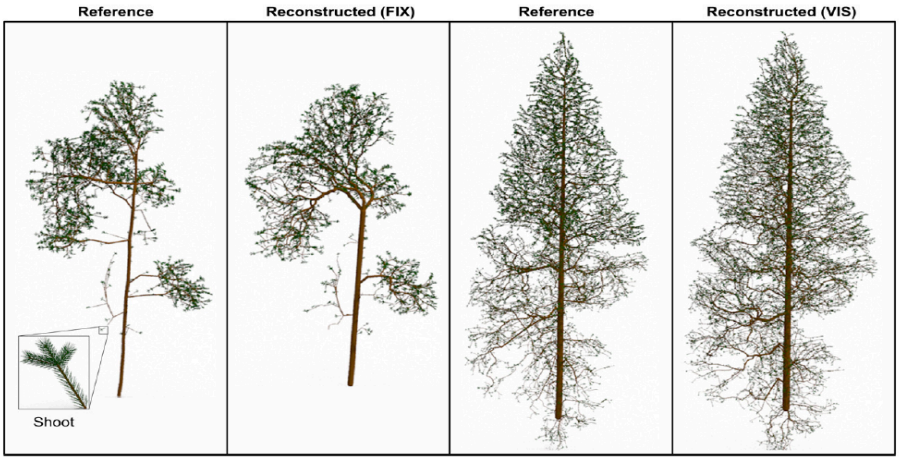

Figure 1.6. 3D tree reconstruction proposed by Cote et al. [35]

However, as is shown in this section a limited number of state-of-the-art 3D tree reconstruction algorithms based on LiDAR exist. It was concluded that these reported methods from the literature are typically based on high density discrete return or point cloud datasets from ground-based LiDAR systems, i.e., a sequence of x, y, z coordinate combinations. A direct inverse modeling approach based on full-waveform LiDAR data still presents a gap in terms of LiDAR research. This is especially true since such ground-based LiDAR systems can only acquire data for a small area for vegetation reconstruction, which is not useful for ecosystem monitoring, such as land degradation analysis and its associated requirement of a large area sample. Last but not least, most of the existing reconstruction approaches are primarily focused on branch and stem reconstruction and the challenge of 3D leaf-on tree reconstruction has not been addressed adequately. We postulate that waveform LiDAR-based 3D tree reconstruction holds significant potential,

given that the spatial resolution of full waveform LiDAR systems has seen significant improvements (e.g., less than half meter) and such systems have the unique capability of recording of the entire cross section of a target.

1.3 Vegetation applications of waveform LiDAR technology

Full-waveform LiDAR data have been widely used for forest analysis due to its enhanced ability to characterize the canopy vertical spatial structure. Currently, applications of waveform LiDAR basically fall into two general categories, namely estimation of vegetation structure and function (canopy height, crown volume, above-ground biomass, etc.) and object detection and classification [15].

Estimation of canopy height, which is extracted from the measurement of the distance between local peaks of the waveform as a feature metric, is one the most widely used and promising applications of waveform LiDAR. For example, Rosette *et al.* [36] used GLAS/ICESat data for tree height retrieval (Figure 1.7) over a managed, mixed temperate forest with varied relief and reported an R^2 value of 0.89 between field measurements and waveform estimates. The authors suggested that ICESat waveform data are capable of providing a reliable indicator of actual canopy height.

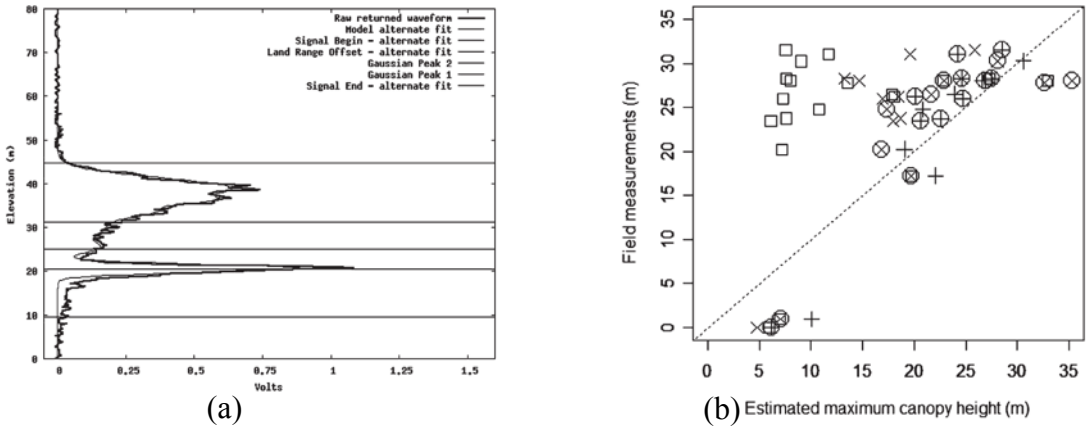

Figure 1.7(a) Typical bimodal waveform. Horizontal lines are then illustrated in the order listed from top to bottom; (b) Relationship between field measurements and estimates of maximum canopy height from waveform parameters [36].

Farid *et al.* [37] proposed the use of four metrics, namely tree height, height of median energy, ground return ratio, and canopy return ratio (see Figure 1.8), derived from waveform LiDAR data, to predict forest leaf area index (LAI) by applying linear regression models between the metrics and field-measured LAI. Results proved that the waveforms had a good degree of correlation with physical measurements. Anderson *et al.* [38] also reported a strong agreement between field and LiDAR-measured height (R^2=0.8, p<0.000) for large-footprint data using NASA's Laser Vegetation Imaging Sensor (LVIS). In another study, allometric calculations of above-ground biomass and waveform metrics of LVIS data (R^2 =0.61, *PRESS RMSE*=58.0$Mgha^{-1}$, p<0.000) and quadratic mean stem diameter and LVIS metrics (R^2=0.54, p<0.002) also showed good agreement at the footprint level [38].

This represents a small number of similar studies evaluating waveform metric extraction, based on the vegetation structure and function estimation approach, that has been reported in the literature [e.g., 39-40]. However, most of these methods were based on large-footprint waveform LiDAR data, which can only determine the structural parameters of trees at coarse levels. Small-footprint waveform LiDAR obviously has advantages when it comes to "fine-scale" structure applications, such as branch and/or woody biomass, crown volume at individual tree level, and scalable foliar area or biomass. Additionally, existing approaches were typically applied to tree structures, whereas we expect that the application of small-footprint waveform LiDAR can be extended to include structural estimation at sub-canopy levels, such as brush and grass levels. For instance, estimation of grass density or herbaceous biomass, is another area where small-footprint waveform LiDAR potentially can prove advantageous over other LiDAR systems. Such fine-scale woody and herbaceous biomass estimation methods ultimately can be coupled to ecosystem dynamics such as carbon sequestration, resource use by man and wildlife, and land degradation at different levels. From a validation standpoint, we can also use such structural feature extraction as a tool with which to verify the effectiveness of our waveform preprocessing chain (Objective 1). This section of the literature, in terms of waveform LiDAR-based applications for vegetation structural assessment, therefore serves as the motivation for Objective 2 in this research.

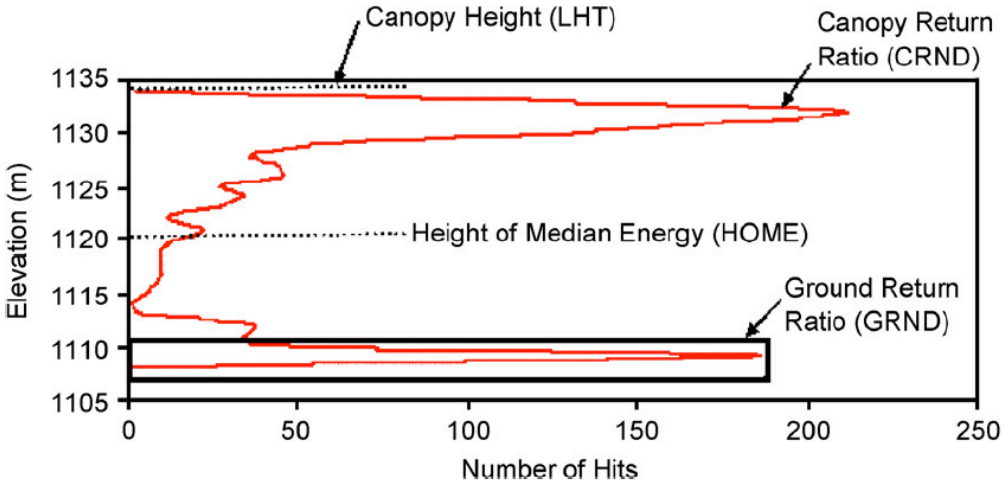

Figure 1.8. Metrics derived from synthetic large-footprint LiDAR waveforms [41]

Chapter 2: LiDAR waveform preprocessing chain development

In this chapter, we first describe the datasets used for testing the proposed processing chain, namely real waveform Carnegie Airborne Observatory (CAO) data and simulated waveform via the Digital Imaging and Remote Sensing Image Generation (DIRSIG) model. Next, the processing chain is presented in a stepwise fashion that follows the diagram in Figure 2.1. This approach assumes that the following information is available for each of the per-pixel waveform LiDAR signals: (i) outgoing waveform, (ii) incoming waveform, (iii) angular information, including zenith and azimuth, (iv) slant range, and (v) a digital elevation model (DEM) for the site of interest. Finally, metrics for evaluating the performance of the processing chain are introduced for both simulated and real waveform data in order to provide a comprehensive validation of the approach. We recognize that the proposed framework and methodology may not be optimal for all waveform LiDAR users, depending on their specific applications or computational resource limitations. However, the purpose of this study was to develop, validate, and propose a standardized waveform preprocessing approach for waveform LiDAR researchers and engineers to extract more representative and accurate 3D structural parameters from remotely sensed scenes. Outputs from this chapter have been published as follows:

- Wu J., J.A.N. van Aardt, and G.P. Asner. A Comparison of Signal Deconvolution Algorithms Based on Small-Footprint LiDAR Waveform Simulation. *IEEE Transactions on Geoscience and Remote Sensing* 49(6): 2402-2414, 2011 [42].
- Wu J., J.A.N. van Aardt, J. McGlinchy, and G.P. Asner. A Robust Signal Preprocessing Chain for Small-footprint Waveform LiDAR. *IEEE Transactions on Geoscience and Remote Sensing,* 50(8): 3242-3255, 2012 [43].

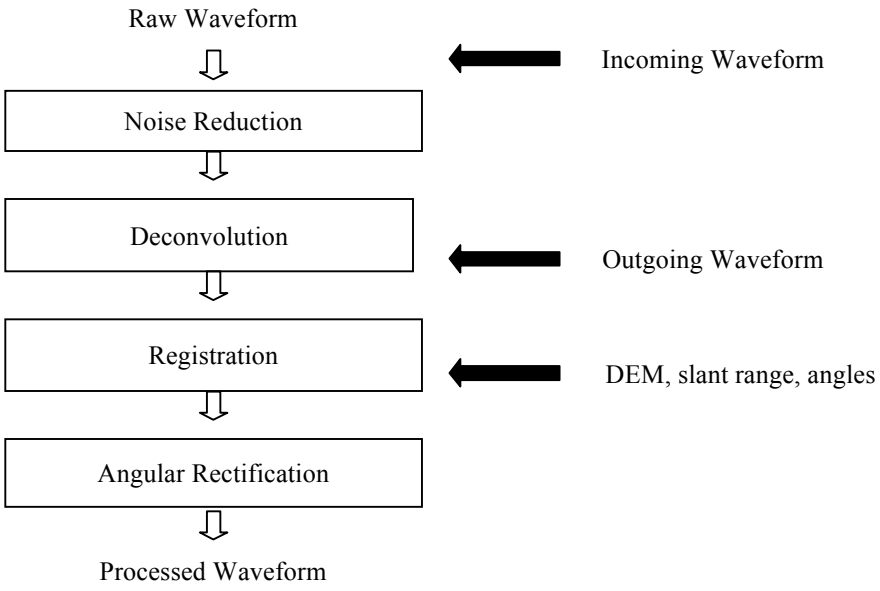

Figure 2.1. A flowchart of the waveform LiDAR preprocessing chain

2.1 Methods

2.1.1 Available data

2.1.1.1 Real waveform and associated field data

The study area for this research effort is comprised of a section of land within and surrounding Kruger National Park (KNP) in South Africa (Figure 2.2). The area is bounded by (22°8'00" S; 30° 34'52"E) and (25° 32' 48"S; 32° 2' 50" E) and spans a west-east land use gradient. This gradient is defined by sampling in Bushbuckridge (communal rangelands; high rural population density), Sabie Sands game reserve (private conservation area), and Kruger National Park (state-owned conservation area). The topography is gently undulating with a slowly decreasing terrain height toward the east, with an average altitude of approximately 450m above mean sea level. Vegetation communities are influenced largely by geomorphological and pedological processes at

the landscape level. Dominant geology includes granite and gneiss with local intrusions of gabbro. Vegetation has a discontinuous overstory of woody plants, mostly in the 2-5m height category, and a herbaceous layer dominated by C4 grasses [44]. The vegetation communities are classified as granite lowveld or gabbro grassy bushveld according to Muncina *et al.* [45]. Therefore, the waveform and field data we collected have enough physical variability in terms of the wide range of woody structure and biomass level for further analysis.

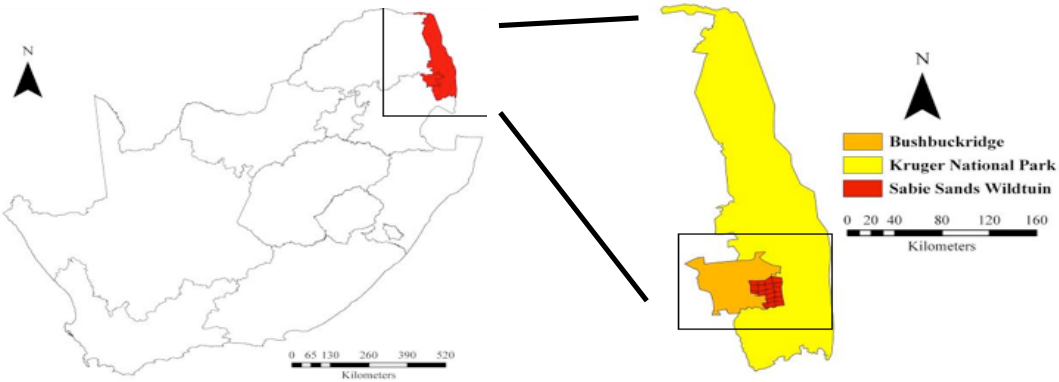

Figure 2.2. The study area and associated land use gradient in South Africa

Waveform LiDAR data were collected by the Carnegie Airborne Observatory (CAO) alpha system, using a custom-built Optech ALTM 3100EA system (Figure 2.3) with an outgoing pulse width of 16ns, a laser wavelength of 1064nm, a footprint of 0.56m, and a temporal resolution of 1ns, which corresponds to 0.15m vertically.

Field data for this research were collected during May 2008 - in association with an airborne data collection campaign - from 36 sites in the study area, each 50 x 50 m in size. A total of 36 plots (2-5 meter variable radius) were laid out within each site on a 10m spacing, resulting in a grid-like pattern (Figure 2.4); however, only nine sites fell within the area that was covered by the waveform LiDAR system, for a total of 224 plots. A Trimble (Trimble® Recon® Handheld with aerial backpack) or Leica (GS20 Professional Data Mapper with handheld aerial) differential GPS was used to collect accurate geographic co-ordinates for each tree and grass measurement, which were differentially corrected to sub-meter accuracy using the Nelspruit trigonometric base station one second data (http://www.trignet.co.za/). Individual trees were measured for

crown height and diameter at breast height (DBH) to be used as input to allometry equations for calculation of woody biomass. Herbaceous biomass was directly measured by the weight of dry grass within a 0.5×0.5m grid at each plot center.

Figure 2.3. CAO Alpha system with the ALTM 3100 waveform LiDAR system.

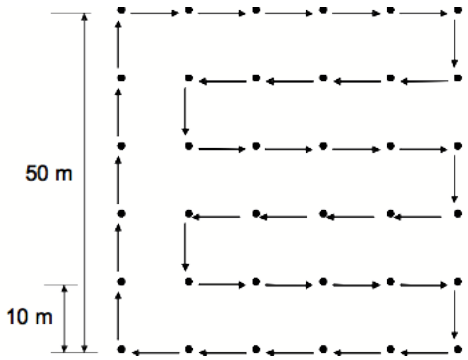

Figure 2.4. Site-level sampling design with 36 plots/site.

2.1.1.2 Simulated LiDAR waveform data

Virtual scenes that combined a 3D deciduous tree, above-ground grass layer, and ground were created as the input for the DIRSIG simulation (see appendix A.1 for more details) by using the tree generation software "Arbaro" [46] and rendered using the open source 3D graphics application "Blender" [47] (Figure 2.5). Materials including leaves, branches, grass, and ground with valid emissivity and extinction coefficients, as measured from actual vegetation, were mapped to each facet of these 3D models. This enabled us to comprehensively simulate the process of laser pulse interaction with vegetation, including absorption, reflection, and transmission at each facet. We created a 3D real world coordinate system (x,y,z) with the center of the tree base as origin, in order to better characterize the relative position between the scene and the laser pulse. The zenith and azimuth angles were used, as Figure 2.5 shows, to define the trajectory of each laser pulse.

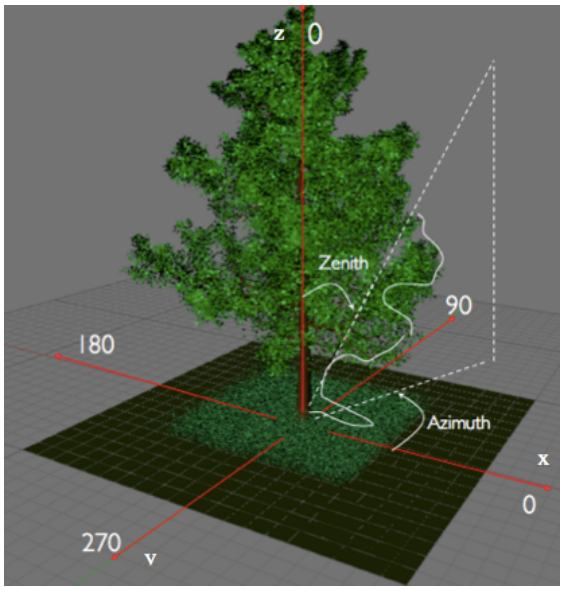

Figure 2.5. An example of a virtual scene for generating simulated waveform LiDAR:

- *Ground: 20m×20m (x, y)*
- *Grass: 12m×12m×1m (x, y, z)*
- *Tree: 7.2m×7m×10m (x, y, z)*

The LiDAR system configuration is another important input required for accurate waveform simulation. The parameters that were used for configuring the LiDAR system are summarized in Table 2.1. The goal was to match our virtual system with commercially available small-footprint waveform LiDAR systems. For instance, the

flying height (1000m) and beam divergence (500 mrad) were used to generate the size of small-footprint waveform simulations (0.5m). The selection of pulse width was motivated by the outgoing pulse width of 16ns, as implemented in the operational waveform LiDAR data collected by the CAO using a custom-built Optech ALTM 3100EA system; the same applies to the selection of 1ns as sampling resolution (time bin) and 1064nm as wavelength. This allowed for the simulation results to be directly compared to operational or real data. We also added 2ns, 4ns, and 8ns outgoing pulse widths for simulation purposes. This was due to the facts that the 2ns outgoing pulse width (near perfect system impulse response) can be used to generate the approximated or truth dataset and the 4ns/8ns pulse widths are the standard settings for CAO wLiDAR and other commercial systems. These pulse widths therefore can be used as intermediate widths between 2ns and 16ns to test the robustness of the processing chain at different outgoing pulse widths.

We furthermore restricted the outgoing pulse shape to approximate a Gaussian distribution, based on our observation of the actual outgoing pulses from the CAO: the shape of the actual pulses closely approximates a "Gaussian" distribution and the observed asymmetry is minimal. It was also observed that the shape of the actual outgoing pulses varies in terms of the slope and intensity. We therefore used a Gaussian approximation in order to maintain consistency in the shape of the outgoing pulse across all the waveforms for our simulation.

The selection of the zenith and azimuth angle, which characterizes the trajectory of the laser pulse, was also based on the observation of the angle distribution in the real LiDAR system (Figure 2.6). We can see that the zenith angle ranges between 5° and 10°, and a small number stretches to a relatively large off-nadir angle at around 15°. The distribution of the azimuth angle is typical of the across-track LiDAR scanning, i.e., scanning perpendicular to the flight path. We therefore simulated waveforms at 16 different off-angle directions, based on all the combinations of azimuth (0°, 90°, 180°, 270°) and zenith (5°, 10°, 15°, 20°) values, plus a waveform dataset at nadir view (zenith=0°), in order to provide a comprehensive characterization of both nadir and off-angle LiDAR waveforms. The 2ns outgoing pulse, sampled at nadir, was used to generate

the approximated or truth dataset in order to facilitate comparisons with the angular, rectified, off-angle waveforms.

TABLE 2.1
A DESCRIPTION OF THE LIDAR SYSTEM CONFIGURATION

Flying height above ground (m)	1000
Beam divergence (mrad)	500
Sampling resolution (ns)	1
Wavelength (nm)	1064
Outgoing pulse shape	Gaussian
Outgoing pulse width (ns)	2/4/8/16
Footprint (m)	0.56
Zenith angle (°)	0, 5, 10, 15, 20
Azimuth angle (°)	0, 90, 180, 270

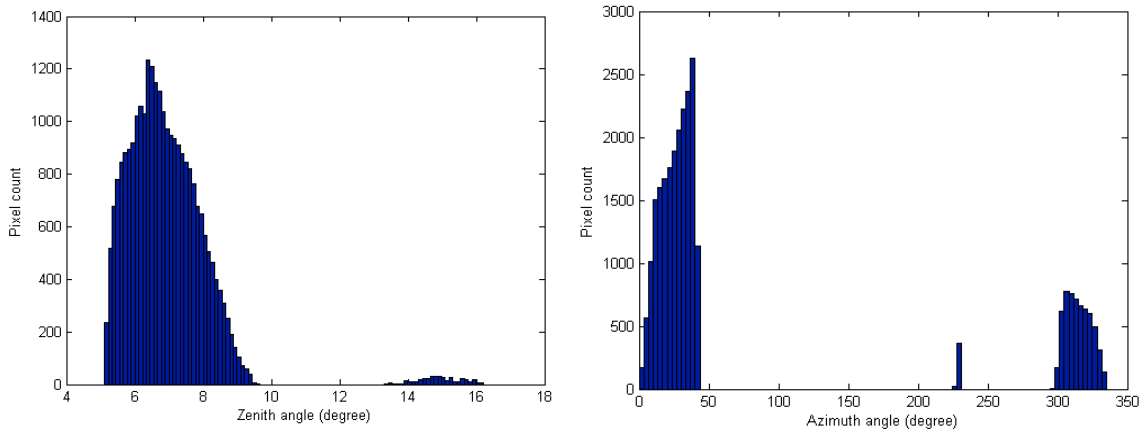

Figure 2.6. Histogram of the zenith (a) and azimuth (b) angle distributions based on real waveform LiDAR data collected by CAO

2.1.2 Noise reduction

The raw incoming waveform typically exhibits a certain noise level due to sensor impacts, such as dark current noise caused by the detector, thermal noise, etc. Signal

noise was simulated using uniformly distributed pseudo-random numbers, assuming white noise, and was added to each waveform in order to approximate the real LiDAR signal-to-noise ratio, which is unknown. This approach also served to test the robustness of processing steps, e.g., deconvolution algorithms, against noise. The amplitude of the noise (Figure 2.7) was estimated by averaging the absolute difference between the noisy and the smoothed waveform data collected by Carnegie Airborne Observatory systems. The resultant waveforms arguably may not reflect the exact noise level and distribution in real waveform LiDAR systems, while the actual signal-to-noise ratio may also vary between different system types and configurations. However, considering that this effort (i) represented a relative comparison of different deconvolution approaches, (ii) used the same waveform data with the same added noise, and (iii) that the high frequency noise is dominated by low frequency signals in such systems, we believe that the impact induced by the relatively simplistic noise estimation was minor.

Many LiDAR signal noise reduction approaches are reported in literature, e.g., the signal accumulation technique, based on the assumption of zero mean random noise [21], is widely used for noise reduction. However, it is difficult to determine the properties of the noise component in actual LiDAR signals in an operational environment. The moving average method, on the other hand, could distort the waveform and smooth the local details of the waveform signal [22]. And as discussed before, the Canonical Correlation Analysis (CCA) proposed by Okumura *et al.* [22] requires the non-lasing signal with only the noise component for data processing, which is usually not available to most LiDAR users. We therefore implemented another, widely used technique in our preprocessing chain: a low pass filtering in the frequency domain by employing the fast Fourier transform to the 1D waveform data, given its efficiency and ease of implementation. The frequency-based filtering could impact the local high frequency components of the waveform signal, but by observing instances of real waveform data (Figure 2.7), we concluded that such an impact is minimal. This is because the valid frequency of the backscattered LiDAR signal typically is lower than the noise frequency, due to the stretched signal width, which is a function of the outgoing pulse signal and the receiver impulse response (see Figure 2.8). In theory the selection of the cut-off frequency threshold could be determined by using mathematical properties, e.g., those extracted via

derivative analysis (e.g., zero crossing point) or integration of the area over the frequency spectrum (e.g., 99% of the underlying area). However, the complexity of automated approaches for real datasets and the ability of deconvolution to overcome certain noise level might negate the need for additional complexity.

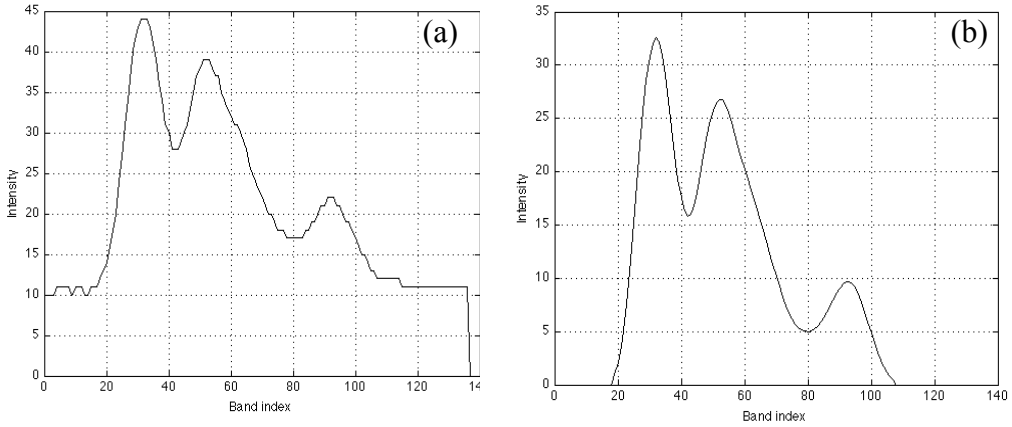

Figure 2.7. Illustration of the waveform noise filtering: (a) Real (raw) waveform data collected by the Carnegie Airborne Observatory system and (b) the smoothed waveform following frequency-based noise filtering. Note: a negative noise level shift of 11 units was applied to the raw signal first to avoid the potential frequency leakage caused by the sharp edge at the inflection point (signal on/off)

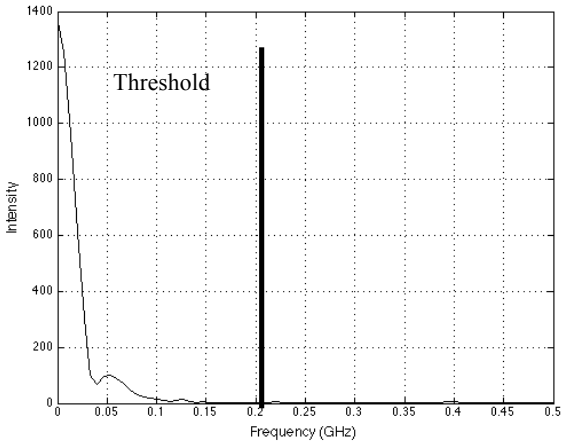

Figure 2.8. A typical frequency representation of a waveform signal. A cut-off frequency threshold of 0.2GHz was selected based on visual assessment of filtering results; any frequency component above 0.2GHz was attributed to noise and set to zero.

2.1.3 Deconvolution

The raw incoming waveform is usually smeared and the effective temporal or vertical resolution decreases due to the non-perfect outgoing pulse signal (e.g., distorted Gaussian, instead of delta function) and the receiver impulse response. Theoretically, such a loss of resolution can be recovered by deconvolving the system response from the measured signal. We therefore introduce a quantitative comparison approach between the three most widely used deconvolution techniques in the waveform LiDAR processing literature, namely the Richardson-Lucy (RL), Wiener filter (WF), and non-negative least squares (NNLS) algorithms.

In order to evaluate the impact of and need for deconvolution on waveform processing, especially for vegetation applications, we tested the algorithms in the context of two vegetation structural assessments: (i) ability to recover the true cross-section profile of an illuminated object, based on the waveform simulation of a virtual 3D tree model (Figure 2.5) and (ii) the ability to differentiate variation in herbaceous biomass, based on the waveform simulation of virtual grass patches.

2.1.3.1 Recovering the true cross-section of vegetation

One of the basic goals of deconvolution of LiDAR waveforms is to remove the unwanted system contribution and extract the true cross-section profile of the illuminated object. However, this true cross-section is typically impossible or difficult to measure directly for real targets such as trees, grasses, and other natural targets. We circumvented this problem by operating in the DIRSIG simulation environment. We simulated a near-perfect outgoing pulse with a narrow outgoing pulse width. In this case, most of the backscattered response contained in the return signal will result from the target itself, thus approximating the true cross-section. We set the width of outgoing pulse to 2ns, given that the sampling rate of the waveform is 1ns - an outgoing pulse width < 2ns might result in artifacts after deconvolution. We incrementally increased the width of the outgoing pulse, from 2ns to 8ns, and 16ns to simulate the setting of real small-footprint LiDAR sensors, e.g., the Optech ALTM 3100EA operated by the Carnegie Airborne

Observatory [46]. This was followed by the application of the three deconvolution algorithms to the simulated return signals and a comparison of the resultant deconvolved signals with the true cross-section data (approximated by the 2ns outgoing pulse). Two waveform datasets, namely the 2ns true response and the deconvolved comparison, should be similar in terms of shape if the deconvolution functioned properly. We simulated the complexity and diversity of natural trees by generating six different virtual 3D trees at a fine- or object-scale, whose specifications and rendered images are listed and shown in Table 2.2 and Figure 2.9, respectively. Each tree plot consisted of branches, leaves, and ground associated with their respective valid emissivity and extinction coefficients [43]. The plot for each tree was divided into a 40x40 pixel grid with a waveform footprint size equal to 0.5m. This resulted in a waveform with 225 time bins, from 24.995m to -8.605m "above ground", at an increment of 0.15m for each pixel after implementing the simulation. Finally, three sets of simulated waveforms were generated for each tree plot for outgoing pulse widths of 2ns, 8ns, and 16ns to check the monotonic trend of the deconvolution comparison results in terms of outgoing pulse width. A 4ns simulation was added for preprocessing validation based on feedback from journal reviewers to ensure that the preprocessing chain can be applicable to different operational sensors specifications.

Three metrics were used to assess the performance of the respective deconvolution algorithms in terms of recovering the cross-section:

1. Root mean square error (*RMSE*) value between the truth and the deconvolved waveform:

$$RMSE = \sqrt{\frac{\sum_{n}\sum_{m}\left(\tilde{P}_{\delta,2}(t) - P_{\delta,w}(t)\right)^2}{m \times n}} \tag{14}$$

where $\tilde{P}_{\delta,2}(t)$ is the truth cross-section approximated by the direct simulation results using an outgoing pulse width equal to 2ns. $P_{\delta,w}(t)$ corresponds to the deconvolved waveform using an outgoing pulse widths equal to w =8, and 16ns. m and n are the number of time bins for each waveform and the total number of waveforms for the plot (e.g., m=225, n=1600 in this paper), respectively.

2. We also evaluated the waveform sensitivity to local peak detections by determining where the sign of the first derivative of the waveform changes for different deconvolution approaches. This is defined as:

$$Sensitivity = \frac{\#\ of\ true\ detections}{total\ \#\ of\ true\ peaks} \tag{15}$$

True detection is defined by the time bin index of a detected local peak from the deconvolved waveforms that agrees with a true peak, which is extracted from the 2ns waveform simulation for each of the six trees.

3. Finally, another important metric, called the false discovery rate, was extracted and is defined as:

$$False\ discovery\ rate = \frac{\#\ of\ \ false\ detection}{total\ \#\ of\ detected\ peaks} \tag{16}$$

where false detection is the opposite of the true detections, described above.

TABLE 2.2
SPECIFICATIONS OF THE 3D VIRTUAL TREES USED FOR WAVEFORM SIMULATION

	Tree 1	Tree 2	Tree 3	Tree 4	Tree 5	Tree 6
Species	Sassafras (*Sassafras albidum*)	Sassafras (*Sassafras albidum*)	Black Tupelo (*Nyssa sylvatica*)	Quaking Aspen (*Populus tremuloides*)	Black Tupelo (*Nyssa sylvatica*)	Eastern Cottonwood (*Populus deltoides*)
Crown Length (m)	12.13	14.84	12.96	9.62	13.02	16.16
Crown Width (m)	13.81	14.47	13.07	9.82	13.17	12.02
Height (m)	19.65	20.53	19.61	19.08	19.84	18.97
# of leaves	172353	163607	111321	65964	111525	108093
# of branches	53205	50577	56911	12029	56947	9704
Leaf Length (m)	0.17	0.18	0.26	0.17	0.26	0.21
Leaf Width (m)	0.12	0.12	0.13	0.17	0.13	0.21

Tree 1: *Sassafras albidum*

Tree 2: *Sassafras albidum*

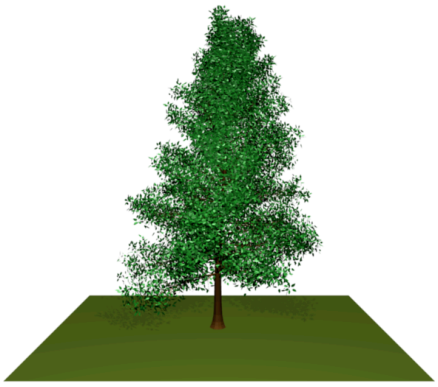

Tree 3: *Nyssa sylvatica*

Tree 4: *Populus tremuloides*

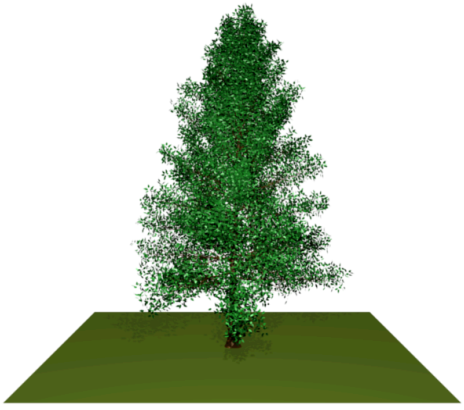

Tree 5: *Nyssa sylvatica*

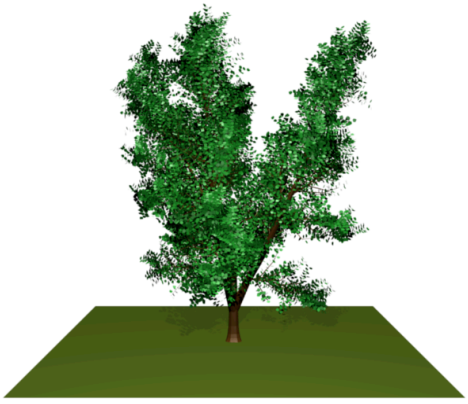

Tree 6: *Populus deltoides*

Figure 2.9. Simulated 3D trees used for waveform simulation and deconvolution assessment.

2.1.3.2 Differentiating herbaceous biomass

The waveform of the return signal is typically distorted as the laser pulse interacts with the layer of grass above ground, e.g., extended widths and peak shifts may occur when compared with the signal reflected from flat, bare ground. This is attributed to the fact that the signal scattered by the above-ground grass is temporally too close to the ground response and thus beyond the temporal or vertical resolution of operational waveform LiDAR systems (e.g., 0.15m). However, the level of distortion theoretically relates to the amount of herbaceous biomass [48]. We used a statistics-based algorithm to extract features from these distorted waveforms for quantitative differentiation of the biomass and to explore the significance of deconvolution in this use case. Figure 2.10 illustrates the workflow of the herbaceous biomass classification algorithm using the simulation data.

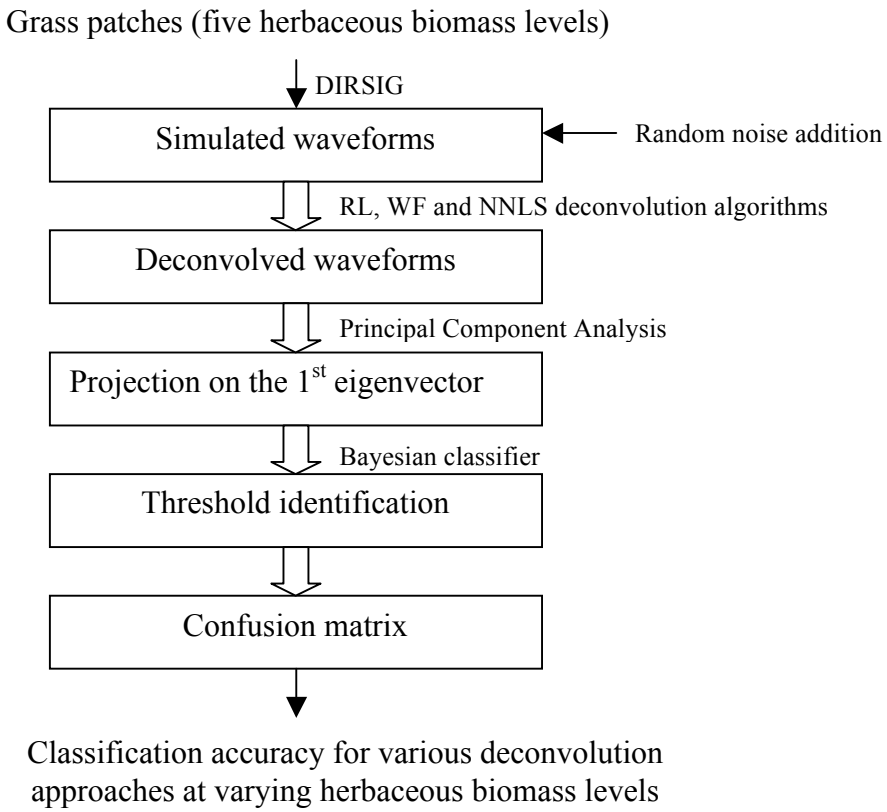

Figure 2.10. Workflow of herbaceous biomass classification algorithm

First, five grass patches with the same area (10x10m^2), but with different herbaceous biomass levels, were created using "Arbaro" (Figure 2.11). The herbaceous biomass was modified by scaling the relative size of each grass facet on a per-patch basis. The scale factor ratios for these five patches were 0.2, 0.4, 0.6, 0.8, and 1. For example, the heights of these grass patches were 0.2m, 0.4m, 0.6m, 0.8m, and 1m, respectively. Since the herbaceous biomass is equal to the product of grass volume and density, and the density was the same for all the patches, their herbaceous biomass ratios were 0.2^3, 0.4^3, 0.6^3, 0.8^3, and 1, respectively. We generated 2000 waveforms in total, with 400 for each patch (20x20 pixels with a 0.5m footprint) using the DIRSIG simulation platform. This was then followed by the application of deconvolution algorithms (RL, WF, NNLS) to the simulated data. Principal component analysis (PCA) [49] was applied to all the simulated waveform data, "*G",* as described below, to identify the vector that contributed most to signal variances. This was done to extract the uncorrelated feature associated with different herbaceous biomass levels from these waveforms, represented in this case by the projection along the first principal axis (Eq. 17). We can thus retrieve the feature that best explains the biomass variance by employing the PCA:

$$Y = a_1^T G \tag{17}$$

where G is the $m \times n$ matrix, in which m is the number of bands for the waveform, n is the total number of waveforms, and a_1 represents the first eigenvector associated with the largest eigenvalue of the covariance matrix of G. Next, we evaluated five different partitioning regions $R_i (i = 1,2,...,5)$ to classify the different biomass levels by minimizing the average risk (Eq. 18) associated with misclassification, defined as a feature vector y that belongs to class ω_k and that lies in $R_i, i \neq k$ [50]:

$$r = \sum_{i=1}^{5} \int_{R_i} \left(\sum_{k=1}^{5} p(y|\omega_k) p(\omega_k) \right) dy \tag{18}$$

where $p(\omega_k)$ is the a priori probability for class k and $p(y|\omega_k)$ is the class-conditional probability density function that describes the distribution of the feature vectors in each of the classes. The partitioning regions R_i can be solved according to the Bayesian

classifier [50], which is optimal with respect to minimizing the average risk. It can be expressed as follows: Assign y to R_i if

$$p(y \mid \omega_i)p(\omega_i) > p(y \mid \omega_k)p(\omega_k) \quad \forall k \neq i \tag{19}$$

Finally, the classification accuracy for deconvolved waveforms from each herbaceous biomass level was assessed using a confusion matrix and by computing the mean of the diagonal values (expressed as the percent classified correctly in each entry).

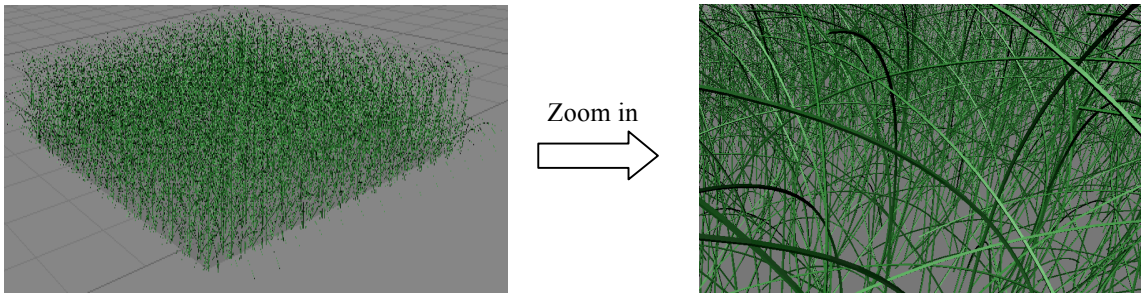

Figure 2.11. An example of a 3D grass patch (the different herbaceous biomass levels were simulated by scaling the relative size of the grass facet while keeping the patch area of 100m^2 constant)

2.1.4 Waveform-to-ground registration

For certain raw LiDAR data formats, e.g., that acquired from the Optech ALTM 3100EA operated by the CAO, the per-pixel based raw LiDAR waveform are assigned to the pixel location where the first interaction between the laser pulse and an above-ground object occurred. All the time bins within that waveform therefore are assumed to align along the same vertical trajectory for that x, y position, i.e., along nadir for that pixel. This 3D waveform registration challenge has not received much attention and we therefore propose a mathematical model for correction of waveform geometry to register each waveform time bin in terms of its x, y, z coordinates in 3D space. This enables a quantitative specification of each waveform time bin's spatial position and provides the mathematical basis for the waveform angular rectification, which will be discussed in the

next section. The basic idea of registration is to tie the time bin associated with the last peak, or last interaction, typically related to the ground response, to the digital elevation model (DEM). The DEM represented the absolute height above sea level (m) for the ground surface, derived from coincident discrete return LiDAR data, which was preceded by the extraction of bare earth (ground) returns using Terrasolid software (V. 008.001). This process enabled the derivation of the relative 3D position for all the other time bins. It should be noted that users may differ in their preference for tying the full-width-half-maximum (FWHM) of the leading or trailing edge of the last peak to the DEM, but this will not change the proposed model. The mathematical derivation, based on Figure 2.12, is presented below:

Displacement along *y*-axis: $S_{y1} = r sin\theta sin\varphi / l$

$$S_{y2}(j) = 0.5c\Delta t(j - N_{lp}) sin\theta sin\varphi / l \tag{20}$$

Displacement along *x*-axis: $S_{x1} = r sin\theta cos\varphi / l$

$$S_{x2}(j) = 0.5c\Delta t(j - N_{lp}) sin\theta cos\varphi / l \tag{21}$$

Actual 3D coordinates for the ground: $X' = X + S_x = X + r sin\theta cos\varphi / l$

$$Y' = Y + S_y = Y + r sin\theta \sin\varphi / l$$

$$Z' = DEM(X', Y') \tag{22}$$

Actual 3D coordinates for j^{th} time bin referenced to the ground:

$$p(j)_x = X' + S_{x2}(j) = X + r sin\theta cos\varphi / l + 0.5c\Delta t(j - N_{lp}) sin\theta cos\varphi / l$$

$$p(j)_y = Y' + S_{y2}(j) = Y + r sin\theta sin\varphi / l + 0.5c\Delta t(j - N_{lp}) sin\theta sin\varphi / l$$

$$p(j)_z = Z' + S_{z2} = Z' + 0.5c\Delta t(N_{lp} - j) cos\theta \tag{23}$$

where

r: slant range (distance between the first and last interaction)

θ: zenith angle

φ: azimuth angle

l : pixel or footprint size (m)

c: speed of light (m/s)

Δt: waveform sampling time (s)

N_{lp}: sample index associated with last peak of the waveform (ground)

j : sample index

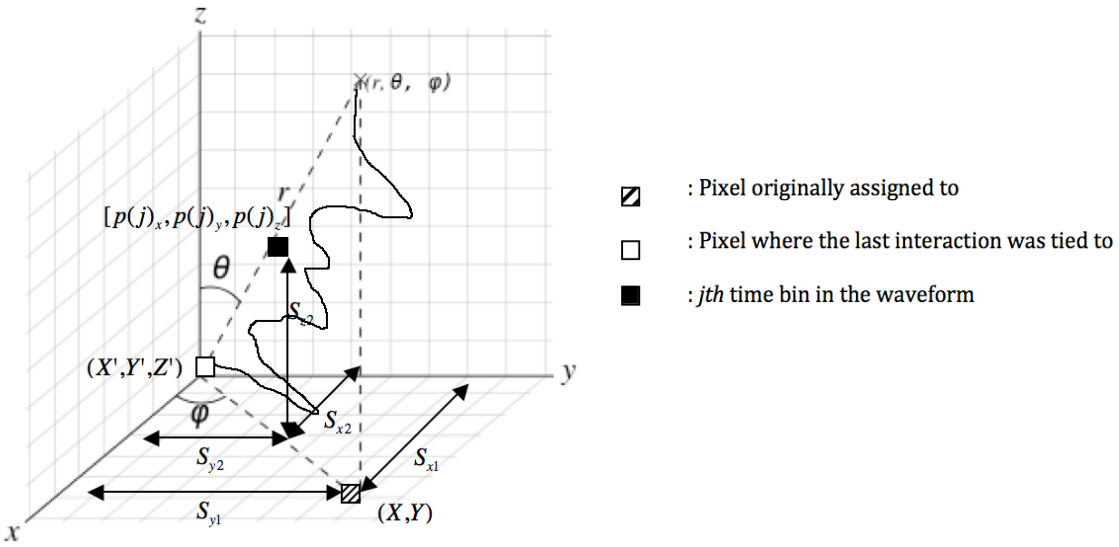

Figure 2.12. Illustration of the waveform registration principles

2.1.5 Angular rectification

The need for angular rectification is justified to address the incorrect practice, as mentioned in the previous section, of assigning all the time bins within each per-pixel waveform to the same horizontal (x, y) location. If we consider the projection of the waveform slant range onto the ground, based on Figure 2.12, and if

$$r_{projection} = r\sin\theta > l\,, \tag{24}$$

we can conclude that an off-nadir waveform potentially could span multiple x,y pixel locations, with the x,y coverage being a function of zenith angle and height above ground of the first interaction. In other words, the waveform originally tied to a single pixel can actually consist of the backscattered signals outside the scope of the horizontal footprint size due to off-nadir scan angles (zenith, θ). Such waveform displacements ($r_{projection}$) should approximate zero or be no larger than the footprint resolution, if we assume the waveform is at nadir ($\theta \approx 0^{\circ}$). However, waveform displacement is quite common in real

waveform data, especially in those regions where the slant range, r, is large. This typically occurs in the case of tall vegetation canopy, as shown in Figure 2.13, based on the CAO data collected in the savanna environment, South Africa. The direction of the vector indicates the azimuth angle and the length is equal the level of waveform displacement ($r_{projection}$) in this angular vector map. The only two directions of azimuth angles in this example result from the mosaicking of two different flight lines for these data. We can conclude that a waveform with zenith angle equal to 7˚, and a footprint size of 0.5m, will result in this displacement problem and associated waveform misregistration when the slant range is greater than 4.1m (Eq. 24) (the canopy vertical height threshold is even smaller). Angular rectification is therefore a critical step for calibrating the raw waveform data.

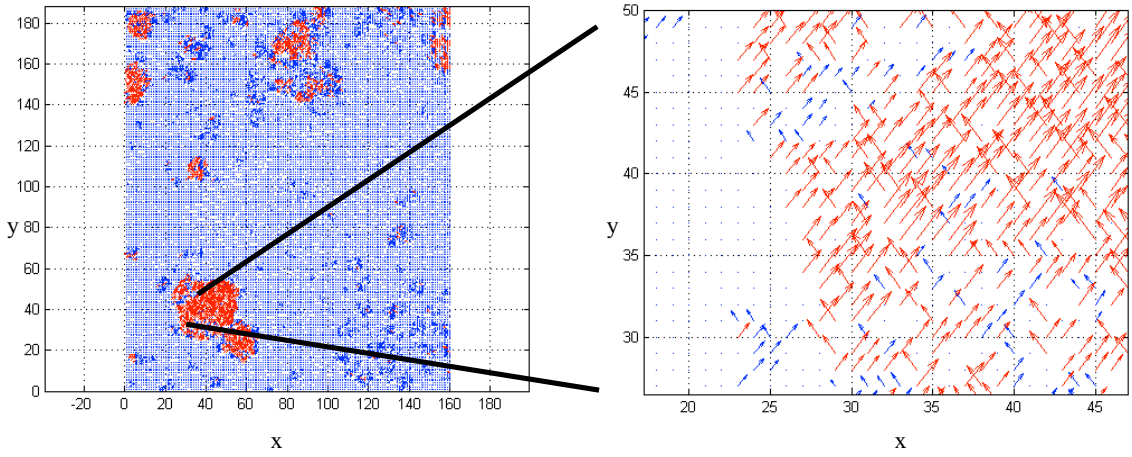

Figure 2.13. Illustration of a waveform angular vector map based on CAO data collected in a savanna area, South Africa; note the displacement of less than one pixel size (blue) and displacement larger than one pixel size (red). The direction of the vector indicates the azimuth angle and the length is equal the level of waveform displacement ($r_{projection}$) in this angular vector map.

We implemented 2D Voronoi natural neighbors interpolation [51-52] to convert each registered time bin in the waveform to the 3D grid version and reconstruct a waveform at true nadir, similar to similar interpolation in the case of a hyper-structural data cube. This was done with consideration that many interpolation algorithms exist to estimate the unsampled value, e.g., from low-level routines to higher order approaches

such as nearest neighbor, linear, quadratic polynomial, piecewise cubic, biquintic, and Kriging [53]. The selection of natural neighbors for angular rectification is justified based on the acceptable tradeoff that this approach provides between computational efficiency and accuracy and because it is extensible to the 3D environment by stacking multiple 2D planes, or height levels.

Harman and Johns [54] also conducted a quantitative comparison of natural neighbors interpolation with a linear and a regularized spline method for the application of generating gridded DEM surfaces from sparse LiDAR point clouds. The authors concluded that natural neighbors interpolation is more capable of dealing with sparse sets of points for interpolation, because the tessellation underlying the interpolation routine extends beyond the boundary of the eventual image, allowing for better interpolation around the boundary of the image relative to other methods. Figure 2.14 shows the procedure of reconstructing the nadir waveform: (a) Each time bin is associated with the proper 3D x, y, z spatial coordinates and intensity information after this waveform registration; (b) Next, we retrieved each x, y pixel plane from the bottom to the top of the waveform at a spatial interval of 0.15m, which is temporally equivalent to the waveform sampling resolution (1ns). The selection of x, y, instead of y, z or x,z planes, is due to the fact that we found invalid responses at certain pixel locations in the real waveform data, which could cause a dark line-like artifact along the y,z or x,z planes; (c) Finally, for each plane, those registered time bins within the corresponding height range will be used as the inputs to interpolation of the grid center, which is the same as the original LiDAR footprint size. Equation 25 shows the basic equation of 2D natural neighbor interpolation:

$$G(x,y) = \sum_{i=1}^{n} w_i f\left(x_i, y_i\right) \tag{25}$$

where $G(x,y)$ is the point to be interpolated, w_i are the weights and $f(x_i,y_i)$ are the known data at (x_i,y_i). Figure 2.15 illustrates the method of natural neighbor interpolation. The area of the circles, which indicates the weights, w_i, are generated using the ratio of the shaded area in the center. The central shaded area is the Voronoi tessellation after inserting the point (black dot) to be interpolated (e.g., points inside the polygon of the shaded polygon are closer to the point to be interpolated than other neighbor points in terms of Euclidean distance). The reader is referred to [54] for more detail on the

implementation of natural neighbor interpolation. The result of this interpolation is a gridded 3D data cube (Figure 2.14 (c)), which has the same spatial resolution as the original LiDAR footprint. The angular-rectified waveform therefore can be retrieved from the column data along the *z* direction associated with each footprint/pixel location.

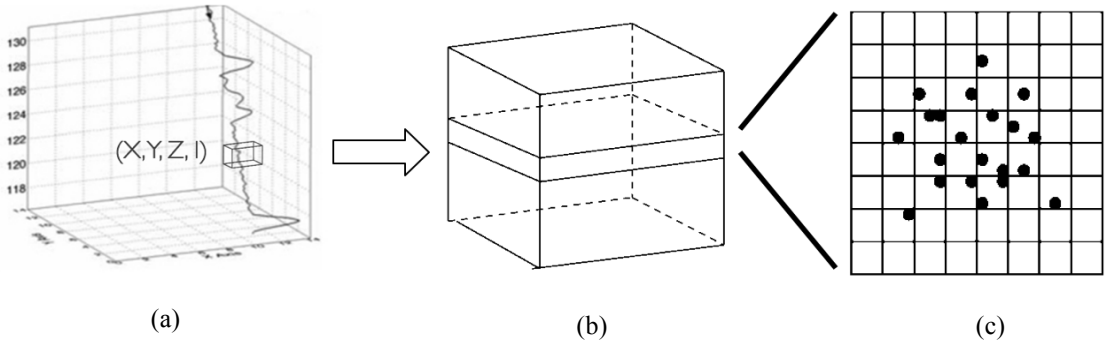

Figure 2.14. An illustration of the gridding process for registered waveform time bins, where (a) shows an example of an off-nadir waveform, (b) shows the vertical sampling plane, and (c) represents the time bins associated with the same absolute height above sea level

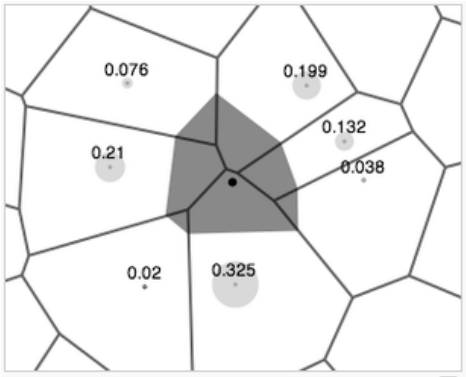

Figure 2.15. Natural neighbor interpolation. Figure taken from the Wikipedia entry on natural neighbor interpolation [52].

2.1.6 Approach to preprocessing chain performance validation

We evaluated our entire proposed preprocessing chain using two approaches: (1) By taking advantage of DIRSIG LiDAR simulation, we were able to simulate the high

fidelity off-angle waveforms interacting with precisely known vegetation structures at various outgoing pulse widths and add typical system noise. These operational simulations were compared to a reference waveform dataset, associated with same vegetation structures, but generated using a narrow outgoing pulse width of 2ns. This was done to approximate the true target cross section along the laser trajectory at nadir, so that we could directly compare the processed waveforms with the truth data; (2) We also applied our methods to real waveform LiDAR data collected by the CAO to further validate impacts of the preprocessing chain in terms of the improvement observed in waveform LiDAR-based woody biomass estimation, along the various steps of the preprocessing chain. We derived the metrics for quantifying the performance of the preprocessing chain in each case as described below.

a) Metrics using simulated waveform LiDAR data

The actual optical path of an off-nadir laser pulse will be longer than that of a pulse collected at nadir, given that one excludes potential multiple scattering effects of photons interacting with vegetation components. Accordingly, the intensity of the backscattered waveform will be more attenuated due to the flux absorption and reflection by vegetation. We therefore can expect that the intensity of the final reconstructed waveform will be attenuated as well, even it can still provide an insight into the overall shape of the truth cross-section at nadir. This is true because the angular rectified waveform needs to be interpolated based on the intensity information at off-nadir conditions. Such intensity attenuation typically cannot be attributed to a linear waveform processing alone, e.g., the attenuation level is typically not a linear function of traveling path due to the complex multiple scattering inside the canopy. We used the spectral angle mapper (SAM) approach [55] to derive the spectral or waveform angle between the processed and reference waveform, or the 2ns outgoing waveform at nadir, as a metric for comparison. The mathematic expression for the spectral angle calculation is shown below and is based on Figure 2.16:

$$\theta = \cos^{-1}\left(\frac{\sum_{j=1}^{N} t_j r_j}{\sqrt{\sum_{j=1}^{N} t_j^2 \sum_{j=1}^{N} r_j^2}} \right) \tag{26}$$

where

t : truth cross-section (nadir reference waveform based on a 2ns outgoing pulse width)

r : reconstructed waveform at nadir

θ : spectral angle (metric)

j : waveform sample index

N : total number of bands

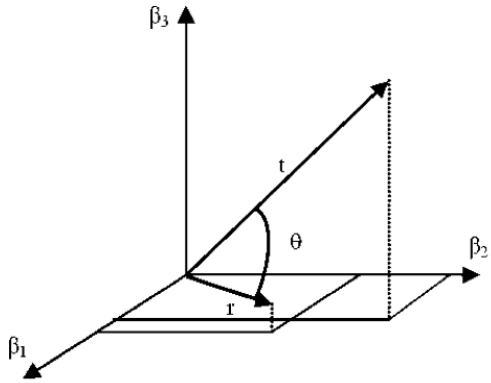

Figure 2.16. Illustration of spectral angle, as calculated using the spectral angle mapper (SAM) approach. Note: only three bands are shown in this example; this metric can be applied to multi-dimensional data

The main advantage of the spectral angle as a comparison metric is that it is based on the overall shape similarity between the simulated-truth waveform pairs, without being affected by the absolute intensity difference. This is especially helpful since we are more interested in recovering the overall shape of the waveform, instead of its absolute intensity level. It is evident from Eq.26 that the calculated angle will be zero if the reconstructed and reference waveforms match exactly, while the most distinguishable pairs will result in a 180˚ angle and the remainder falling in between these two extremes. This approach thus provides a metric for evaluating the accuracy level of the true cross-section recovery, while disregarding the intensity differences between the pairs. Finally, the distribution-free Wilcoxon rank-sum test [56] was used to test the difference of the means of the raw vs. the processed data for 4ns, 8ns, and 16ns outgoing pulse widths. A

test significance level of α=0.05 was used to determine whether a difference existed between the means of the raw and processed data.

b) Metrics using the CAO data

Forward regression analysis has previously been proven useful for estimating woody biomass measurements made at the plot level using structural waveform features as independent variables (R^2 = 0.99, RMSE = 25 Mg/ha) [57-58]. The improvement in signal quality due to application of the processing chain presented in this study therefore was quantified by examining the goodness of fit (R^2) and root-mean-squared error (RMSE) of extracted waveform LiDAR features, used to model tree-level woody biomass during each step of the processing chain. This quantification was examined by way of applying stepwise linear regression to features extracted for individual trees and comparing the biomass calculated from the allometry equations to the biomass calculated by the regression equation, similar to [57-58].

LiDAR waveforms were extracted to represent the known trees using the differentially-corrected GPS coordinates. This was accomplished by employing a region growing algorithm in MATLAB [59] with the seed point set to the GPS coordinate of the tree of interest. Adjacent LiDAR waveforms were chosen using a digital surface model (DSM) generated from the discrete return LiDAR data in order to include only points with DSM values above 3m. This ensured that only waveforms associated with the corresponding tree canopy would be included in the analysis.

Metrics similar to those used by McGlinchy *et al*. [57] were extracted from the processed LiDAR waveforms to estimate woody biomass. A stepwise forward selection, multiple regression procedure was performed on the waveform data to select the variable/s that best explained the variance in the dependent variable, namely woody biomass:

$$\ln(woodybiomass) = \beta_0 + \beta_1 metric_1 + \beta_2 metric_2 + ... + \beta_n metric_n \qquad (27)$$

where metric represents various waveform LiDAR structural variables and β_n represents the respective model coefficients. The regression procedure was performed at each step in the processing chain, from the raw waveform LiDAR to the fully processed waveform

LiDAR. At each step the coefficients changed, but the form of the equation remained the same.

2.2 Results and discussion

2.2.1 Quantitative comparison of deconvolution algorithms

a) Recovering true cross-section

The deconvolved waveforms were compared with the truth data, as approximated by the direct simulation results using an outgoing pulse width equal to 2ns, in order to assess deconvolution in terms of ability to recover the cross-section of a tree plot. Figure 2.17 shows a sample waveform from one of the tree plots, as deconvolved using the RL, WF, and NNLS algorithms.

It was observed that after deconvolution, the width of the local waveform components was decreased and more local peaks were revealed, as we expected when removing the system contribution. The results of the RL and WF algorithms were close to the truth waveforms, as can be seen in Figure 2.17 when comparing them to the true cross-section. However, it was observed that closely-spaced adjacent local peaks could not be distinguished by either RL or WF, which could be due to the resolution of especially the broad the outgoing pulse widths (8ns and 16 ns). We also observed a documented drawback of the WF, called the "ringing effect" [24] caused by the loss of high frequency components during the deconvolution processing. The sum of the remaining low frequency components will introduce a wave-like artifact (a series of rings). This often resulted in extra minor peaks around the major local peaks. Although most of these minor peaks can be removed via filtering, e.g., thresholding, low-pass filtering, etc., it will be difficult to remove them entirely. Results for the NNLS approach proved noisy, given the presence of multiple high frequency peaks. We concluded that NNLS might be more sensitive to finding close-peak neighbors when compared with RL and WF, but the results were not conclusive (Figure 2.17). We also voxelized each waveform by converting every time bin into the "XYZ" coordinate in 3D space and

coding the intensity as rainbow color. This was done to provide a comprehensive comparison in terms of visualization for all the waveforms. Figure 2.18 shows the 3D representations of the voxelized waveforms for tree 6, as an example. It is evident that the deconvolved 3D waveform representations of the truth data agreed well with the real tree geometry, which is indicative of the potential of LiDAR waveforms for 3D tree reconstruction. It was also observed that by changing the width of the outgoing waveform, the 3D representations of the raw waveforms exhibited increasing levels of blur, such that the ground became "thicker" and details inside the canopy were lost. However, after applying the deconvolution, the temporal (vertical) resolution was recovered as the figure shows. The performance of RL and WF was similar when using 8ns as outgoing pulse width, but RL stood out in the case of the larger outgoing pulse width (16ns), when one considers that the ground section associated with WF is thicker and redundant local peaks could be found around the crown and below the ground level. The result for NNLS was obviously not satisfactory relative to the other two approaches, even when based only on visual inspection.

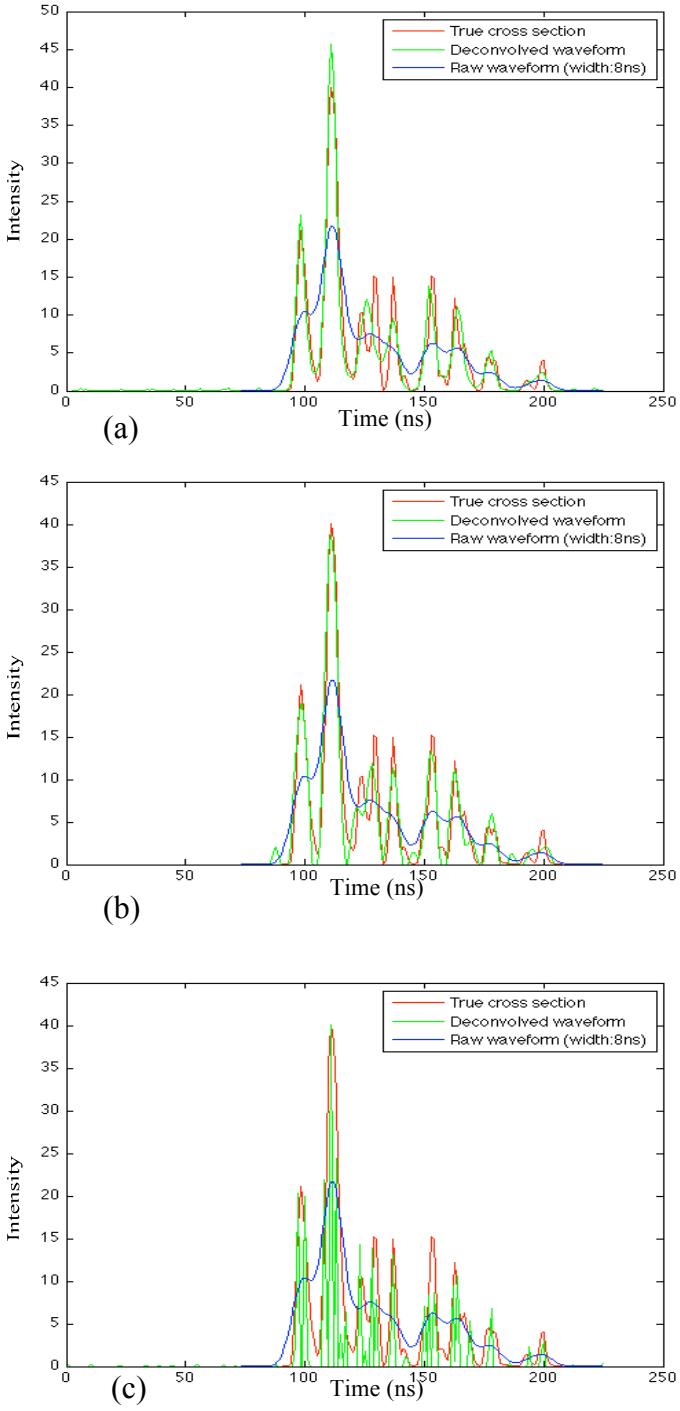

Figure 2.17. An illustration of the deconvolved waveforms for an outgoing pulse width of 8ns: RL (a), WF (b), and NNLA (c).

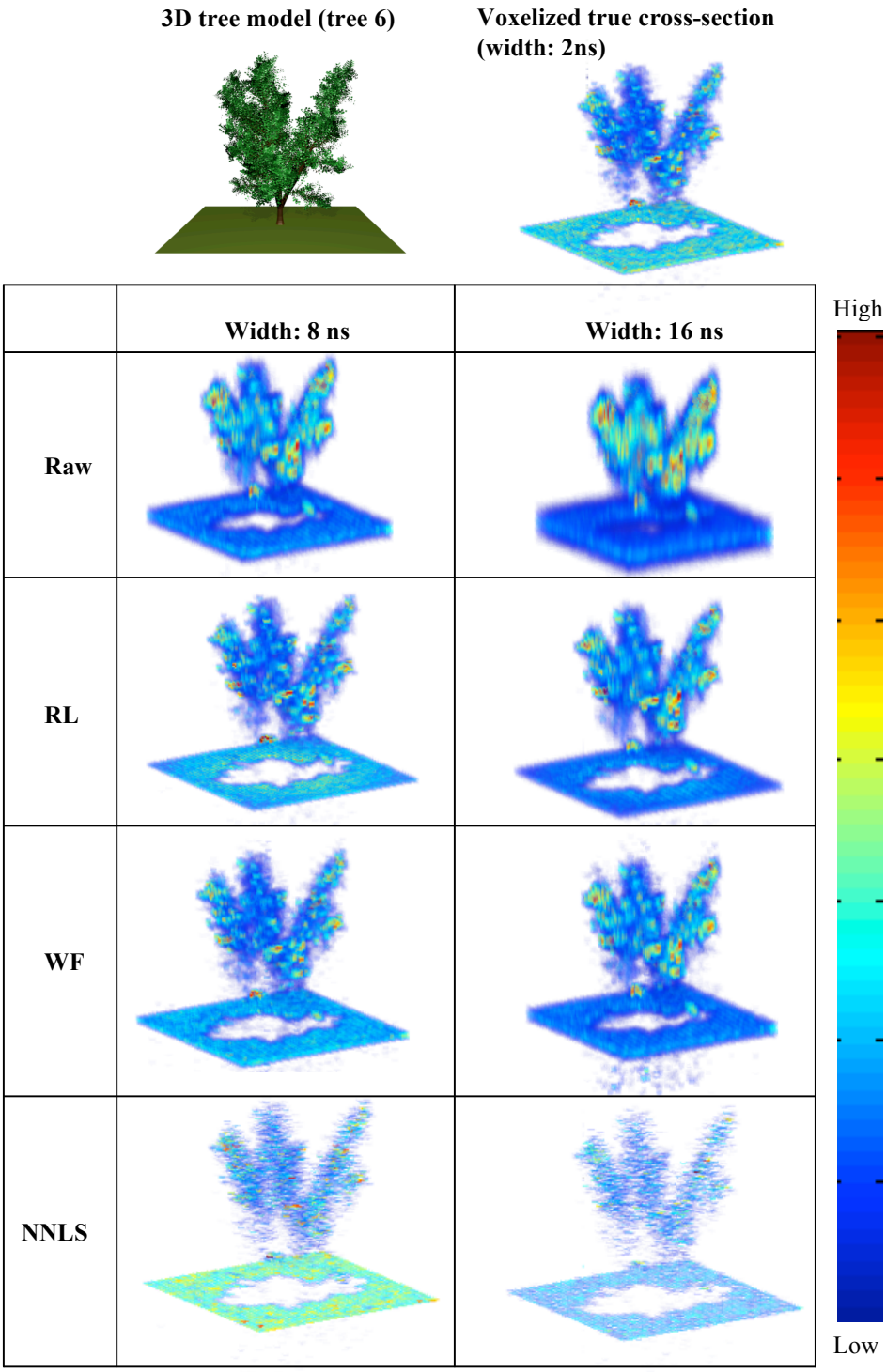

Figure 2.18. A 3D representation of the waveform LiDAR for tree 6 and all deconvolution approaches at 8ns and 16ns outgoing pulse widths.

Figure 2.19 shows the overall quantitative comparison in terms of RMSE (Eq. 14) between the truth and deconvolved waveforms for RL, WF, and NNLS at different outgoing pulse widths (8ns and 16ns). This figure again demonstrates that RL was superior to the other two approaches. The results also show that the selection of the width for the outgoing pulse could significantly affect the deconvolution outcome. The assessment of deconvolution accuracy using RMSE was expanded by evaluating if the location of peaks in each deconvolved waveform corresponded to those found in the truth data waveform (non-deconvolved; 2ns outgoing pulse width). Figure 2.20 shows the point clouds associated with the extracted peaks from various waveforms, similar to the output of discrete return LiDAR systems. Figure 2.20(a) shows the LiDAR returns from the truth data of tree 5, as an example. Points located below the ground level typically correspond to the minor peaks after the ground response, which are attributed to the multiple scattering of the photons inside the crown.

Figure 2.20(b) shows the result using the raw simulated waveforms prior to deconvolution; it is evident that the density of the points decreased due to the loss of temporal (vertical) resolution caused by the system and noise contributions. To a large extent, deconvolution can reveal peaks hidden by this unwanted system interference; however, it could also introduce artifacts in the form of non-existing returns due to the noise as Figure 2.20(c) shows. We further compared these detected points with those from the truth waveforms and determined the correct peak detection shown in Figure 2.20(d). The overall statistics are listed in Table 2.3. The quantitative results indicated that (i) deconvolution (RL, WF, and NNLS) dramatically increased the density of the point clouds, compared with the raw data, (ii) as we increase the width of the outgoing pulse, the effect of deconvolution is negated, and (iii) the fact that only about half of the detected peaks after deconvolution (RL, WF, and NNLS) matched the ground truth data, suggests that no deconvolution algorithm can fully recover the full temporal response for these waveforms. This can be observed from Figure 2.18, where for certain close-peak neighbors, the deconvolution approaches were unable to uncover both peaks, but resulted in a peak detection in-between. This is arguably still useful for vegetation applications, but it effectively represents a false detection, even if this “false” detection is representative of target interaction on either side. The quantitative analysis was

concluded by assessing two final metrics: sensitivity and false discovery rate, based on Eq. 15 and Eq. 16, respectively, and plotted in Figure 2.21.

It is evident that all of the deconvolution algorithms enhanced the detection sensitivity when compared with the raw data. NNLS performed the best in terms of the sensitivity among these three deconvolution algorithms. However, this increased sensitivity came at the cost of a higher false discovery rate for the NNLS algorithm. For example, NNLS resulted in more peak detections, which increases the probability of detecting a true response for a given time bin. On the other hand, this boost in point density resulted in more false detections due to the noise, or application of the algorithm itself. Therefore, if minimization of the false detection is the most important consideration, the RL algorithm still appears to be the best choice.

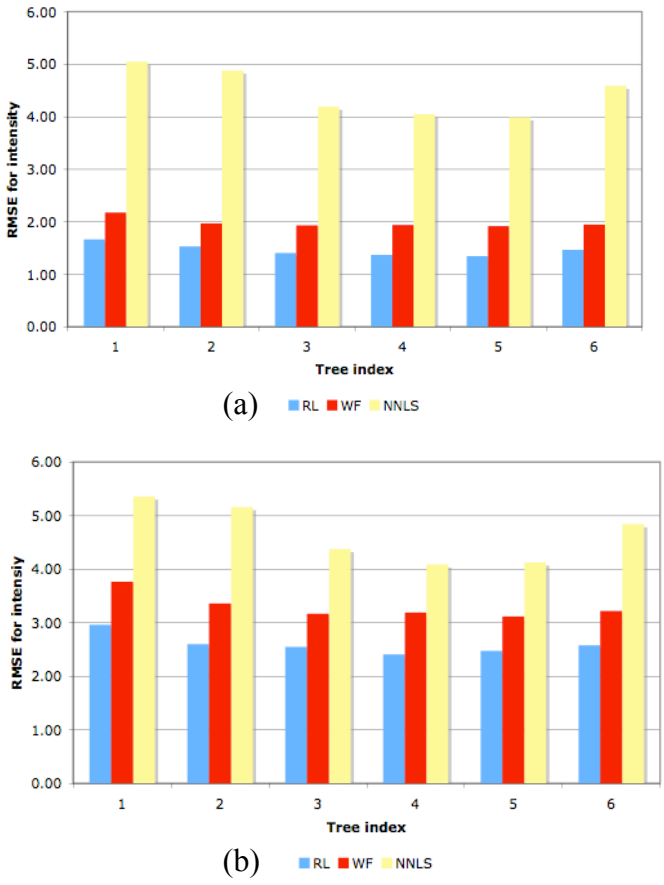

Figure 2.19. Results of the RMSE comparison for outgoing pulse width 8ns (a) and 16ns (b)

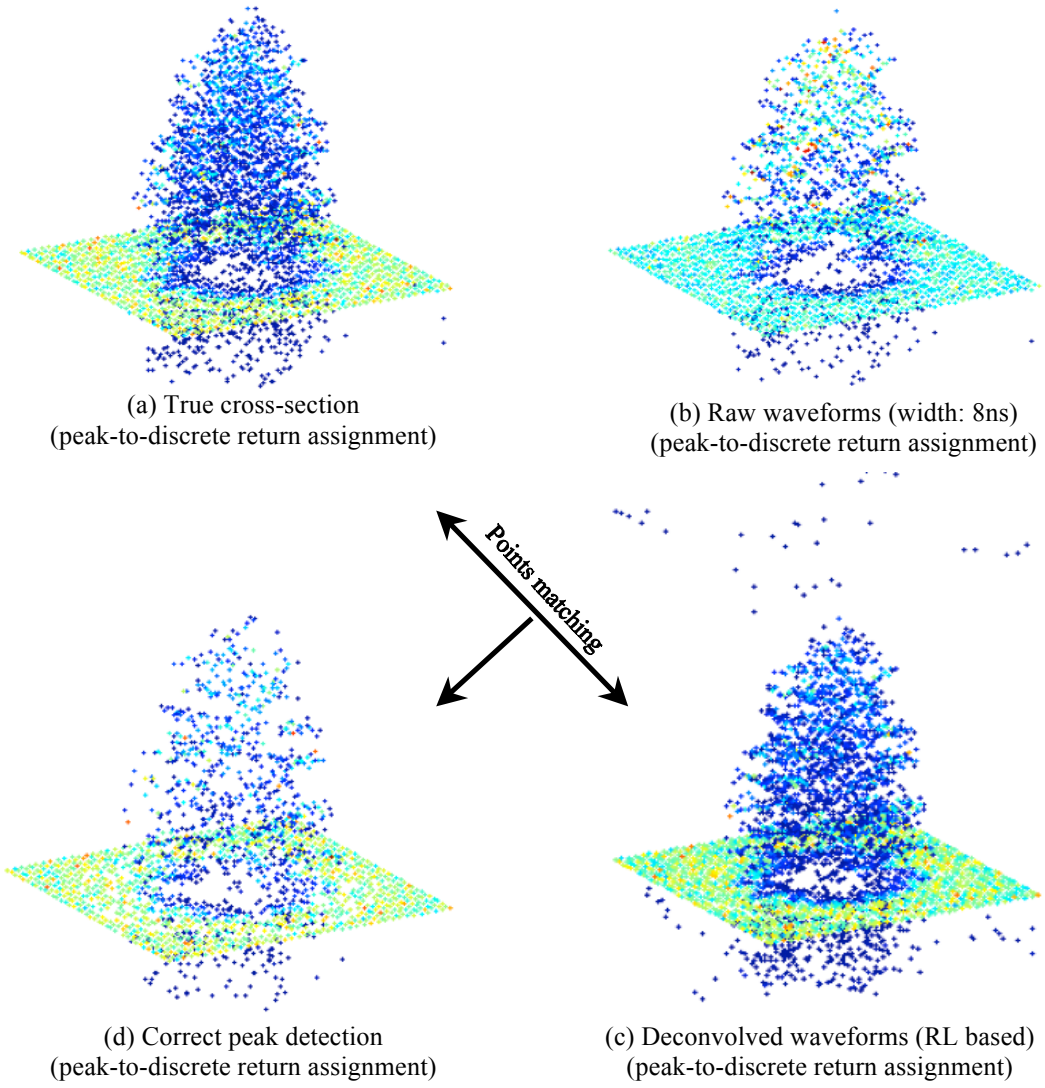

Figure 2.20. Point clouds extracted from the local peaks of the waveforms (Tree 5). The point clouds are colored according to the intensity. (a) Extracted from waveform using 2ns outgoing pulse width, (b) Extracted from raw waveform using 8ns pulse width, (c) Extracted from deconvolved waveforms (RL), (d), Matched points between (a) and (c)

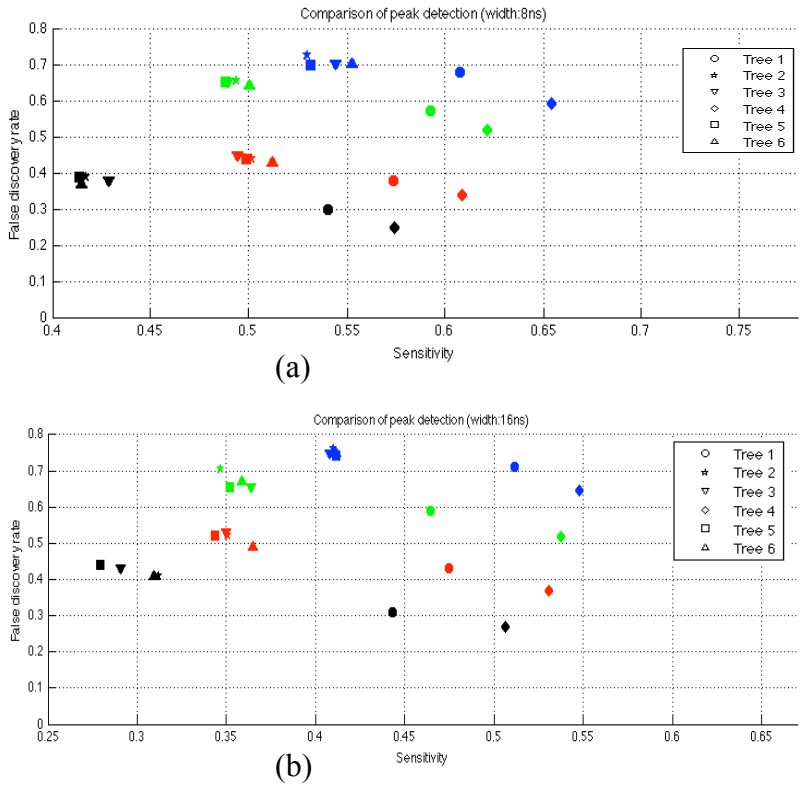

Figure 2.21. False discovery rate vs. sensitivity for 8ns (a) and 16ns (b) outgoing pulse widths, with raw (black), RL (red), WF (green), and NNLS (blue) waveforms.

TABLE 2.3
STATISTICS OF THE PEAK DETECTION RESULTS. (A: TOTAL # OF DETECTED PEAKS, T: # OF PEAKS THAT MATCH THE TRUTH WAVEFORM, ALL THE VALUES ARE NORMALIZED BY COMPUTING THE RATIO TO THE # OF PEAKS AT 2NS AS THE PERCENTAGE SHOWS)

		Tree 1		**Tree 2**		**Tree 3**		**Tree 4**		**Tree 5**		**Tree 6**	
		8ns	**16ns**	**8ns**	**16ns**	**8ns**	**16ns**	**8ns**	**16ns**	**8ns**	**16ns**	**8ns**	**16ns**
Raw	A	2224 77%	1852 64%	2657 68%	2056 53%	2697 69%	1988 51%	2054 77%	1860 69%	2758 68%	2031 50%	2493 66%	1985 52%
	T	1557 54%	1278 44%	1621 42%	1213 31%	1672 43%	1133 29%	1541 57%	1358 51%	1682 41%	1137 28%	1571 41%	1171 31%
RL	**A**	2666 93%	2401 83%	3479 90%	2842 73%	3506 90%	2903 74%	2474 92%	2260 84%	3625 89%	2913 72%	3401 90%	2711 72%
	T	1653 57%	1369 48%	1948 50%	1364 35%	1928 49%	1364 35%	1633 61%	1424 53%	2030 50%	1398 34%	1939 51%	1383 37%
WF	**A**	4003 139%	3255 113%	5560 143%	4553 117%	5482 141%	4102 105%	3467 129%	2995 112%	5704 140%	4138 102%	5288 140%	4118 109%
	T	1708 59%	1338 46%	1919 49%	1347 35%	1908 49%	1419 36%	1666 62%	1441 54%	1986 49%	1433 35%	1895 50%	1358 36%
NNLS	**A**	5448 189%	5101 177%	7467 192%	6632 171%	7106 182%	6343 163%	4280 160%	4134 154%	7178 176%	6474 159%	6979 184%	6227 164%
	T	1751 61%	1475 51%	2059 53%	1594 41%	2123 54%	1590 (41%)	1754 65%	1470 55%	2163 53%	1674 41%	2093 55%	1558 41%

Hence, based on these quantitative tests (classification accuracy, RMSE, peak detection) of three deconvolution algorithms, we concluded that RL is superior to the other approaches. This corroborated the findings of Harsdorf that the 1-dimensional Richardson-Lucy algorithm leads to the best results, as per a visual comparison between an arbitrary designed pre-deconvolved and post-deconvolved waveform [26]. But our approach provides a more comprehensive and quantitative comparison, both in the direct 3D recovery accuracy for the truth waveform and the application of the deconvolved waveforms (biomass classification). This was underscored by statistic-based metrics towards measurement of the quality of the deconvolution algorithms applied to LiDAR waveforms, thereby quantifying the advantages and disadvantages of the different algorithms.

b) Differentiating herbaceous biomass

Figure 2.22 illustrates one of the simulated waveform pairs from the grass patches with five different herbaceous biomass levels, where patch 1 represents the lowest and patch 5 the highest biomass. These waveforms have a wider distribution and are more spread out prior to deconvolution, especially in the leading edge (a) area. The peaks also shift to the left, or closer to the sensor, as the biomass increases. This can be explained by considering that before the laser pulse hit the ground, it interacted with above-ground grass, which backscattered part of the energy before the backscatter event/s that occur closer to the ground. This led to an increase of width for the return signal, which became even more obvious after applying the deconvolution, shown in Figure 2.22 (b).

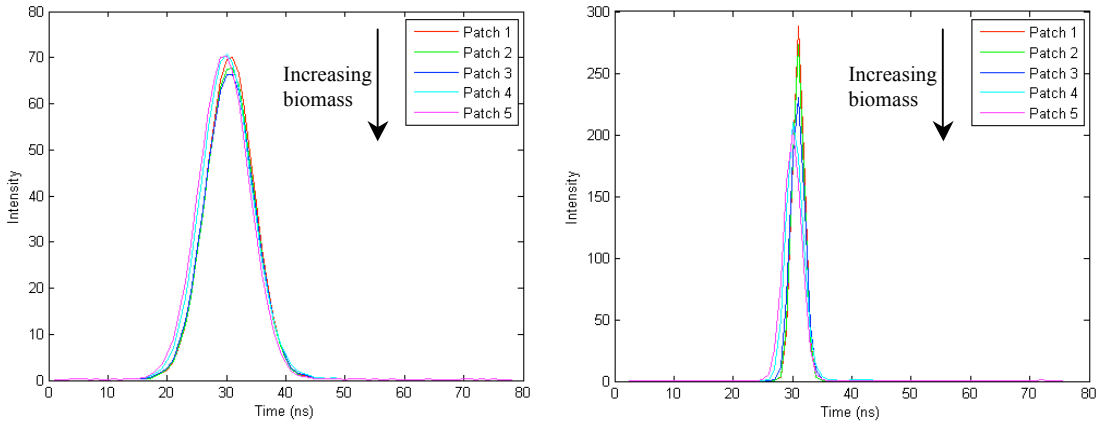

(a) (b)

Figure 2.22. Simulated waveforms from grass patches: (a) before deconvolution, and (b) after deconvolution. Herbaceous biomass ratios from patch 1 to 5 were 0.2^3: 0.4^3: 0.6^3: 0.8^3: 1. The plots are based on the RL deconvolution algorithm with an outgoing pulse width equal to 8ns.

In order to better explain the classification algorithm, we can consider the results of post-deconvolution waveforms, using RL as an example. Figure 2.23 shows the statistics-based feature extraction using PCA. It was observed that more than 99% of the variance of the deconvolved waveforms can be explained by the first four eigenvectors associated with the largest eigenvalues in descending order, in which the first eigenvector contributed approximately 82% of the variance. If we evaluate the shape of the first eigenvector shown in red in Figure 2.23 (b), it is clear that two local peaks with negative and positive values, respectively, can be related to the grass and ground scene components. The reverse signs of the intensity also suggest the tradeoff of energy contribution to the original waveform between the grass layer and ground. For example, the more positive energy from the ground contributed to the original waveform, the more energy associated with the grass component will be subtracted, and vice versa. This observation agrees with the plot in Figure 2.22, i.e., that those waveforms from low biomass levels typically exhibit high intensity at the ground component, and relative less energy from the leading (left) edge, which corresponds to the energy contribution from grass. These simulation results also corroborate previous research about the existence of a

correlation between waveform shape metrics and the presence of varying levels of herbaceous biomass in the real world [48]. The 2nd, 3rd, and 4th eigenvectors were used to explain the slight peak shift across different biomass levels observed in Figure 2.22, since the peaks of these eigenvectors are obviously spread out (Figure 2.23 (b)).

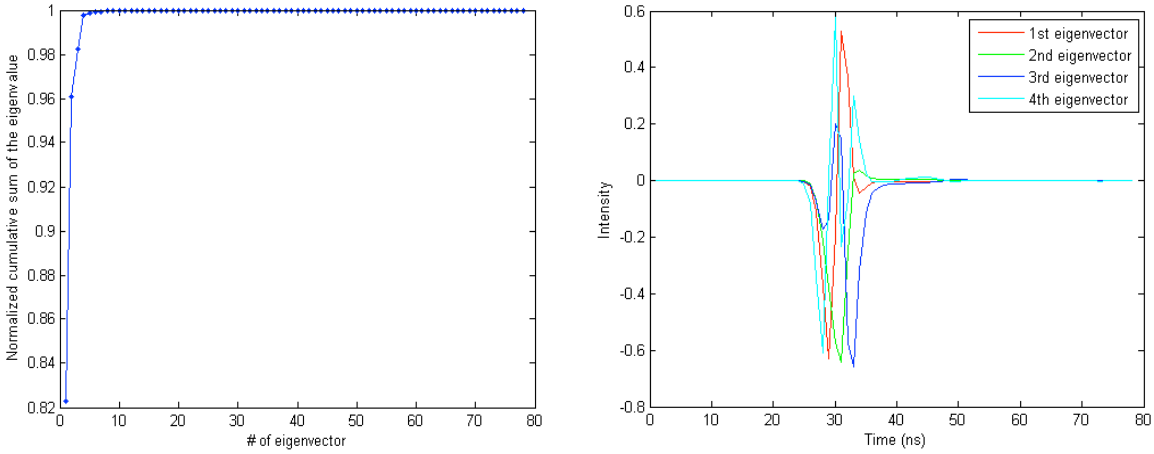

(a) (b)

Figure 2.23. (a) Plot of the normalized cumulative sum of the eigenvalues for the simulated waveforms from grass patches; (b) Eigenvectors associated with the four largest eigenvalues in descending order.

Figure 2.24 (a) shows the scatter plot of the projection onto the 1st vs. 2nd eigenvectors (color index is the same as in Figure 2.22). We can see that the points are separable in terms of different grass biomass levels along the *x*-axis, which corresponds to the projection on the 1st eigenvector. This observation agrees with the most significant contribution, i.e., grass structure, from the 1st eigenvector. It also shows that points associated with large herbaceous biomass (magenta, cyan), are basically located in the negative region along the *x*-axis. This suggests that the negative local peak, which was assumed to correspond to the grass layer in the 1st eigenvector, contributed positively to the final return signal. The inverse is true for the second ground-related peak. This effectively resulted in a shift of the return waveform to the left and with a larger width. It was also observed that the low biomass patches (red and green points) were relatively similar, which was attributed to the herbaceous biomass not being linearly separated in the design of the grass patches, e.g., the ratios were 0.2^3: 0.4^3: 0.6^3: 0.8^3: 1. We

assumed that the distribution of the projection values follow a normal distribution, as shown by the histogram fitting using a Gaussian curve (Figure 2.24 (b)). This was done in order to identify the thresholds for classifying the grass patches. The partitioning regions were computed using Eq. 19.

Finally, the classification accuracy was assessed using a confusion matrix (see Table 2.4 as an example); the results are summarized in Figure 2.25. Four conclusions can be drawn from Figure 2.25:

1. Deconvolution (RL, WF, and NNLS) improved the classification accuracy when compared with the results using the raw data without deconvolution, while the widths of the outgoing pulse were set to 8ns and 16ns.
2. RL stood out in terms of the accuracy when compared to WF and NNLS.
3. The width of the outgoing pulse affected the classification results in that large widths negated the effect of deconvolution processing.

   When the width of the outgoing pulse was set to 2ns, the classification accuracy, based on waveforms without deconvolution was better than accuracies for deconvolved waveforms. This corroborated our assumption, stated in section IV, that we can use the simulation results for outgoing pulses with a narrow width to approximate the true target response as reference for comparing different deconvolution algorithms.

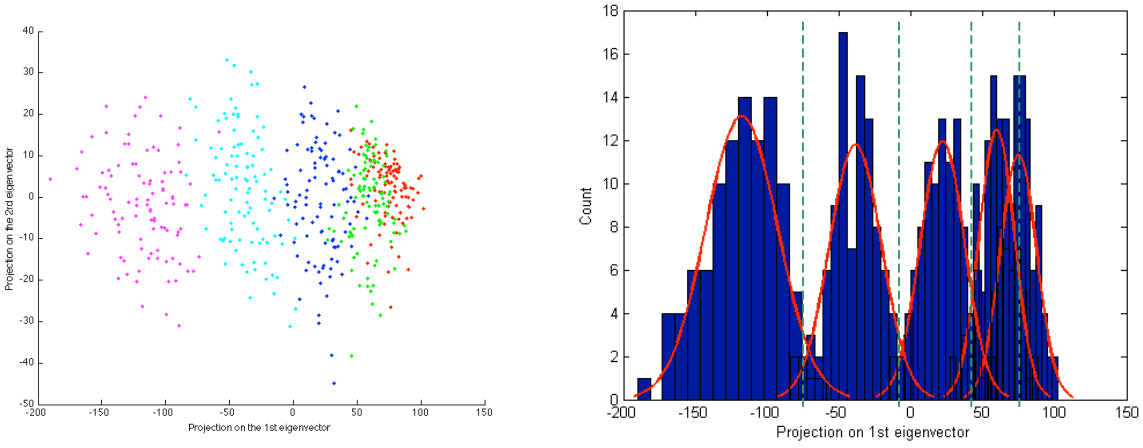

(a) (b)

Figure 2.24. (a) Projection on the 1st eigenvector vs. projection on the 2nd eigenvector. (b) Histogram of the projection on the 1st eigenvector.

TABLE 2.4
ILLUSTRATION OF CONFUSION MATRIX USED FOR ASSESSING THE ACCURACY OF HERBACEOUS BIOMASS CLASSIFICATION (BASED ON RL)

		% Classification				
	Herbaceous biomass levels	1	2	3	4	5
Reference	1	74%	25%	1%	0	0
	2	26%	66%	8%	0	0
	3	0	11%	85%	4%	0
	4	0	0	4%	91%	5%
	5	0	0	0	1%	99%

Overall accuracy: 83%

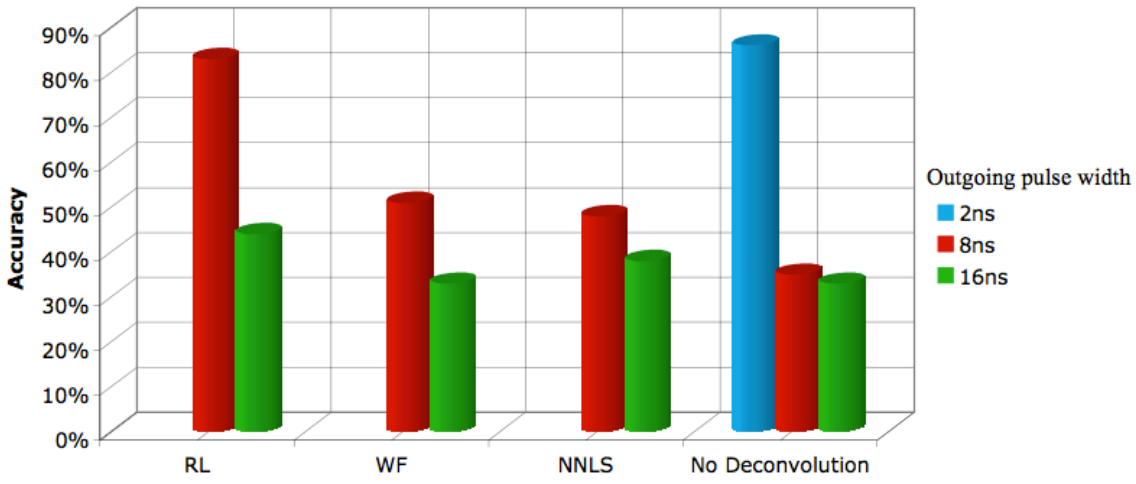

Figure 2.25. Comparison of the classification accuracy for no deconvolution and the three deconvolution algorithms in question.

2.2.2 Preprocessing chain validation

Insofar as the distribution-free Wilcoxon rank-sum test is concerned, it was shown that the means of the raw versus processed data were significantly different at a test significance level of 1% ($p<0.01$) for the 4ns, 8ns, and 16ns outgoing pulse widths. This conclusively proved that the preprocessing chain resulted in significant changes to the

unprocessed data, but not if the changes resulted in more accurate waveforms. The SAM comparison effectively addressed the second issue.

Figure 2.26 (a) illustrates the 3D representation of voxelized waveforms from the raw DIRSIG simulation data at off-nadir angles (zenith=5°) for 40×40 pixels with 121 bands for each footprint and a voxel size of 0.5m×0.5m×0.15m (x, y, z). The voxels are coded in rainbow scale according to the waveform intensity of each time bin. Figure 2.26 (b) shows the representation of the truth data by implementing the same simulation via DIRSIG at nadir, but using 2ns as the outgoing pulse width for approximating the near perfect system response. Figure 2.26 (c) shows the fully processed waveform following the application of the entire preprocessing chain, which allows for a visual comparison between the processed and the truth waveforms. The spectral angle between these two data sets subsequently was calculated to quantify the difference. It is observed from Figure 2.26 (a) that the off-nadir raw waveform data are misaligned - observe the tilt of the ground and tree. The signal is furthermore stretched or smeared because of the imperfect outgoing pulse and system impulse response, which effectively results in a decrease in vertical (temporal) resolution. However, by applying the preprocessing chain for waveform calibration, we can observe that the tilt artifact is corrected, while the noise reduction and deconvolution also significantly improved the signal's sampling time and the details of the tree structure. This latter aspect is best observed by comparing the crown profile of truth, raw, and processed waveform data.

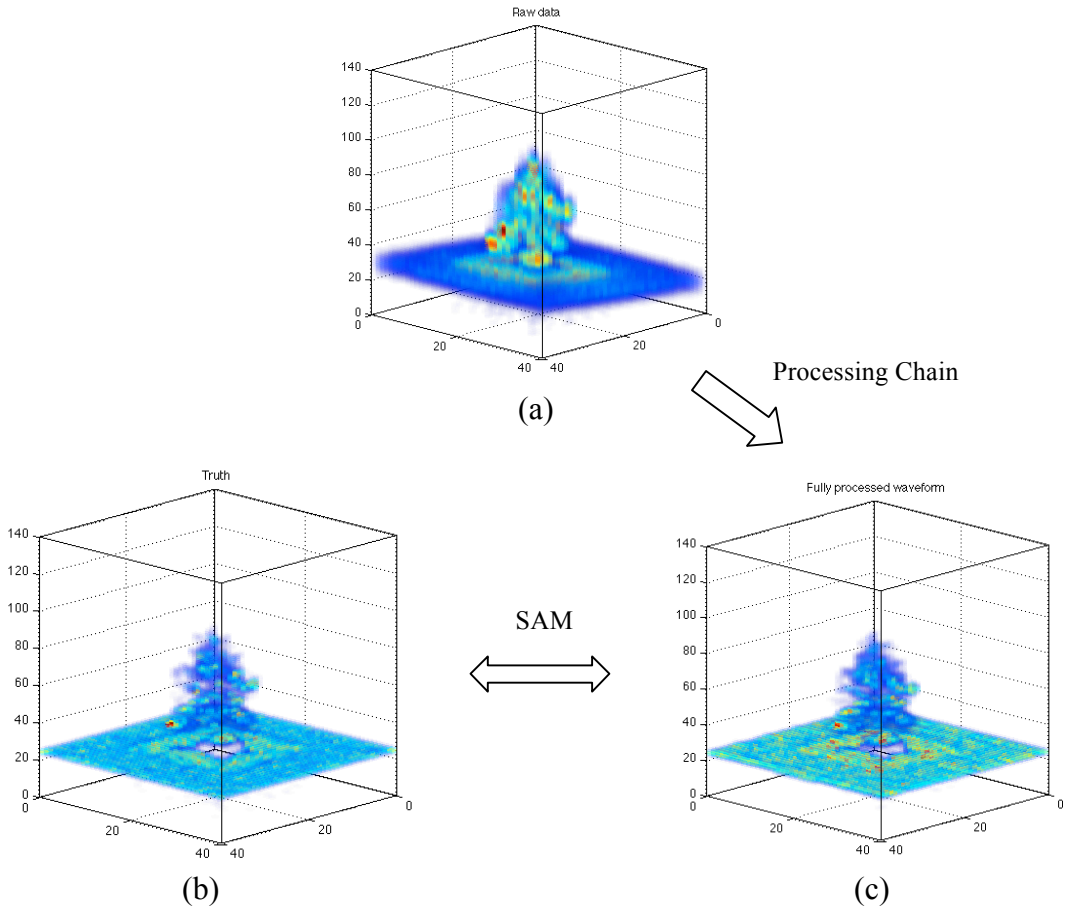

Figure 2.26. A 3D representation of the voxelized waveforms. (a): Raw waveform (8ns pulse width, zenith=5°). (b): Truth waveform (2ns pulse width). (c): Fully processed waveform.

Figure 2.27 provides a stepwise numerical evaluation of the preprocessing chain performance based on the SAM comparisons (smaller angles are preferable). The x-axis of the bar plot represents the processing step (from raw to fully processed), while the y-axis is the spectral angle in degrees. Five different gray intensities were used to represent the zenith angle conditions, given that the performance of the chain also depends on the magnitude of the zenith angle. The height of each bar represents the average spectral angle across all 1600 simulated waveforms at four different azimuth angles, with an associated error bar that represents the standard deviation of the angle distribution in each case. For the final step, namely angular rectification, the interpolation was based on four

different data sets which corresponded to the four azimuth angles. Five conclusions can be drawn from these results (Figure 2.27):

(1) The spectral angle between the processed and truth, at-nadir waveforms by direct simulation using 2ns outgoing pulse width increases as the off-nadir angle (zenith) increases. The trend becomes more obvious when the outgoing pulse width is relatively narrow, as evidenced by a comparison between the results for 4ns, 8ns and 16ns waveforms. This is caused by misregistration of the waveform time bin, e.g., when one takes the ground response as an example: the location of the Gaussian-like peak in a waveform shifts to the left or right under off-nadir conditions. When the outgoing pulse width is broad, these shifted ground peaks and the truth data will have large overlaps, resulting in comparatively insignificant spectral angles when compared to narrow outgoing pulse widths. Here the shift results in less overlap or even gaps between the ground peaks. This is shown in the first bar of the raw data in Figure 2.27.

(2) The most significant improvement in the case of nadir waveforms occurs during the deconvolution step, while waveform registration has the biggest impact on spectral angles in the case of off–nadir waveforms. This can be explained by considering that the waveforms are in theory perfectly registered for each time bin at nadir zenith angles, where most of the signal degradation is caused by the loss of temporal resolution, which in large part can be recovered during the signal deconvolution. However, both temporal resolution loss and waveform misalignment have an impact on the spectral angles between raw and processed data at the off-nadir angles. Although the deconvolved waveforms without registration resulted in a closer approximation of the truth waveforms, one can still end up with large spectral angles if the time bins were slightly shifted compared to the truth data.

(3) We also observed that for the off-nadir angles, as the preprocessing chain progresses to the deconvolution step, the spectral angles actually increased when compared to the previous steps. This was attributed to the situation mentioned in conclusion (1): The overlap area between the shifted waveform and the corresponding truth data decreases when the pulse width becomes narrower. The deconvolution processing actually decreases the width of the waveform in the same way, which inversely

increases the spectral angle. In extreme situations, a 90° angle results from a condition of complete non-overlap between the shifted deconvolved waveform and truth data, which typically occurs at the single ground peak. However, such an inverse spectral angle condition is temporary and it does not imply that the deconvolution has a negative impact on waveform calibration. As long the waveform registration and angular rectification are applied, the spectral angle will be significantly reduced again.

(4) The effect of angular rectification is not that obvious in this experiment, but we still observed a marginal improvement or decrease of the spectral angle, especially for large zenith angle conditions, e.g., zenith=15, 20.

(5) The outgoing pulse width impacts the accuracy of the preprocessing chain, which is evident when comparing the final results between the 4ns, 8ns, and 16ns outgoing pulse widths. We concluded that better results, i.e., smaller spectral angles between truth and processed data, are possible for waveforms with narrower outgoing pulse width after applying the processing chain.

It can be observed from Figure 2.27 that waveform registration and angular rectification contribute significantly to the preprocessing chain, especially for off-nadir waveforms. Figure 2.28 shows an example by presenting four waveforms, corresponding to the same pixel location but associated with four different azimuth angles, 0°, 90°, 180°, and 270°, and the final reconstructed nadir waveform, based on these four off-nadir signals after registration and angular rectification. A direct comparison reveals that none of the off-nadir waveforms has a shape similar to the truth waveform, since certain time bin responses are from that pixel's neighbors, as mentioned earlier. However, after applying the preprocessing chain for waveform registration and angular rectification, the reconstructed waveform exhibits a form that is much closer to the truth signal in terms of the shape and locations of major peaks. Although a marginal difference still exists, the result is generally much improved when compared to unprocessed data.

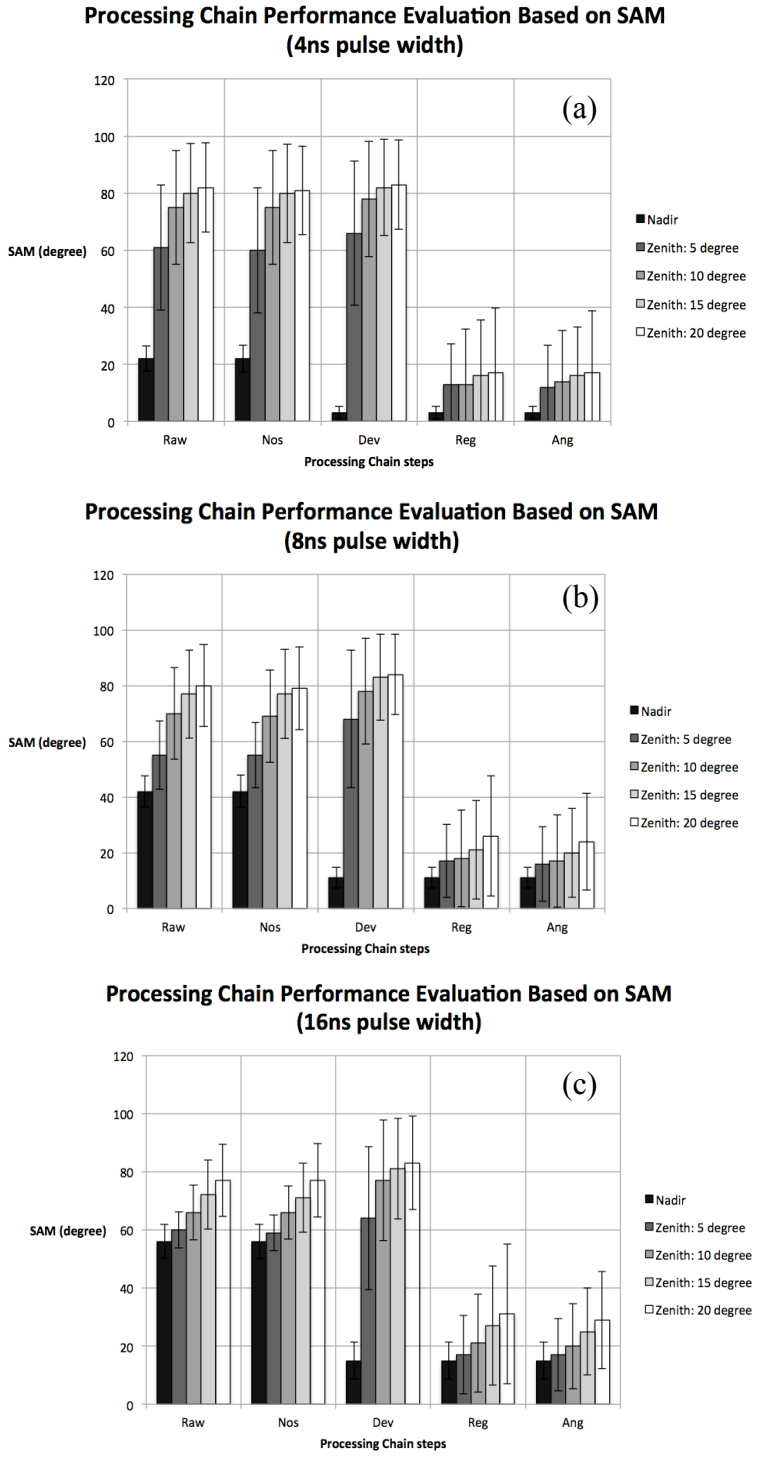

Figure 2.27. Stepwise evaluation of the processing chain performance; 4ns (a), 8ns (b) and 16ns (c) outgoing pulse widths. Raw (Raw data), Nos (Noise Reduction), Dev (Deconvolution), Reg (Registration), Ang (Angular Rectification)

.

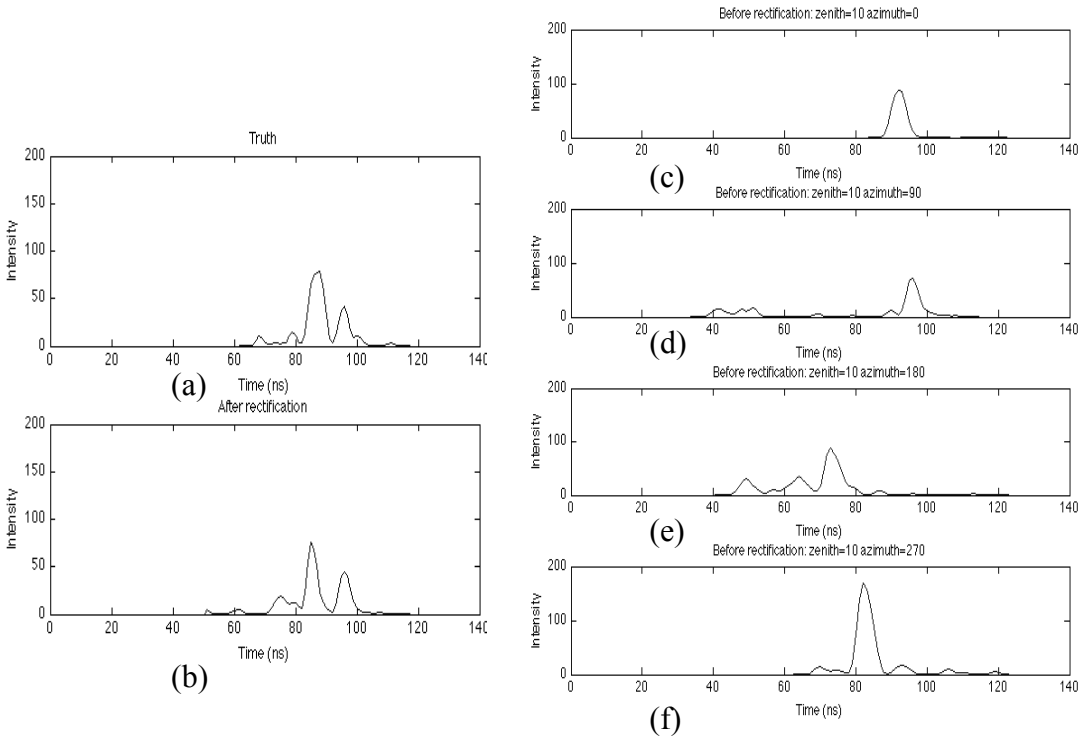

Figure 2.28 An illustration of the impact that waveform registration and angular rectification have on the processing of waveform LiDAR signals. The truth waveform (a) is compared to the reconstructed waveform (b) after registration and angular rectification. The various off-nadir waveforms are shown before processing for azimuths 0°, 90°, 180°, and 270°, and a zenith of 10° for all (c,d,e,f)

In addition to the validation using simulated waveforms, we also applied the preprocessing chain on the real CAO data. The values of the waveform LiDAR metrics, extracted as independent variables for modeling woody biomass, change after each step in the processing chain. This is evident in Figure 2.29, where the 10-90% duration was mapped for a site within the study area after each stage of the waveform processing. After applying the signal detection threshold and de-noising the data, there were areas where no waveforms were detected, i.e., black dots scattered across the site are representative of no data. This is in contrast to the unprocessed data representation, but arguably more representative of the actual laser-vegetation interactions for the given collection settings.

The results of the regression procedure in terms of accuracy and precision of the biomass modeling are shown on the Figure 2.30 (a) and Figure 2.30 (b), respectively. It is evident that there were distinct trends in terms of an increase in model fit (R^2) and an associated decrease in model error (RMSE) as the waveform processing progressed. The RMSE graph on the Figure 2.30 (b) shows large error bars for the RMSE calculation. This was attributed to the distribution of woody biomass available in the data set. Almost 70% of the allometry-estimated, field-based woody biomass measurements fell below 3000kg (Figure 2.31). These smaller measurements most often result in incorrect predictions and contribute heavily to the large RMSE at each stage of processing due to the limitation of the waveform spatial resolution.

The slight decrease in model performance from the registration step to the angular rectification step of the processing chain was attributed to the manner in which the LiDAR data were acquired. Only one flight line was available for this area, limiting the waveform acquisition to a single pass. This resulted in the availability of approximately 50% of the pixels containing waveform data, where the remaining pixels' waveform data had to be interpolated at the final step of the processing chain. This had an obvious negative effect on the modeling approach. Even so, the net effect of the waveform LiDAR signal processing chain yielded an increase in the accuracy and precision of the woody biomass model, which further validated the processing approach.

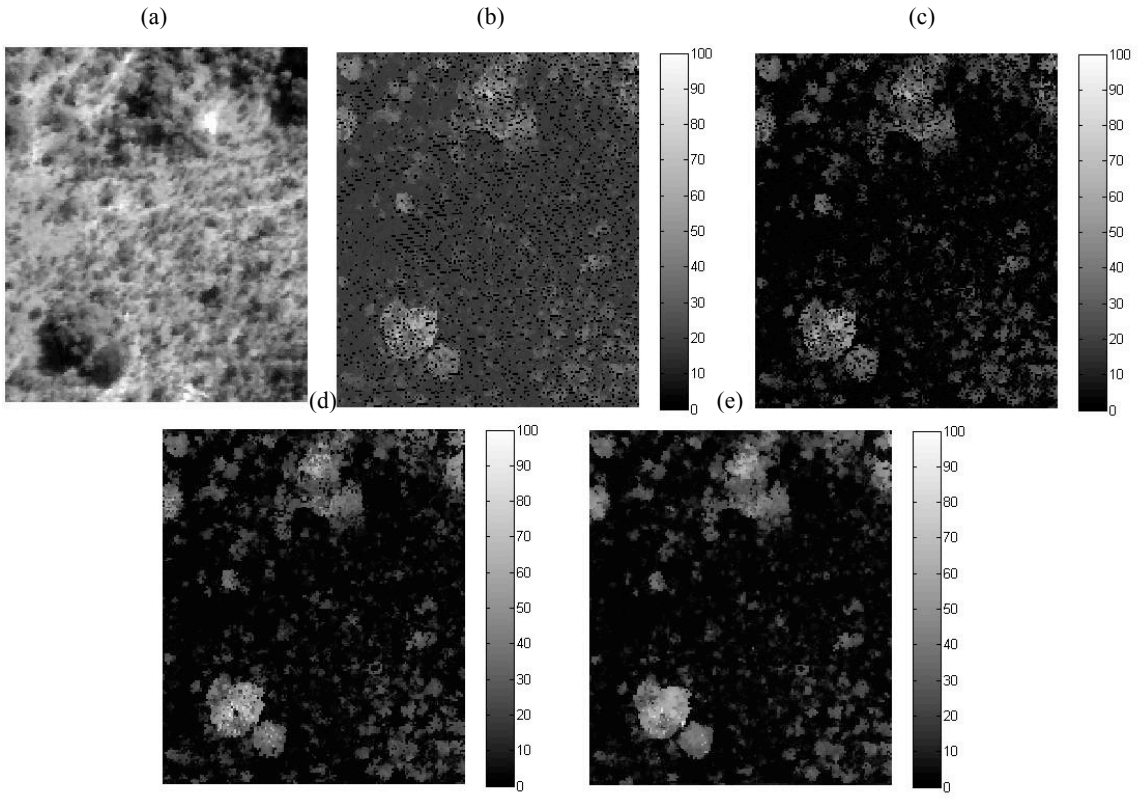

Figure 2.29. An example of a waveform LiDAR metric used for woody biomass modeling and the impact of processing steps: a panchromatic image of a site within the study area (a), 10-90% duration metric (b), after threshold removal and de-noising (c), deconvolution (d), ground registration and angular rectification (e).

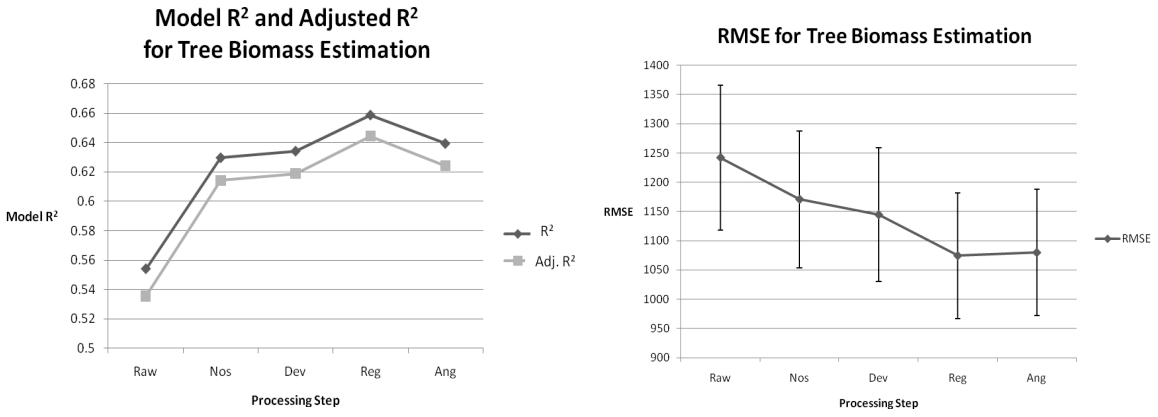

(a) (b)

Figure 2.30. Model R^2 as a function of the waveform processing steps (a). There is a slight decrease at the end of the chain, attributed to interpolation of neighboring waveforms. Model RMSE as a function of waveform processing step (b).

.

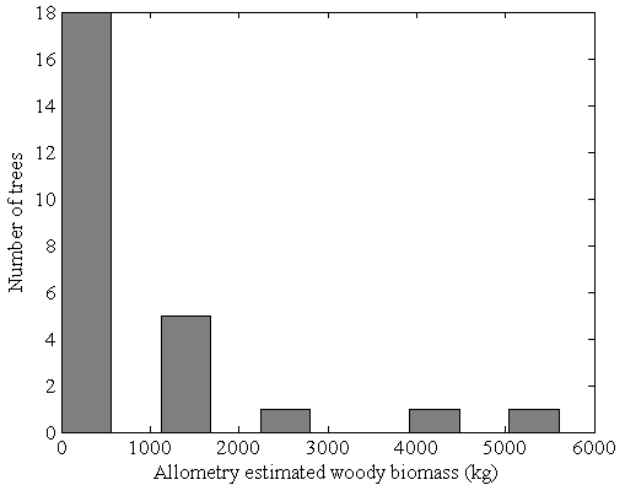

Figure 2.31. The distribution of allometry-estimated (field-based) woody biomass (kg) for the individual trees used in this study.

2.3 Conclusions

The question of deconvolution algorithm choice, as a preprocessing step to waveform LiDAR usage, has remained largely unanswered in literature. Previous attempts evaluated deconvolution approaches visually, without injecting quantitative assessments into studies [18, 24, 26, 30]. We have successfully developed a methodology based on four statistic-based quantitative metrics, namely, classification accuracy, RMSE, sensitivity, and false discovery rate, to compare three widely used deconvolution algorithms: RL, WF, and NNLS. This was done by taking advantage of high-fidelity waveform LiDAR simulations as our validation data. The results showed superior performance for the RL algorithm in terms of the small RMSE between the deconvolved and truth waveforms and a low false discovery rate for the recovery of the true 3-D tree cross section as one use case, and high classification accuracy for differentiating the herbaceous biomass levels as the second validation case. These results provide a quantifiable basis for the selection of the RL deconvolution approach in the waveform LiDAR preprocessing chain. We have also demonstrated the potential of waveform LiDAR particularly for vegetation applications in terms of savanna woody and herbaceous biomass estimation. A PCA-based algorithm has been developed to extract

features from the waveforms and relate these to herbaceous biomass levels. This could potentially provide a more efficient remote sensing based vegetation biomass assessment approach, particularly at senescent growth stages, when compared with traditionally expensive and time-consuming field data collection.

This chapter has also shown that the width of the outgoing waveform pulse has a major impact on waveform processing in that it directly affects the deconvolution results and our ability to extract fine scale structural vegetation features. This could benefit LiDAR users and system engineers in terms of optimizing the system configuration for their specific application.

Finally, we successfully developed and validated an end-to-end signal preprocessing chain to calibrate raw waveform LiDAR data, which typically exhibit a stretched, misaligned, and relatively featureless character when unprocessed. These artifacts are due to the outgoing pulse width, system response, and the off-nadir waveform acquisition capability. Such uncalibrated waveforms present obvious limitations to the application of waveform LiDAR and have a negative impact on the quantification of vegetation structure, biomass estimation, and other object structural characteristics. Our approach addresses these signal impairment problems by applying a preprocessing chain, which includes frequency-based noise filtering, Richardson-Lucy deconvolution, waveform registration, and angular rectification. We validated the impact of this method by taking advantage of a high fidelity, simulation environment with known waveform LiDAR system parameters and object (target) structure in the Digital Imaging and Remote Sensing Image Generation (DIRSIG) model. This approach enabled a direct comparison between the processed waveform signal and the true cross section profile of vegetation components. We used the spectral angle mapper (SAM) approach to quantify the stepwise improvement of waveform signal recovery after applying the preprocessing chain. The distinct decrease in spectral angles between truth and processed data along the preprocessing chain validated the performance of the methodology. We corroborated these findings by applying our preprocessing chain to real waveform LiDAR data collected by the Carnegie Airborne Observatory and extracting waveform metrics for modeling of tree-level woody biomass in a savanna environment. The significant improvement in model fit (R^2) and reduction in model root-mean-squared

error (RMSE) along the preprocessing chain corroborated our conclusion that the developed preprocessing approach has significant potential for improving the accuracy of waveform LiDAR-based vegetation biomass assessment. We believe that this approach will have a positive impact on other waveform LiDAR-based applications as well, since our preprocessing chain was developed for a general case. Future research should include efforts to further improve the functionality of this preprocessing chain by incorporating waveform normalization algorithms to calibrate the signal for intensity attenuation along the laser trajectory through vegetation. 3-D Voronoi natural neighbors interpolation can also be included for improved angular rectification, although this comes with an increased burden on computational and time resources. We are confident that this approach will have a significant impact on future small-footprint waveform LiDAR research, given its proven robustness in both a simulation and real environment and resultant high fidelity waveform signals.

Chapter 3: Waveform feature metrics extraction for biomass modeling

The application of LiDAR remote sensing technology to forest assessment has become an effective approach to facilitate in-field measurement and vegetation characterization. However, monitoring the biomass change at the tree-level by using small-footprint waveform LiDAR has seldom been reported in literature. In addition to that, the study of the correlation between the herbaceous biomass and small footprint waveform LiDAR also has not been addressed. In this chapter, we describe the approach of waveform feature metric extraction for both woody and herbaceous biomass modeling. The waveform LiDAR data (pixel size: 0.56×0.56m, vertical resolution: 1ns) for this study was acquired by Carnegie Airborne Observatory (CAO; http://cao.ciw.edu) during April 2008. Each scene pixel consists of an incoming (received) waveform data with 256 bands and 1ns (0.15m) spacing. The waveform of the outgoing pulse, associated with each incoming waveform (40 bands with 1 ns spacing), was also provided. Please see Section 2.1.1.1 for a detailed data description. The ground height above sea level for each pixel was extracted from a digital elevation model (DEM), which was derived from coincident discrete return LiDAR data, following the extraction of bare earth (ground) returns using Terrasolid software (V. 008.001).

Outputs from this chapter have been published as follows:

- Wu J., J.A.N. van Aardt, G. P. Asner, R. Mathieu, T. Kennedy-Bowdoin, D. Knapp, K. Wessels, B.F.N. Erasmus, and I. Smit, 2009. Connecting the dots between laser waveforms and herbaceous biomass for assessment of land degradation using small-footprint waveform lidar data. *Proceedings of IEEE International Geoscience & Remote Sensing Symposium*, vol. II, pp. 334-337, Cape Town, South Africa, 2009 [48].
- Wu J., J.A.N. van Aardt, G.P. Asner, T. Kennedy-Bowdoin, D. Knapp, B.F.N. Erasmus, R. Mathieu, K. Wessels, and I.P.J. Smit, 2009. LiDAR waveform-based woody and foliar biomass estimation in savanna environments. Peer-reviewed proceedings: *Silvilaser 2009 - 9th International Conference on Lidar Applications for Assessing Forest Ecosystems*, October 14-16, 2009, College Station, TX [60].

3.1 Methods

This chapter employed the same real waveform dataset and field data as Chapter 2; we therefore refer the reader to Section 2.1.1.1 for more details.

3.1.1 Metrics for woody biomass modeling

Figure 3.1 illustrates the proposed approach of waveform metric extraction at tree level. After processing via the aforementioned preprocessing chain (Chapter 2), we selected all the waveforms with more than one peak, since waveforms typically exhibit multiple peaks due to tree canopy, sub-canopy, and ground interactions. The first metric, d_1, is defined as the distance from the full-width-half-maximum (FWHM) of the first peak to the last peak, which we propose corresponds to the height of the tree. The second metric, d_2, is extracted as the distance between the first valley and FWHM of the first peak, since this value should reflect the thickness of crown within that footprint (0.56m).

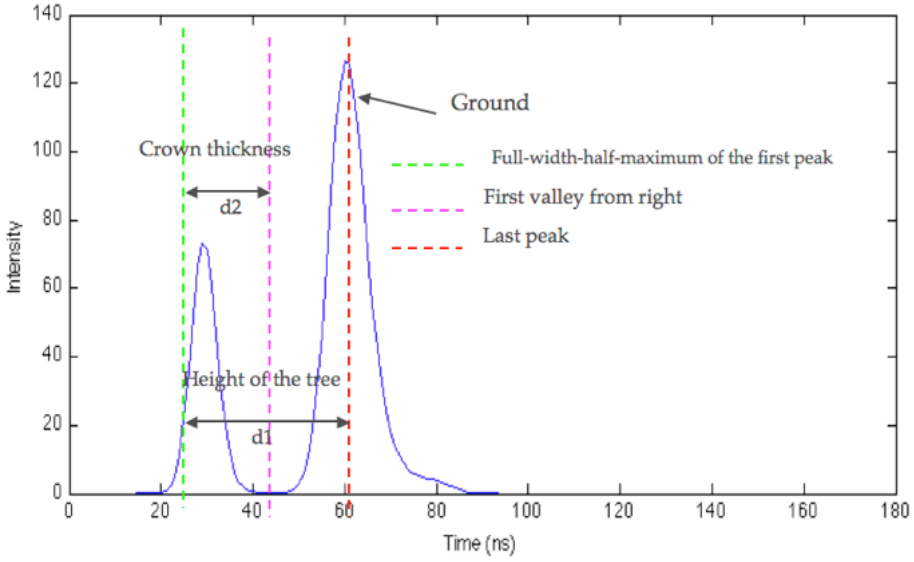

Figure 3.1. A graphical representation of the metrics extracted from each LiDAR waveform

It is evident that any given tree will be represented by a number of waveforms at 0.56m spatial resolution. The final estimation of tree height was thus determined by

scanning the pixel in z-slice (Figure 3.2) from top to bottom until its intensity equaled the FWHM of the first peak of the corresponding waveform; tree height was then assigned as d_1 of that waveform.

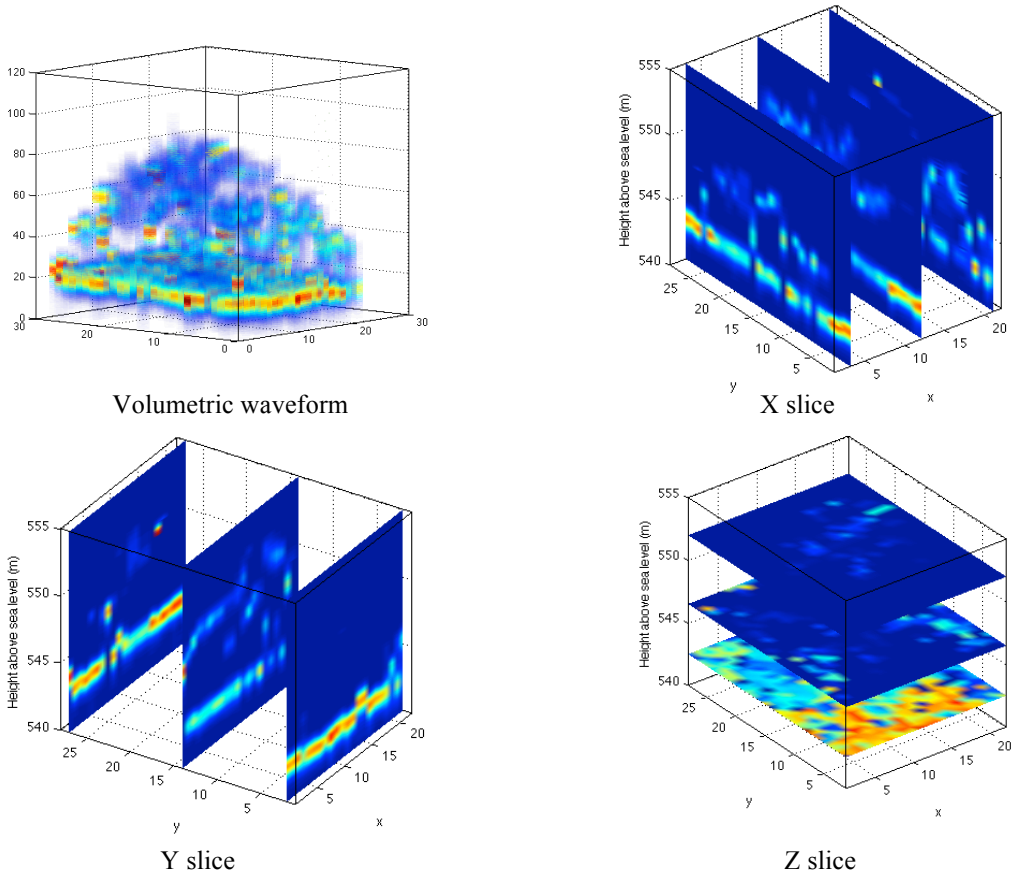

Figure 3.2. 3D volumetric waveform visualization at the individual tree level. The presentations show x,y,z coordinates, with waveform intensity color-coded from cool (blue; low) to warm (red; high)

In addition to that, we also used the standard statistical approach to estimate the mean and standard deviation for crown thickness by:

$$\bar{d}_2 = \frac{\sum_N d_{2,i}}{N} \tag{28}$$

$$d_{2,std} = \sqrt{\frac{\sum_{N}(d_{2,i} - \bar{d}_2)^2}{N}} \tag{29}$$

The crown volume of the tree can also be approximated by $S\sum_{N} d_{2,i}$, where S is the pixel size (0.56m× 0.56m), d_2, is extracted as the distance between the first valley and FWHM of the first peak, i denotes the pixel index for the pixel within the crown footprint, and N is the total number of pixels associated with crown, which can be determined by computing the peak number for each pixel in that tree plot. For example, a waveform with a single peak typically represents a ground-only interaction, while multiple peaks suggest the existence of a tree or tree crowns of different tree overlapping within that footprint. Figure 3.3 shows a histogram representation of the crown thickness estimation from an individual tree. A red cross indicates the GPS location of the tree for linking the waveforms to the field data and the rectangular plot area was manually extracted from the gray-scale DEM image. The mean and standard deviation of the crown thickness are determined by the shape of the crown itself, thereby offering a metric with which to characterize the tree in terms of species, foliar biomass, crown shape, etc.

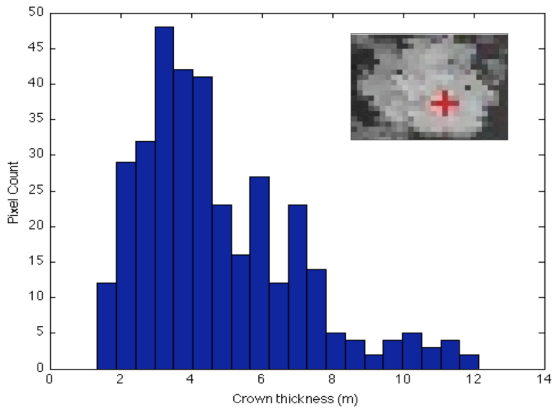

Figure 3.3. An example of a histogram showing the crown thickness distribution, derived from multiple LiDAR waveforms (0.56 m), for an individual tree canopy.

3.1.2 Metrics for herbaceous biomass modeling

We have already described a statistics-based approach to extract an uncorrelated feature metric that can differentiate herbaceous biomass using the predefined simulated waveform data in Section 2.1.3.2. However, we observed that the shape of real waveform LiDAR data from grass is much more complicated due to the mixture of factors such as substrate, stone, multiple scattering of the photons, uneven ground surface, etc. Waveforms associated with similar herbaceous biomass levels could result in distinctly different distortion levels. Thus, we proposed to model the herbaceous biomass using a Gaussian decomposition approach, hypothesizing that the herbaceous biomass, directly associated with the grass abundance, can be linked to the properties of the last waveform component (Figure 3.4).

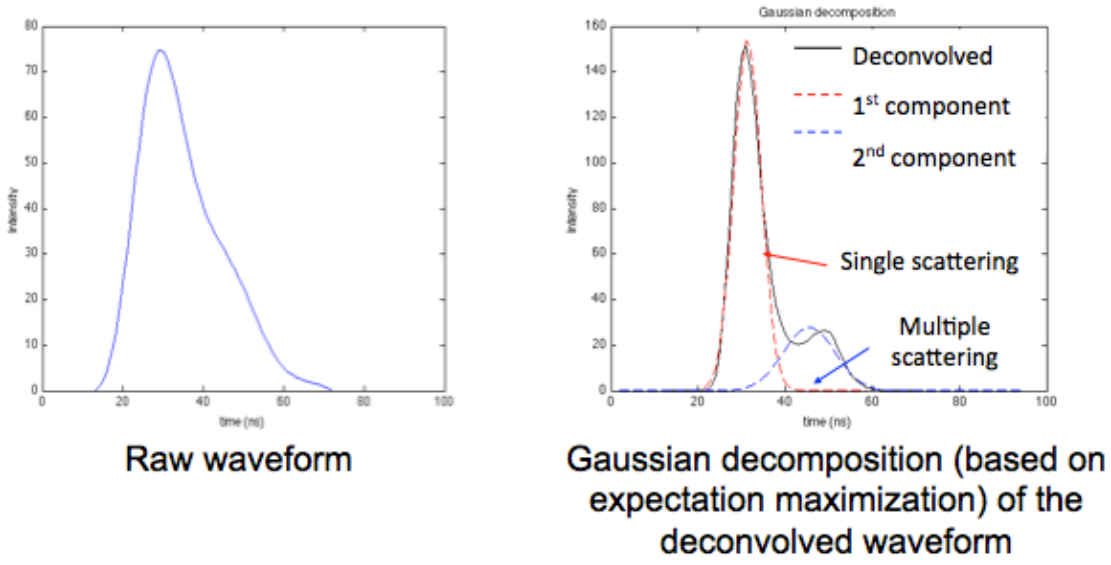

(a) (b)

Figure 3.4. Modeling the herbaceous biomass by Gaussian decomposition; it was hypothesized that the complexity of the herbaceous layer is correlated to the multiple scattering component

The last component of a waveform LiDAR return typically corresponds to the ground-level response, which may be composed of bare soil, grass, leaves, stones, etc. We hypothesized that the herbaceous biomass, directly associated with the grass abundance, can be linked to the properties of the last waveform component, specifically the width, height, and area properties of this component. Figure 3.4 (a) shows the raw return waveform (single peak), where there is no tree or shrub present. Figure 3.4 (b) reveals a dual-peak intensity distribution after deconvolution of the raw waveform; this was hidden in the raw signal due to an imperfect system response and variable outgoing pulse. An expectation-maximization (EM) algorithm was subsequently employed to decompose this deconvolved waveform into two individual Gaussian curves [36]. It is evident that the second Gaussian is mainly due to the asymmetric trailing edge, relative to the leading edge in the raw waveform. This asymmetric trailing edge hypothetically results from the late return photons due to the structure of the ground layer, such as grass, leading to multiple scattering of the return signal. On the other hand, the first Gaussian was seen as corresponding mainly to the single scattering from the ground material, e.g. bare soil, grass, stone, etc. The mathematical description of this waveform as a mixed Gaussian model is expressed as:

$$g(x) = a_1 e^{-\frac{(x-u_1)^2}{2\sigma_1^2}} + a_2 e^{-\frac{(x-u_2)^2}{2\sigma_2^2}} \tag{30}$$

where a_1 and a_2 are the amplitudes of the Gaussian peaks and σ_1 and σ_2 are the standard deviation (related to width) of each Gaussian; x and μ_i are input and mean variables, respectively. The next step involved extraction of waveform metrics (independent variables) and linking these to the measured field biomass data. Since we have parameterized the waveform in terms of a Gaussian distribution, feature metrics, e.g., a_1, a_2, σ_1, and σ_2, can be directly extracted from Eq. 30. We also added two additional metrics, namely s_1 and s_2, which correspond to the integral (area) of the two Gaussian curves. These six independent metrics are not necessarily uncorrelated, which led to the exclusion of highly-correlated (> 0.8) metrics after calculation of correlation coefficients. The herbaceous biomass model was finally retrieved based on a linear regression fit between the selected, independent feature metrics and field data in the form of:

$$H_{biomass} = \sum_{1}^{n} c_n p_n + k \tag{31}$$

where p_n refers to the n^{th} feature metric, c_n represents the associated coefficient, and k is the residual.

3.2 Results and discussion

a. Woody biomass

A correlation coefficient matrix (Table 3.1) was created for the field data and waveform-derived metrics in order to optimize the metric selection. Three important aspects are evident from Table 3.1. First, it was observed that the measured height exhibited a high correlation with the estimated height. Second, measured foliar biomass is highly correlated with the estimated crown volume. Third, measured woody biomass can be estimated by crown volume and the standard deviation of crown thickness, since the crown volume showed a correlation of less than 0.8 with the standard deviation of the crown thickness. Avoidance of highly correlated independent variables typically increases model robustness [61]. All the metrics in Table 3.1 have been converted into "natural log" space in order to minimize the nonlinearity between the parameters.

TABLE 3.1
CORRELATION COEFFICIENTS BETWEEN FIELD DATA (BLUE) AND WAVEFORM-DERIVED METRICS (YELLOW) (D=DIAMETER MEASURED ABOVE BASAL SWELLING; H=MEASURED HEIGHT)

	D	H	Woody biomass	Foliar biomass	Estimated height	Crown volume	Mean (crown)	Std (crown)
D	1	0.8167	0.9806	0.984	0.796	0.8498	0.8436	0.6706
H	0.8167	1	0.7767	0.7832	0.9247	0.8182	0.8569	0.714
Woody biomass	0.9806	0.7767	1	0.961	0.7776	0.8393	0.8466	0.6582
Foliar biomass	0.984	0.7832	0.961	1	0.788	0.8553	0.8452	0.6889
Estimated height	0.796	0.9247	0.7776	0.788	1	0.8614	0.9342	0.7936
Crown volume	0.8498	0.8182	0.8393	0.8553	0.8614	1	0.8608	0.7373
Mean (crown)	0.8436	0.8569	0.8466	0.8452	0.9342	0.8608	1	0.8963
Std (crown)	0.6706	0.714	0.6582	0.6889	0.7936	0.7373	0.8963	1

The estimation of foliar biomass was best performed using the crown volume metric, based on the observations from the correlation table, while woody biomass modeling relied on both crown volume and standard deviation of crown thickness as independent variables. The mathematical regression model can be expressed as:

$$\ln(FB) = 0.7888 \ln(V_{waveform}) - 1.7088 \quad (32)$$

$$\ln(WB) = 1.39 \ln(V_{waveform}) + 0.36 \ln(S_{waveform}) - 1.94 \quad (33)$$

where FB indicates the foliar biomass, V is the crown volume, WB represents the woody biomass, and S is the standard deviation of the crown thickness. The coefficients were solved by least squares linear regression. Figure 3.5 shows the plots of estimated height and woody and foliar biomass vs. field-measured values, with R^2 values of 0.92, 0.73, and 0.71 for height, foliar biomass, and woody biomass, respectively. Overall, the results suggest that waveform-derived metrics have significant potential for assessing tree structure and biomass of savanna species.

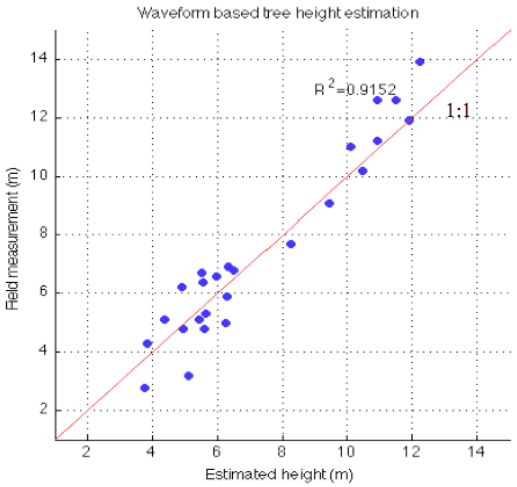

(a)

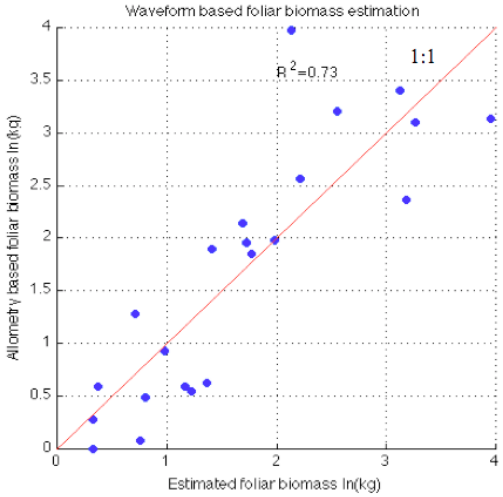

(b)

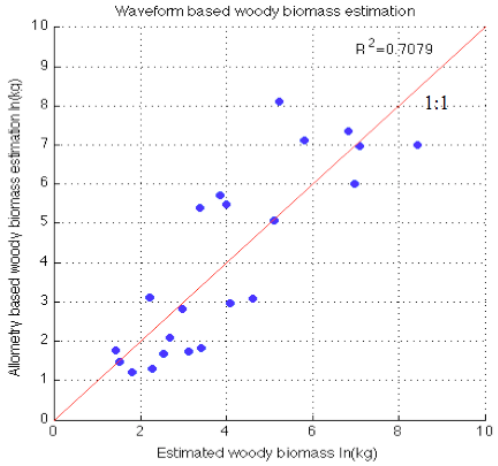

(c)

Figure 3.5. (a) Height, (b) foliar biomass, and (c) woody biomass estimation using waveform LiDAR metrics.

b. Herbaceous biomass

The proposed herbaceous estimation model (Eq. 30, 31) was tested for 6 different sites, in which herbaceous biomass ranges between 0-90 gram/plot ($0.25m^2$ samples; 216 plots in total). We only considered waveforms (before deconvolution) with a single peak, i.e., waveforms that did not exhibit multiple peaks due to tree canopy returns. This reduced the number of sample plots to 159. We also assumed that the GPS locations of the pixel-based (0.56x0.56m) waveform and the plot center (field sample) were both representative of the same plot. Herbaceous biomass samples were then grouped into 5g classes for the purposes of this study, which led to 18 weight-based biomass classes (e.g. 0-5, 5-10,…, 85-90) in the 0-90g range. Waveform-derived metrics and measured biomass were averaged within each class.

Table 3.2 shows the correlation coefficient matrix for the field data and waveform-derived metrics, used to optimize the variable selection. All the metrics in Table 3.2 have been converted into "natural log" space to minimize the nonlinearity between the parameters. It is evident that pairs (a_1, s_1) and (a_2, s_2) exhibited high correlations. We therefore discarded a_1 and s_2 to ensure model robustness, since these correlated metrics also exhibited a lower correlation to the biomass, when compared with s_1 and a_2, respectively.

Figure 3.6 shows the results of herbaceous biomass estimation using feature metrics σ_1, s_1, a_2, and σ_2 (Eq. 34), where the coefficients were solved by least squares linear regression. We concluded that the waveform approach has potential for estimating above-ground herbaceous biomass, given the model's ability to explain almost 60% (R^2=0.59) of herbaceous biomass variability. However, we also hold that the small range in herbaceous biomass field values, limited structural information, and senescent state of the vegetation were detrimental to model performance.

$$\ln(HB) = 6.3 \ln(a_1) + 5.2 \ln(s_1) + 0.3 \ln(a_2) + 0.4 \ln(\sigma_2) - 41.6 \quad (34)$$

where HB represents the herbaceous biomass. a_1 and a_2 are the amplitudes of the Gaussian peaks, σ_2 is the standard deviation (related to width) of each Gaussian, and s_1 corresponds to the integral (area) of the first Gaussian curve.

TABLE 3.2
CORRELATION COEFFICIENTS BETWEEN FIELD DATA AND WAVEFORM-DERIVED FEATURE METRICS FOR HERBACEOUS BIOMASS ESTIMATION

	a_1	σ_1	s_1	a_2	σ_2	s_2	***Bio (H)***
a_1	1	-0.12	0.98	0.79	0.35	0.59	0.69
σ_1	-0.12	1	0.07	0	-0.05	-0.09	0.21
s_1	0.98	0.07	1	0.80	0.36	0.58	0.75
a_2	0.79	0	0.80	1	0.52	0.93	0.67
σ_2	0.35	-0.05	0.36	0.52	1	0.57	0.35
s_2	0.59	-0.09	0.58	0.93	0.57	1	0.50
Bio (H)	0.69	0.21	0.75	0.67	0.35	0.50	1

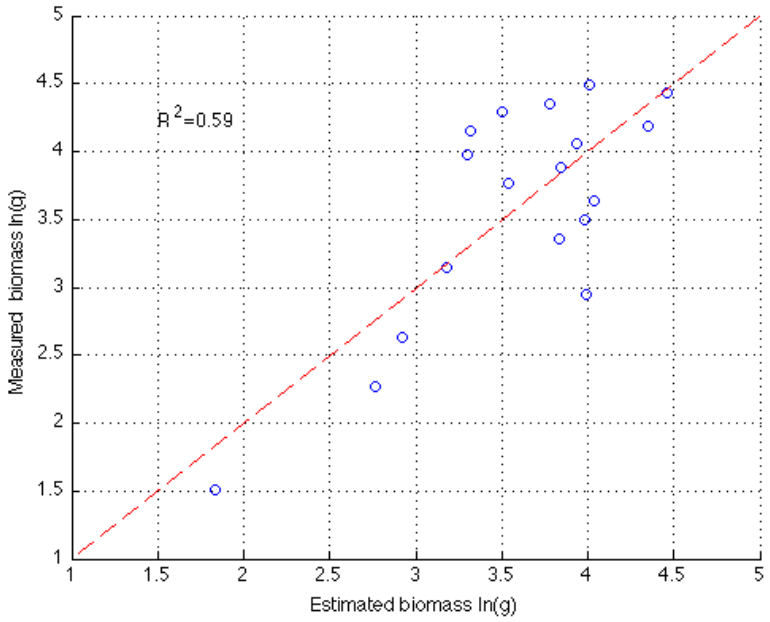

Figure 3.6. Herbaceous biomass estimation using waveform LiDAR-derived metrics.

3.3 Conclusions

We successfully extracted structural metrics from LiDAR waveforms and related these to woody and foliar biomass measurements from a savanna region. The results show that waveform LiDAR technology has significant potential for estimating woody and foliar biomass at the tree-level, or fine scales, in this savanna environment. Although we did not evaluate the performance of more traditional discrete return LiDAR, it was evident that the waveform approach was especially useful for foliar biomass estimation. This parameter evidently corresponds to the tree crown volume, which can be effectively measured using waveform LiDAR. We concluded that waveform LiDAR has a unique advantage over discrete return LiDAR in this case, since the latter typically records the response from the canopy and subsequent lower-level returns at a per-determined minimum distance based on the sensor's reset time (see Asner et al., 2009) [62]. Waveform LiDAR, on the other hand, contains intensity data at a higher temporal/vertical resolution; these data points can be effectively associated with crown thickness or volume. We therefore propose to use more detailed, accurate, and precise ground-truth field data, in the form of 3D models, to better relate LiDAR waveforms to vegetation structural characteristics. Additionally, the current research can be extended from individual tree to plot-, site-, and landscape level for land degradation assessment in future efforts.

In addition to the woody and foliar biomass modeling, we also extracted waveform LiDAR feature metrics from the deconvolved waveform's Gaussian responses to model plot-level herbaceous biomass - the coefficient of determination (R^2) indicated that our model could explain 60% of the variation in herbaceous biomass. Although this could be considered as relatively low, it still implies that a significant portion of the herbaceous biomass variability can be characterized by a single wavelength remote sensing modality; it therefore is clear that significant potential exists for assessment of herbaceous biomass in savanna ecosystems at fine scales using waveform LiDAR. We attributed the relatively poor model performance to a narrow range of field biomass values. Future research should focus on biomass estimation during the wet season, linking woody-herbaceous

biomass assessment, and applying spectral-based mixture mapping to further explore the relative variation of LiDAR returns across different vegetation species, structures, biomass, etc., at the sub-pixel level.

Chapter 4: 3D tree reconstruction using waveform LiDAR data

As was pointed out in the introduction, most of the current reported methods for 3D tree structure reconstruction are based on high density discrete return or point cloud datasets from ground-based LiDAR systems, i.e., a sequence of x, y, z coordinate combinations. A direct inverse modeling approach, based on full-waveform LiDAR data, still presents a gap in terms of LiDAR research. This is especially true since such ground-based LiDAR systems can only acquire data from a small area of vegetation for 3D reconstruction purposes, which is not useful for ecosystem monitoring, such as land degradation analysis and its associated requirement of a large area sample. Also, most of the existing reconstruction approaches are primarily focused on branch and stem reconstruction and the challenge of 3D leaf-on tree reconstruction has not been addressed adequately. In this chapter, we propose to use the method of 3D clustering using "DBSCAN" (density-based spatial clustering of applications with noise) to achieve 1st order waveform based 3D tree inverse reconstruction. Note that by "1st order" we imply first order branching, i.e., the tree stem and its immediate branching pattern from that stem. First, the algorithm of "DBSCAN" will be described, followed by a presentation of the results of 3D branch reconstruction for both leaf-off and leaf-on conditions.

In terms of validation of the 3D reconstruction approach, it is evident that complete knowledge of the target, or tree object in this case, is required. We used the Digital Imaging and Remote Sensing Image Generation (DIRSIG) simulation environment and hypothesize that this approach can eventually be extended to actual airborne data, since our 3D reconstruction algorithms will be based on known and accurate 3D models that served as reference for reconstructed trees. This effectively negates the challenge related to our lack of complete vegetation target knowledge, a situation that is typical of studies based on natural resource field data alone.

4.1 Methods

For the methodology development and validation, we used the same dataset, based on simulated waveforms of six different tree species, as described in Section 2.1.3.1. We also added the 4ns outgoing pulse width waveform simulation to evaluate the pulse width impact on the 3D branch reconstruction, similar to Chapter 2, where the 4ns pulse width was added based on reviewer feedback for the published preprocessing paper. The reader is referred to these sections for a detailed data description.

4.1.1 Waveform LiDAR clustering

The motivation for the 3D reconstruction of the tree branches using waveform LiDAR is similar to the concept of using high density point clouds data from discrete return data. Our approach is founded in the hypothesis that point clouds that are associated with the same object (branches, canopy, etc.) should cluster together if this object is visually separable from others in 3D space. Figure 4.1 shows an example of the point cloud visualization, extracted from simulated waveform LiDAR data for tree branches. We can clearly see the correlation between the point cluster and actual branch location.

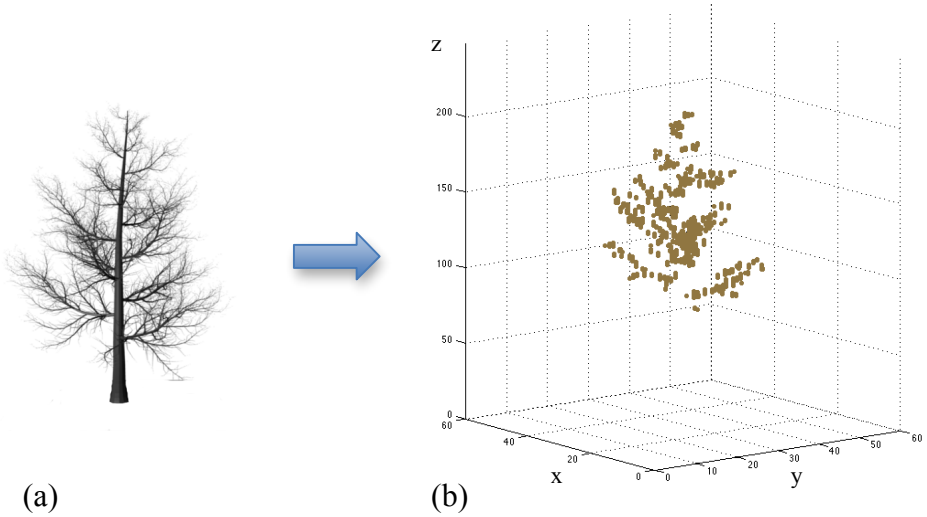

Figure 4.1. (a) 3D tree branches input and associated point clouds extracted from simulated waveform data (b)

Numerous clustering algorithms have been reported in the literature for image processing, data mining, and other purposes. The most famous, namely the k-means clustering algorithm [63], requires knowledge of the number of clusters to classify the data using an iterative strategy to optimize the objective function. The result is the location of the center of gravity of each cluster. The shape of the cluster is therefore restricted to be a symmetric ellipse or circle, which is rare for the point clouds that are related to the branch structure in 3D space. The improved k-medoid method, CLARANS (Clustering Large Applications based on RANdomized Search) [64] was shown to be more efficient, while the "natural" number of clusters also can be determined by this algorithm. However, the run time of this approach is significantly larger making it unsuitable for processing large scale LiDAR data. Other methods, such as the hierarchical algorithm [65], iteratively split the data into smaller subsets. The advantage is that it does not require "*k*" (the number of clusters) as an input. However, the main problem is the difficulty of determining the termination condition to indicate when the merge or division process should be terminated.

In DBSCAN (density-based spatial clustering of applications with noise) proposed by Ester *et al*. (1996) [66], a cluster, which is a subset of the total points, must meet the following two properties:

1. All the points within that cluster should be mutually connected in terms of density.
2. If a point is density-wise connected to any point in the cluster, this point is a part of that cluster as well.

The algorithm starts with any arbitrary point in the database. The only variables that need to be defined by the user are (i) the minimum number of points required to form a cluster (MinPts) and (ii) the radius of the neighborhood (eps). For each point that has not been visited, its neighborhood is retrieved and if there are enough points contained in that neighborhood, a cluster is initiated, otherwise, it is labeled as noise point. Please see A.2 for the pseudo code [67].

The underlying principle of DBSCAN is that for each point of a cluster, its neighborhood should contain at least a minimum number of points or a certain point density. To detect a cluster, DBSCAN can start with any arbitrary point in the database,

and retrieve all associated points, based on a density parameter. The reasons that DBSCAN was chosen for tree branch reconstruction in this study are as follows: First, it does not require the number of clusters as *a priori* input (in contrast to the k-means algorithm); Second, the spatial shape of the branch cluster can be arbitrary, as shown in Figure 4.2, which allows flexibility in the branch posture.

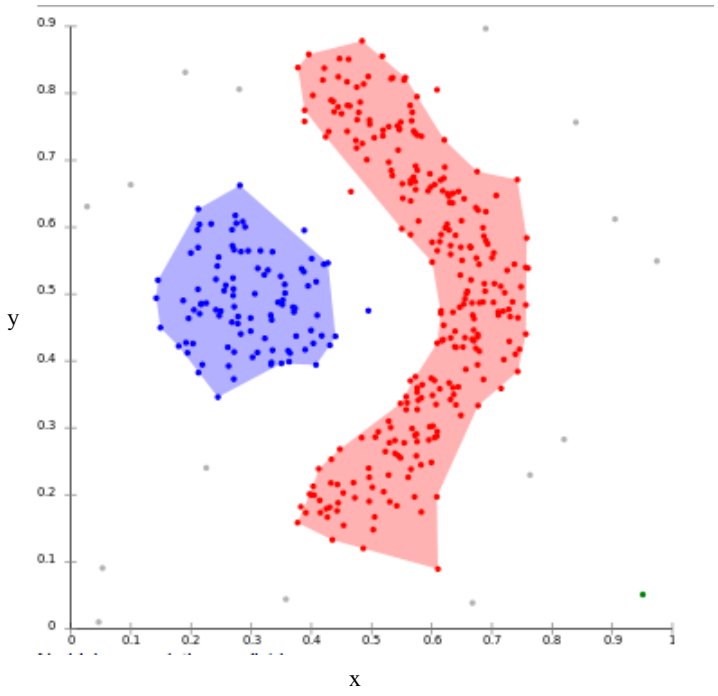

Figure 4.2. An illustration of the DBSCAN algorithm that shows the arbitrary nature of cluster shapes [68]

4.1.2 Stem and branches reconstruction

The stem can be modeled as a cone structure, where height can be defined as the distance from the ground response to the highest location of the point clouds, derived from each waveform data sample. The stem center position on the x, y plane can be estimated based on the average of x, y for all the point clouds. This is based on the assumption that for regular trees, the main stem is typically located in the center of the branches.

For the reconstruction of branches, an assumption was made that each cluster can be approximated by a cylinder to represent a branch. The two apexes of the branch are defined as the closest and furthest point within that cluster relative to the stem center. The main challenge in reconstructing a complete 3D tree in leaf-on condition using waveform LiDAR data, is indeed the branch component. This is due to the fact that the laser pulse in the near-infrared wavelength (1064 nm) typically is not transmitted by branches inside the canopy. Therefore, the voxelized waveform points associated with a tree typically show the profile of the canopy only, without internal branch and stem structures

It is recognized that, although some of the LiDAR waveform energy may originate from the branch reflection or backscatter, it will remain challenging to retrieve the exact 3D location of the each branch. This is due to the complex geometry of the branch orientation, branch-leaf mixtures, and the limitation of the waveform LiDAR temporal (vertical) resolution (0.15 m for CAO system). However, we still can estimate the approximate location of branches of a tree for at least the 1st order level - branches from the main tree bole - by looking at the canopy profile. This assumption is based on the hypothesis that leaves can only propagate from branches. In order to maximize the number of branches that can be detected, the same approaches that were applied for the leaf-off condition, can be used for leaf-on condition as well. The DBSCAN algorithm was run using different waveform intensity threshold settings, until the maximum number of clusters was reached.

However, these reconstructed 1st order branches may also disconnect from the main stem because of the strong energy attenuation in those woody areas. Two parameters therefore were proposed to address this challenge, namely branch length (L) and branch angle (Θ), to first select the 1st order branches and then naturally reconnect them to the stem. Figure 4.3 shows the top view of the initial sparse branch locations using cylinders, one of which is highlighted in red and labeled by "L" and "Θ". Here, L is the length for that cluster, while Θ is defined as the angle between the two apexes of that branch relative to the stem center:

$$L = |V_0 - V_1| \tag{35}$$

$$\theta = acos\left(\frac{V_0 \cdot V_1}{|V_0||V_1|} \right) \tag{36}$$

where V_0 and V_1 are the vectors representing the two apexes of the branch.

The hypothesis is that the cluster size (length) of the first order branch should be relatively long compared to the sub-order branches. The projection angle, Θ, between the two apexes should also be small enough so that this branch can directly originate from the center stem. The threshold of L and Θ can be defined by the user, since this value can vary for different tree species, and is also dependent on the waveform LiDAR settings, e.g., LiDAR wavelength, power, etc.

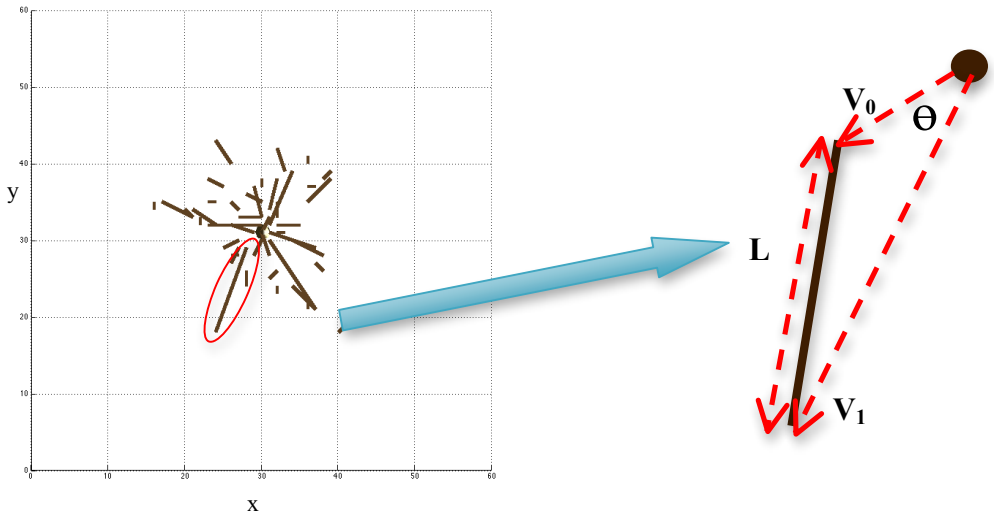

Figure 4.3. 1st order branch characteristics in terms of L and Θ

Once the first order branches were removed, the next step was to reconnect them to the stem. Figure 4.4 shows the side view of the first order branches, and the dashed line is where the branch is extended to the stem. In order to maintain the same tilt angle for the branch, it can be modeled using similar triangle geometry. The position that the branch originates from can be estimated by:

$$Z_x = \frac{\beta Z_1 - Z_0}{\beta - 1} \tag{37}$$

$$\beta = \sqrt{\frac{X_0^2 + Y_0^2}{X_1^2 + Y_1^2}} \tag{38}$$

where, (X_1, Y_1, Z_1) and (X_0, Y_0, Z_0) spatial coordinates of the two apexes for that branch.

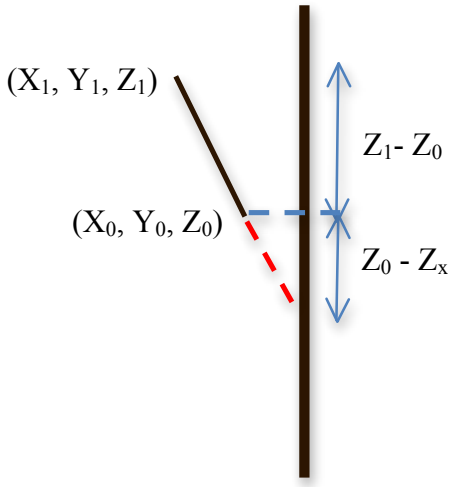

Figure. 4.4. An example of how a first order branch can be reconnected to the stem

Finally, the sub-branches can be connected to the nearest neighboring branches for better visualization. To further quantify the accuracy of the branch reconstruction, three metrics were computed to compare the reconstructed branch under leaf-on condition to the leaf-off condition: average azimuth angle (*AA*), average zenith/tilt angle (*TA*), and average projected branch length (BL). The azimuth angle is in the 0 ~ 360º range, and the zenith or the tilt angle of the branch is defined to be 0 ~ 90º, assuming that the branches only grow upwards (Figure 4.5). The projected branch length is defined to be the projection length of the branches onto the x, y horizontal plane (Figure. 4.3). However, we considered that it will be difficult to resolve every branch at centimeter level, similar to what is typically attempted in the case of high point density ground-based LiDAR scanners, due to the limitation of the spatial resolution of the airborne waveform LiDAR. This will likely be true even at a small footprint size, e.g., 0.5m in x,y plane and 0.15m in the vertical direction. We binned the azimuth angle into four regions, namely (0-90°),

(90-180°), (180-270°), and (270-360°). Then all the three metrics were averaged in each region for comparison.

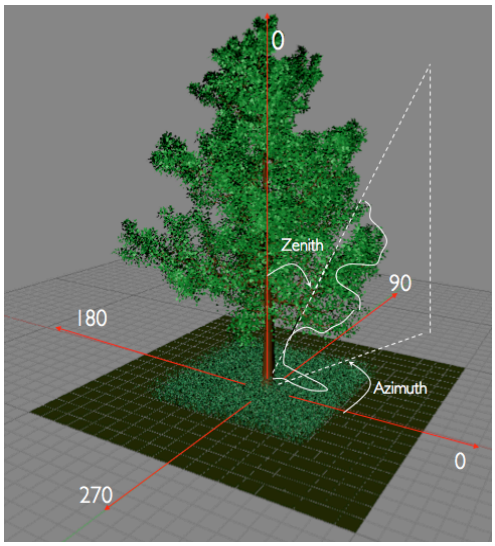

Figure. 4.5. Definition of tree azimuth and zenith angle

4.2 Results and discussion

4.2.1 Leaf-off scenario

First, we consider a simple case, namely the reconstruction of a branch using the simulated waveform from a 3D tree model at the leaf-off condition. In reality, the typical outgoing pulse has a specific pulse width; therefore, when the laser pulse interacts with the target (branch), the width of reflected waveform will be increased further due to the convolution of the outgoing waveform with the target profile. This may cause difficulty in representing the object if we register every sampling point in the waveform and plot them in 3D space. In contrast with the discrete return LiDAR points - where only first return points are used to represent the target at that location - waveform data use many

continuous sampling points to indicate one location, which effectively amounts to usage of redundant data. Obviously, we can set a threshold for the waveform intensity to reduce the data redundancy, since typically only the waveform peak region corresponds to the most critical location of the target. Figure 4.6 shows a 3D representation of waveform data with different intensity thresholds by taking tree #3 as an example, where every point is extracted from the waveform sampling and has an intensity beyond the threshold. It is evident that, if the threshold is set too high, an inadequate number of points will result in an inability to represent the branch structure. On the other hand, too small a threshold can result in data redundancy, which could make it challenging to distinguish the exact branch location. Therefore, the threshold setting is critical to ensure acceptable clustering results.

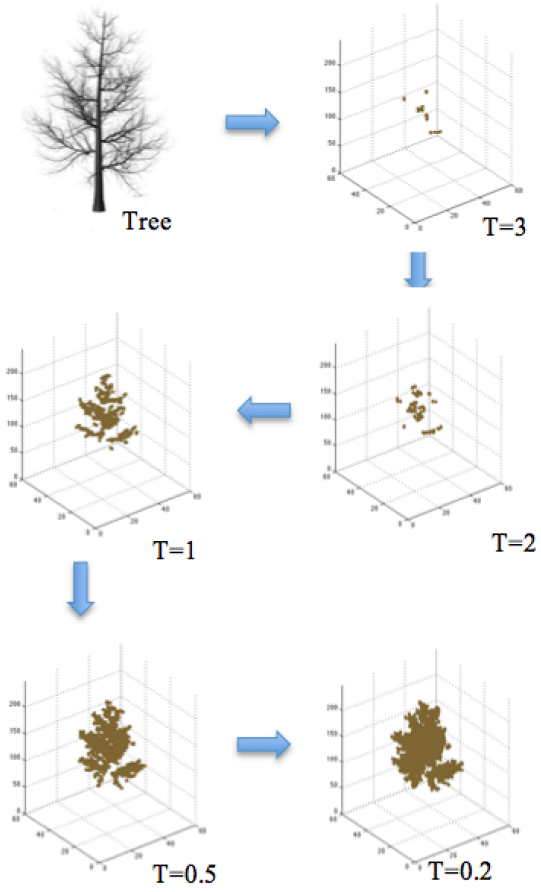

Figure 4.6. Branch representation using waveform LiDAR data with different intensity thresholds. e.g., all the point clouds intensity are larger >3 while T=3 (this was done based on tree #2)

As we proposed in the Section 4.1.2, in order to maximize the detection of branches, we iteratively run the DBSCAN with different waveform intensity threshold setting until the maximum number of clusters was reached. Figure 4.7 shows the plot of number of cluster versus intensity threshold. We conclude the maximum number of clusters is considered optimal, since too few points will result in fewer clusters, whereas too many points located close together (e.g. the whole tree), may be grouped into a single cluster. The point where branches are clearly distinguishable will yield the most clusters. The results of Figure 4.7 corroborates the observation made in Figure 4.6, i.e., that there exists an optimal threshold that can return the maximum number of clusters. In this example, the optimal threshold associated with the maximum number of clusters is 1.21, which resulted in 49 clusters. The final cluster result based on this optimal threshold is also illustrated in Figure 4.8. Different color points was used to represent the cluster that has been identified. In contrast to the large-scale discrete return LiDAR point clouds associated with the first returns, which is more sparse and does not necessarily form a branch shape in 3D space, waveform data provide more flexibility to maximize the possibility of detecting the branches.

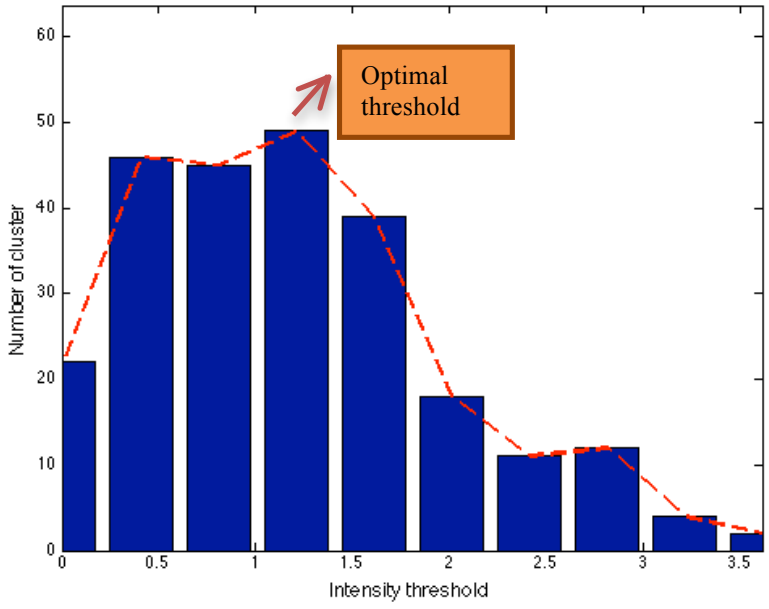

Figure 4.7. A graphical representation of the optimal threshold for clustering

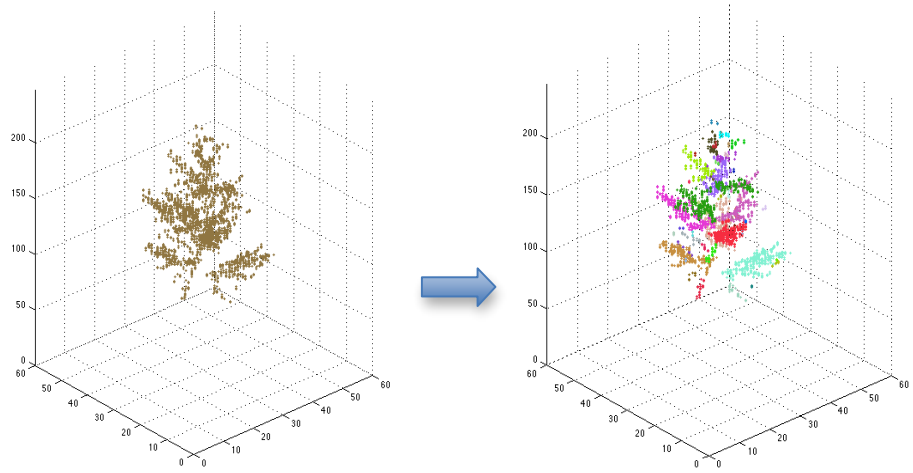

Figure 4.8. Results of DBSCAN clustering based on the optimal threshold; different clusters are distinguished by color

Once the data subset was chosen according to the threshold, the stem was modeled as a cone structure, centered at the average of x,y for all the point clouds. Results are presented in Figure 4.9.

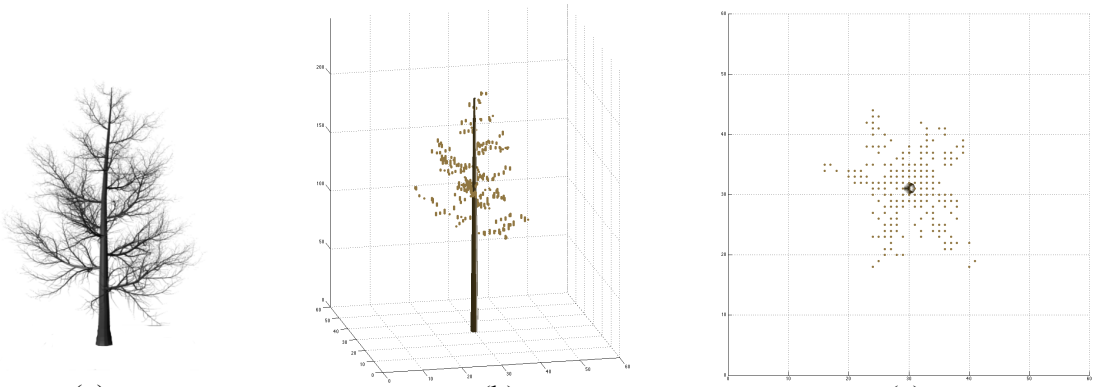

Figure 4.9. Stem reconstruction for leaf-off case: (a) Leaf-off tree input, (b) reconstructed stem from a side view, and (c) reconstructed stem from a top view

Figure 4.10 illustrates 1st order branches approximated by cylinders from each cluster, using DBSCAN, for a tree model in leaf-off condition. The two apexes of the branch are defined as the closest and furthest point within that cluster, relative to the stem center. Finally, we reconnected the branches to the stem, using Equation (37), to make it more realistic, as shown in Figure 4.11.

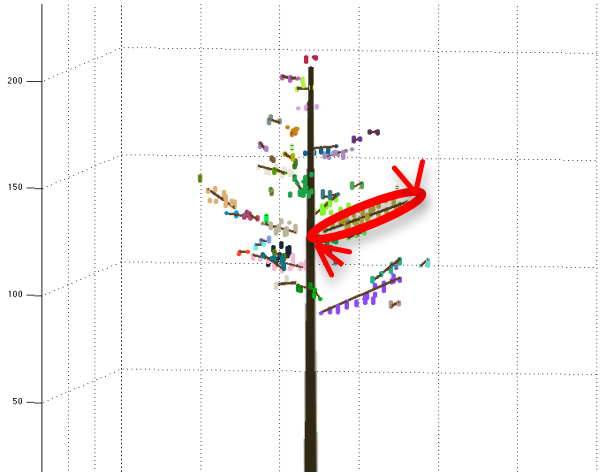

Figure 4.10. 1st order branches approximated by cylinders from clusters for a tree model in leaf-off scenario.

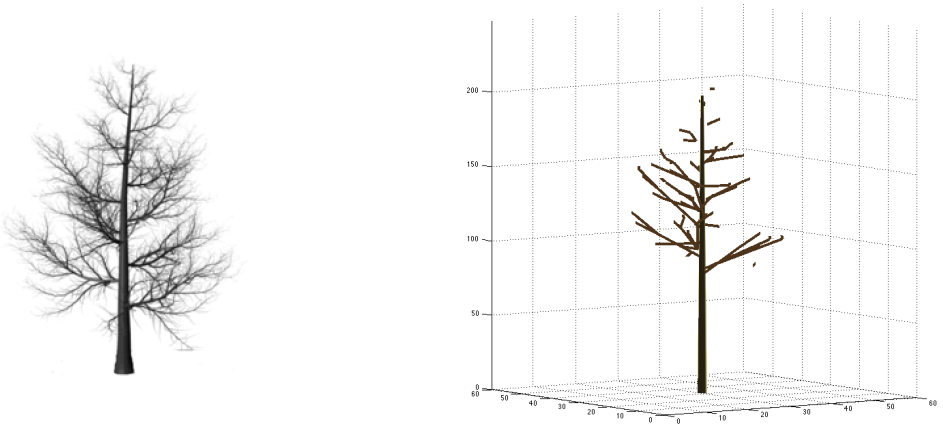

(a) (b)

Figure 4.11. (a) Leaf-off tree input. (b) Final reconstruction result of the branches for the leaf-off scenario

4.2.2 Leaf-on scenario

Following the same methodology as we applied for the leaf-off scenario, the results for leaf-on case, based on the same tree #2, is presented in this section. Figure 4.12 shows the difference between the point clouds without any filtering vs. the application of the optimal intensity threshold. The effectiveness of this threshold is evident from Figure 4.12 (b), where the internal branch cluster is much more defined. Figure 4.13 shows the stem reconstruction for leaf-on case. The overall canopy shape can already be visualized at this point.

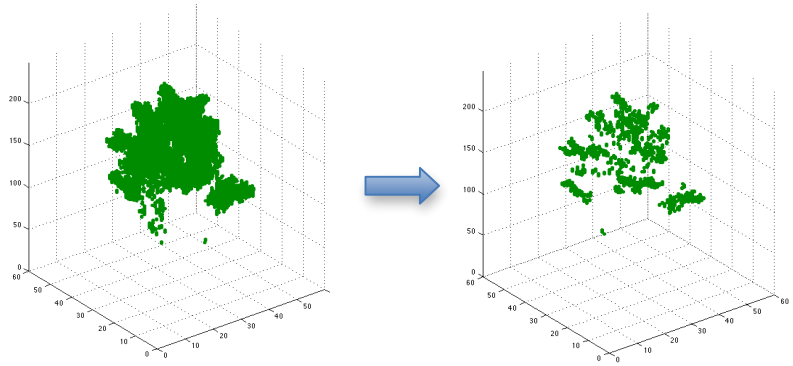

(a) (b)

Figure 4.12. (a) Raw point clouds extract from the waveform, (b) after applying optimal intensity threshold.

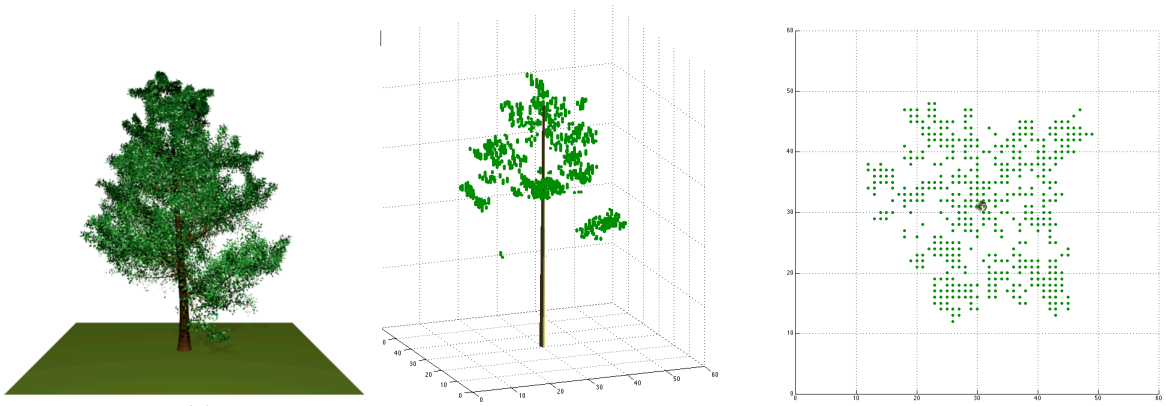

(a) (b) (c)

Figure 4.13. Stem reconstruction for leaf-on condition: (a) Leaf-on tree input, (b) reconstructed stem from a side view, (c) reconstructed stem from a top view

Figure 4.14 shows the results of optimal DBSCAN clustering, as well as the branch representation of each cluster. Compared to the leaf-off condition (same tree in Figure 4.10), it was observed that the branch structure is similar in terms of location and tilt angle. However, for the leaf-on scenario, the branches look more sparse; this was attributed to the rapid energy attenuation while the laser pulse passes through the canopy.

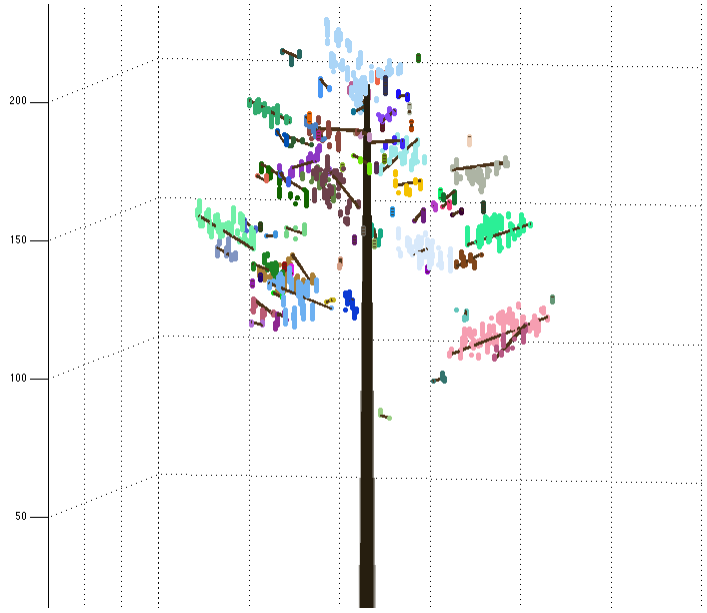

Figure 4.14. 1st order branches, as approximated by cylinders from clusters for a tree model in the leaf-on scenario

Figure 4.15 shows the final results of the stem and branch reconstruction for leaf-on scenario. In general, the 1st order branch structure appears to be similar, which is promising, while the leaf-off condition results in more details when compared to the leaf-on condition. This is to be expected because the canopy cluster can overlap, resulting in fewer branches that can be detected. Also, on the other hand, energy attenuation as laser pulses pass through the canopy also reduces the chance of detecting the branch and leaf structure, especially in the bottom portion of the canopy.

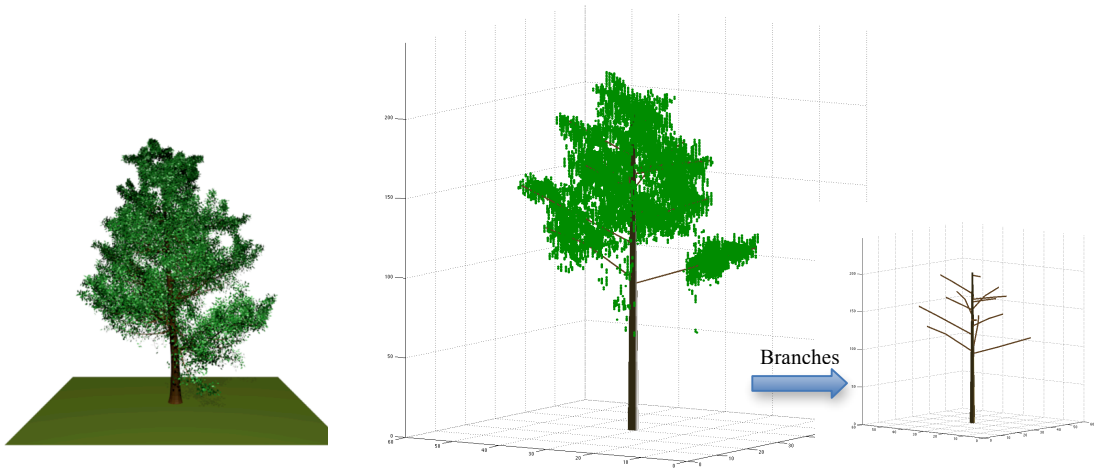

(a) (b)

Figure 4.15. (a) Leaf-on tree input. (b) Final reconstruction result of the branches for the leaf-on scenario

To further quantify the difference of branch reconstruction between the leaf-off and leaf-on case, Figure 4.16 shows the diagram that characterizes the branch azimuth angle vs. the 2D 1st order branch projection, and also the azimuth angle vs. the tilt angle (zenith) for each branch. Each vector in the diagram represents a branch projected in 2D xy plane at certain azimuth angle, and the length of the vector corresponds to the projected branch length and the tilt angle respectively. The results are summarized in Table 4.1. It can be observed that the azimuth angle and tilt angle of the reconstructed branches from the leaf-on tree are each only about 6° different from the leaf-off condition (truth data). The projected branch length was first normalized by the longest branch in the comparison, because the 1st order branch absolute length derived from the leaf-on condition is typically longer than that for the leaf-off state, due to the larger point cloud volume of the canopy. For the 3D reconstruction purpose, the relative distribution of branch position, and length is obviously more of interest to us. As the table shows approximately 7% branch length difference was observed based on these results.

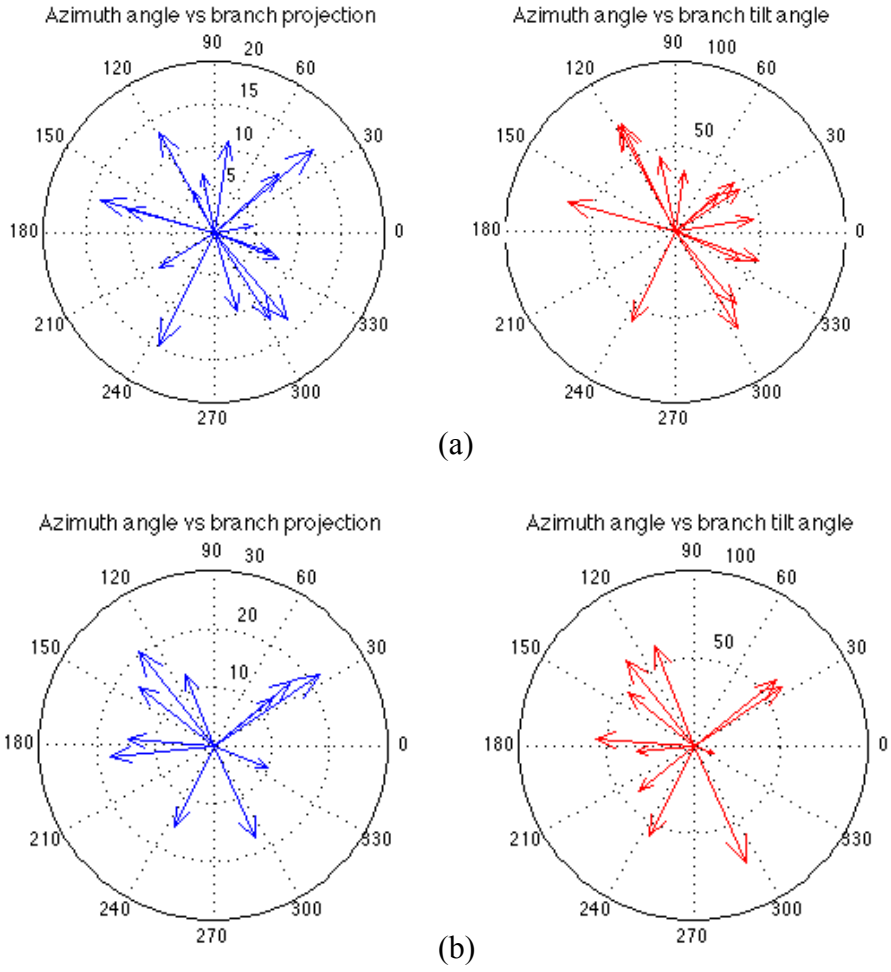

Figure 4.16. Branch reconstruction characterization for leaf-off (a) and leaf-on (b) scenario

TABLE 4.1
Quantitative comparison of the branch reconstruction for leaf-off and leaf-on conditions
Δ represents difference for each metric

	Azimuth Angle in degree (AA)		Title Angle in degree (TA)		Normalized Branch Length (BL)	
Region:	Leaf_on	Leaf_off	Leaf_on	Leaf_off	Leaf_on	Leaf_off
0-90	36.92	42.94	54.42	40.35	1.00	0.92
90-180	139.22	133.08	56.75	52.84	0.92	0.90
180-270	215.42	229.10	45.48	51.96	0.95	1.00
270-360	315.89	315.49	43.08	43.22	0.79	0.91
Average Δ	6.56		6.15		0.07	

	2ns	4ns
AA	18.72	13.01
TA	17.63	10.61
BL	0.05	0.11

	2ns	4ns
AA	15.06	13.30
TA	-7.39	-19.57
BL	0.07	0.01

	2ns	4ns
AA	-6.80	-12.20
TA	0.35	5.08
BL	0.07	0.05

	2ns	4ns
AA	8.19	12.79
TA	2.69	-15.78
BL	-0.01	-0.08

	2ns	4ns
AA	26.83	18.13
TA	17.74	8.02
BL	0.02	0.02

(a) (b) (c) (d)

Figure 4.17. Branch reconstruction results (a) original 3D tree model (leaf-on), (b) original 3D tree model (leaf-off), (c) reconstructed tree branches using waveform simulated from leaf-on tree, (d) quantitative results of 2ns and 4ns pulse width branch reconstruction (leaf-on) accuracy by comparing to the truth data (2ns leaf-off). Note: Azimuth Angle in degree (AA), Title Angle in degree (TA), Normalized Branch Length (BL)

The algorithm was further tested on five other trees from different species, using a 2ns outgoing pulse width for simulated waveforms for the leaf-off tree state as truth data. These truth data were then compared to the branch reconstruction results using simulated waveform LiDAR signals for the leaf-on tree states for 2ns and 4ns outgoing pulse widths. The latter pulse width was chosen to evaluate the pulse width impact on the 3D reconstruction, and also because a 4ns outgoing pulse width is commonly used in commercial waveform LiDAR systems.

The first column (a) of Figure 4.17 shows the input high-fidelity 3D tree models that were used for generating simulated waveform from DIRSIG, while the second column (b) shows the same trees in leaf-off condition. The reconstructed 3D tree branch structure, based on the simulated waveforms from trees in leaf-on state and using a 2ns outgoing pulse width is presented in the third column (c). The accuracy in terms of the difference (azimuth angle, tilt angle, and branch length) between the truth data is listed in the last column (d). As we can see, the presented approach can successfully reconstruct similar 1^{st} order branch structure to the truth data, even with the leaf-on condition by visual comparison. Although the 3D reconstruction approach still can not reach the accuracy of ground base LiDAR mainly due to the limitation of the spatial resolution of airborne LiDAR system, but the preliminary results still look encouraging and hint at the potential of using waveform LiDAR to estimate the woody biomass of vegetation by locating every 1^{st} order branch, even inside the canopy volume.

In this experiment, in order to test the robustness of our method, we have used different trees, with differences in terms of branch orientation, tilt angle, etc. Figure 4.17 shows that the accuracy of branch reconstruction varies between trees. This is because the waveform spatial resolution (0.15m for a 1ns sampling rate) is identical across all the trees, but the spatial distance between branches inside the canopy can be quite different between species. Those branches with many small tips may cluster together and present a challenge when it comes to distinguishing branches using a limited waveform temporal resolution. We also observed that a smaller pulse width may not always result in better outcomes, which can be attributed to the fact that the algorithm always attempts to maximize the number of detected clusters, which means that the smaller the outgoing pulse width, the larger the number of branch clusters that can be detected by the

algorithm. In other words, the smaller pulse width may result in lots of higher order branch that could impact the azimuth and tile angle calculation accuracy.

4.3 Conclusions

In this chapter, we presented a novel 3D 1st order branch reconstruction approach based on DBSCAN clustering that applies on the LiDAR waveform data directly. Firstly, an optimal waveform intensity threshold was determined by iteratively running the DBSCAN across wide range of threshold setting in order to maximize the branch clusters that can be detected. The results also show the flexibility of 3D object reconstruction by using waveform data, in contrast to the airborne discrete return LiDAR, where we may not have enough information for data preprocessing. Because small footprint discrete return LiDAR usually produces single or a few (e.g, <4) returns in meter level footprint size, this type of data can only resolve the overall canopy shape, and may not even be able to show the branch cluster shape [69-71]. Secondly, we characterized the branch geometry in terms of branch length (L) and branch angle (Θ), by approximating the 1st order branch cluster as a cylinder from the clusters. Mathematically, we also developed a model using similar triangle geometry to naturally reconnect 1st order branches to the stem. Thirdly, the proposed approach was applied on both leaf-off and leaf-on scenarios for 1st order tree branch reconstruction. This was validated by using the simulated waveform data from DIRSIG that takes the same tree in these two scenarios as inputs. To further quantify the accuracy of the branch reconstruction for leaf-on case, three metrics were computed to compare difference, average azimuth angle (AA), average zenith/tilt angle (TA), and average projected branch length (BL). Although there exists some variation between different tree species and pulse width conditions, the results still show a promising outcome whereby our proposed approach can reconstruct tree structure at the 1st order branch level with similar geometry, compared to the leaf-off scenarios for different trees.

In short, our approach shows the 1st order skeleton structure inside the canopy can be successfully characterized and reconstructed using waveform LiDAR data, which has not been adequately addressed in the literature before. Further research could involve the

higher order branch reconstruction by estimating the sub-clusters in 3D. Also, local waveform intensity threshold may also be valuable to distinguish more details of the branch structure. In addition to that, advanced computer graphic techniques could be another tool to render the reconstructed branch in 3D in a more realistic way. Finally, this approach will be eventually tested on real waveform data to reconstruct a real tree.

Chapter 5: Conclusions

The processing and application of small-footprint waveform LiDAR systems are topics that arguably have not received adequate attention in scientific literature. In this thesis a detailed literature review of waveform LiDAR was presented in terms of the basic system scheme, signal processing algorithms, and associated applications. Accordingly, three objectives were identified based on existing gaps in the current waveform LiDAR research: (1) Develop a robust, end-to-end waveform LiDAR processing chain approach; (2) Decode the waveform in terms of feature metrics extraction for woody and herbaceous biomass modeling; and (3) Develop a signal- and image processing-based waveform LiDAR inverse model for 3D tree structure characterization and reconstruction using Digital Imaging and Remote Sensing Image Generation (DIRSIG) waveform LiDAR simulation.

An end-to-end signal processing chain to preprocess raw waveform LiDAR data - which typically exhibit a stretched, misaligned, and relatively featureless character when unprocessed - was developed and presented. Our approach addresses these signal impairment problems by applying a preprocessing chain, which includes frequency-based noise filtering, Richardson-Lucy (RL) deconvolution, waveform registration, and angular rectification.

The first challenge was that of identifying the best-suited deconvolution approach, as part of the preprocessing chain development. A methodology based on four statistic-based quantitative metrics, namely classification accuracy, RMSE, sensitivity, and false discovery rate was developed to compare three widely used deconvolution algorithms: RL, Wiener Filter (WF), and Non-negative Least Squares (NNLS). Such methods successfully solved the question of deconvolution algorithm choice as a preprocessing step to waveform LiDAR usage in the literature. The results showed superior performance for the RL algorithm in terms of the small RMSE between the deconvolved and truth waveforms, a low false discovery rate for the recovery of the true 3-D tree cross section as one use case, and a high classification accuracy for differentiating the herbaceous biomass levels as the second validation case. These results provide a

quantifiable basis for the selection of the RL deconvolution approach in the waveform LiDAR preprocessing chain.

The next step was to validate the entire preprocessing chain by using a high fidelity simulation environment in the DIRSIG model, which is based on known waveform LiDAR system parameters and object (target) structure. The approach enabled a direct comparison between the processed waveform signals and the true cross section profile of vegetation components. Spectral angle mapper (SAM) approach was used to quantify the stepwise improvement of waveform signal recovery after applying the preprocessing chain. The distinct decrease in spectral angles (e.g., 80º spectral angle before preprocessing, reduced to 20º after going through the entire preprocessing chain) between truth and processed data along the preprocessing chain, validated the promising performance of the methodology. The results also showed that the most significant improvement in the case of nadir waveforms occurs during the deconvolution step, while waveform registration has the biggest impact on spectral angles in the case of off–nadir waveforms. The preprocessing chain subsequently was applied to real waveform LiDAR data, collected by the Carnegie Airborne Observatory (CAO), and waveform metrics were extracted for modeling of tree-level woody biomass in a savanna environment. The significant improvement in model fit (R^2) - from 0.55 to 0.64 (or a 16% improvement) - and reduction in model root-mean-squared error (RMSE; from 1250kg/ha to 1080kg/ha; a 14% improvement) along the processing chain steps corroborated the conclusion that the proposed processing approach has significant improvement for the accuracy of waveform LiDAR-based vegetation biomass assessment.

Furthermore, algorithms for extracting the feature metrics required for woody, foliar and herbaceous biomass estimation were proposed; this approach highlighted the potential of small-footprint waveform LiDAR for this specific vegetation application. The model evaluation results exhibited a correlation of R^2 =0.92 for the tree height estimation, R^2 =0.73 for foliar biomass estimation, and R^2 =0.71 for the woody biomass estimation, based on our proposed model derived from small footprint waveform LiDAR dataset.

Finally, a clustering-based 3D tree reconstruction in terms of 1st order branch structure using waveform LiDAR data was also presented. This approach exhibited

flexibility in that it can be applied to both leaf-off and leaf-on conditions and produced encouraging results for both 3D branch visualization and quantitative metrics in terms of branch-level azimuth angle and tilt angle and length. To the best of our knowledge, this is also the first instance where individual tree-level branch reconstruction, based on airborne small-footprint waveform LiDAR data, was performed. This will contribute not only to the visualization of vegetation (trees) at a fine scale by using a large area coverage airborne LiDAR system, but also benefit the quantification of vegetation structure, biomass, etc. for natural resource applications.

Future research should include efforts to further improve the functionality of this processing chain by incorporating waveform normalization algorithms to calibrate the signal for intensity attenuation along the laser trajectory through vegetation. 3D Voronoi natural neighbor interpolation could also be included for improved angular rectification, although this comes with an increased burden on computational and time resources. Finally, a higher order branch reconstruction will constitute the logical next step for further improving the accuracy of the 3D branch reconstruction. As far as the waveform LiDAR system is concerned, auxiliary information, such as the signal-to-noise-ratio, will be useful to the application of the preprocessing chain towards optimization of the noise filtering level. The absolute energy data for both outgoing and incoming waveforms furthermore can be utilized to better understand and simulate the signal attenuation complexities, which theoretically could serve as the basis for eventual waveform normalization.

It was shown that this research presents a significant contribution to the science and application of small-footprint waveform LiDAR to structural assessment, given the proven robustness of the various approaches in both simulated and real environments. Finally, the processing code will be made available as an open source resource to the research community.

APPENDIX

A.1 DIRSIG waveform simulation model

DIRSIG, developed by the Digital Imaging and Remote Sensing (DIRS) Laboratory at Rochester Institute of Technology, was used to simulate the realistic interaction between the outgoing laser pulse and vegetation. The DIRSIG model [72-73] is designed to simulate returned fluxes for a scene as a function of time, using Monte-Carlo [74] ray tracing techniques and is based on outgoing laser pulses that are generated by a well-defined source system. The advantage of using a waveform LiDAR simulation approach is that we can arbitrarily change LiDAR system settings, e.g., pulse width, beam divergence (footprint size), wavelength, etc., thereby providing the flexibility to characterize the object structure for a variety of scenarios. On the other hand, the structural parameters of the virtual object, e.g., tree, grass, etc., are known exactly, thus enabling us to link tree height, crown shape, volume, biomass, leaf area, and other parameters to the simulated waveform.

Figure A.1 shows the workflow we used for waveform LiDAR simulation for a tree using DIRSIG. A 3D virtual deciduous tree was first created as input to the DIRSIG LiDAR simulation by using the tree generation software Arbaro [46]. Specific materials such as leaves, branches, and ground were mapped to each facet of this 3D model and valid emissivity and extinction coefficients, which are based on measurement of actual vegetation, were assigned to each material. This enabled the simulation of absorption, reflection, and transmission processes for each pulse and the vegetation it interacts with.

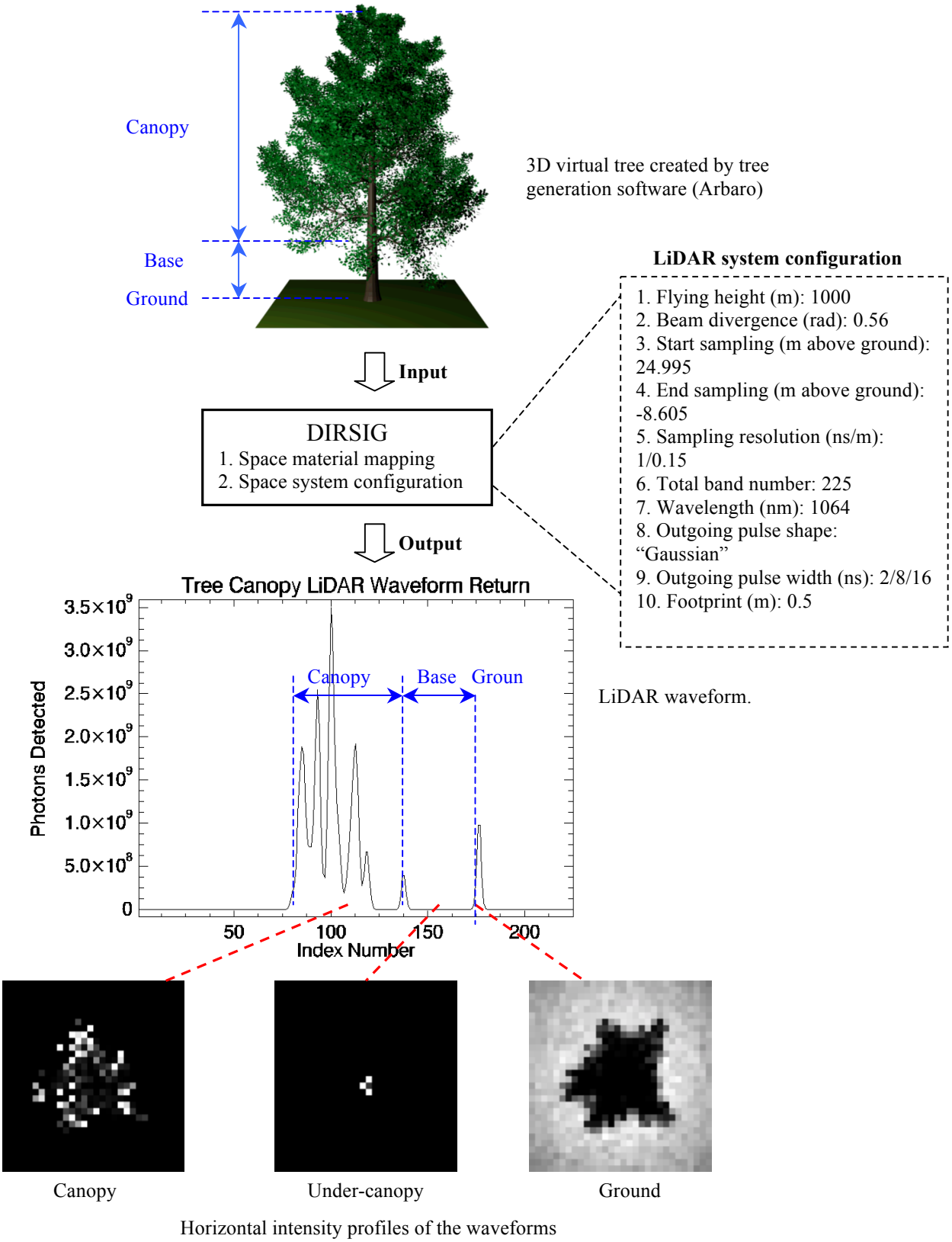

Figure A.1. Workflow of waveform LiDAR simulation using DIRSIG

An operationally viable waveform LiDAR platform was set up in the DIRSIG environment as per the system configuration lists: the goal was to match our virtual system with commercially available small-footprint waveform LiDAR systems, e.g., the Optech ALTM series. A varying outgoing pulse width (2/4/8/16 ns) was used in order to test the effect of pulse width on waveform processing and analysis results. The selection of pulse width was motivated by the outgoing pulse width of 16ns, as implemented in the operational waveform LiDAR system on the Carnegie Airborne Observatory [75], which is essentially a custom-built Optech ALTM 3100EA system. This operational selection is based on the need for the laser pulse to have enough energy to penetrate dense canopy in all woody or forested environments. A 2ns outgoing pulse width was used to generate the approximated or truth dataset. A 4ns (and 8ns) pulse width is the standard setting for the ALTM 3100 and other waveform LiDAR systems and was also used as an intermediate setting between 2ns and 16ns. Therefore, the outgoing pulse width setting of our simulation is congruent with an applicable operational system so that the results can guide the waveform preprocessing that will be applied to the real data. The transmitted pulses in operational sensors furthermore are asymmetric in shape, i.e., they have a slightly longer tail in the trailing edge vs. the leading edge. However, the shape of the outgoing pulse in the simulation was assumed to approximate a Gaussian distribution based on our observations of the actual outgoing pulse from the Carnegie Airborne Observatory (Figure A.2) and for the following reasons: Firstly, as can be observed from Figure A.2, the shape of the actual pulses closely approximates a “Gaussian” distribution and the observed asymmetry is minimal; secondly, the shape of the outgoing pulse in reality could vary in terms of the slope and intensity; we used a Gaussian approximation in order to maintain consistency in the shape of the outgoing pulse across all the waveforms for our simulation.

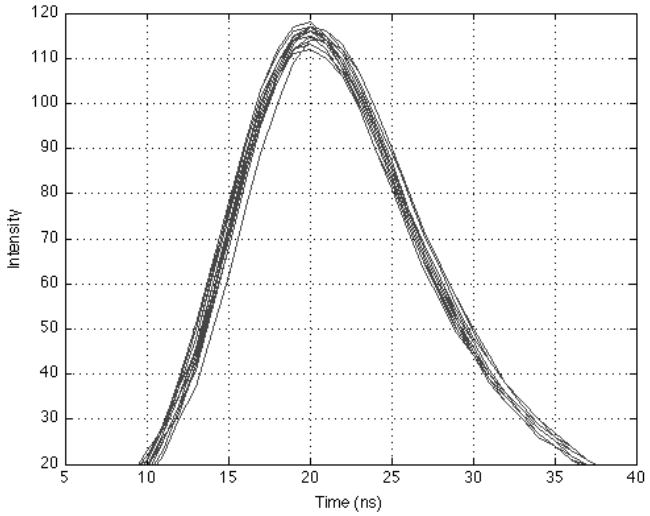

Figure A.2. Actual outgoing pulses used by CAO system (ALTM 3100EA)

Figure A.1 also shows an example of the typical output from the DIRSIG LiDAR simulation. The plot of the tree was divided into a 40x40 pixel grid with a footprint size equal to 0.5m, while the waveforms were sampled in 225 time bins for each pixel after implementing the simulation. The x-axis for each waveform corresponds to the time bins, which can be converted to height-above-ground. The y-axis of the output waveform represented the number of photons detected for that pixel at different heights or time bins, which directly relates to the intensity of the waveform signal in the real waveform LiDAR system. It can be observed that the waveform basically consists of three parts: the canopy (where most of the energy is reflected), the base of the tree (trunk without branches), and the ground response. In some situations, the ground response may not be recorded, since there is not enough energy transmitted by branches and leaves to reach the ground. A post-ground response, or delayed returns, may also be observed due to multiple scattering of photons and delayed signal travel time.

A.2 DBSCAN

Pseudo code is below:

```
DBSCAN(D, eps, MinPts)
   C = 0
   for each unvisited point P in dataset D
      mark P as visited
      NeighborPts = regionQuery(P, eps)
      if sizeof(NeighborPts) < MinPts
         mark P as NOISE
      else
         C = next cluster
         expandCluster(P, NeighborPts, C, eps, MinPts)

expandCluster(P, NeighborPts, C, eps, MinPts)
   add P to cluster C
   for each point P' in NeighborPts
      if P' is not visited
         mark P' as visited
         NeighborPts' = regionQuery(P', eps)
         if sizeof(NeighborPts') >= MinPts
            NeighborPts = NeighborPts joined with
NeighborPts'
      if P' is not yet member of any cluster
         add P' to cluster C

regionQuery(P, eps)
   return all points within P's eps-neighborhood
```

A.3 Waveform LiDAR processing GUI tools

Brief guideline for the waveform LiDAR processing tools

a). Start the tools:

1. Add the folder "GUI tools" to your MATLAB searching path.
2. Type "LiDAR_tools" to bring up the main user interface of the tools.

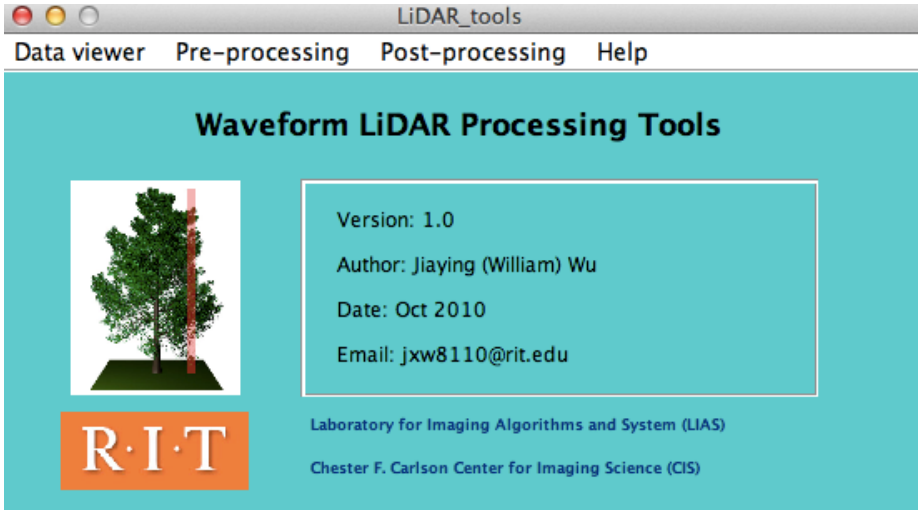

Figure A.3. LiDAR_tools main user interface

b). Data viewer:

1. Data viewer allows you to visualize three types of remote sensing data: spectra, discrete return (point clouds) and waveform data. (Spectra and waveform input data require the ENVI ".hdr" format, point clouds input data are ".txt" format)
2. **Note**: Please clear the cache whenever you reload the data or load new inputs to avoid any memory issues.

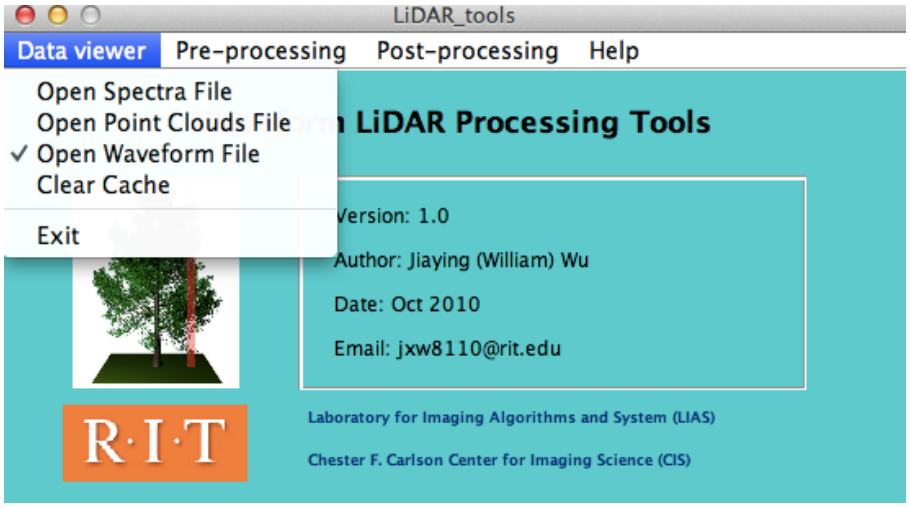

Figure A.4. LiDAR_tools data viewer

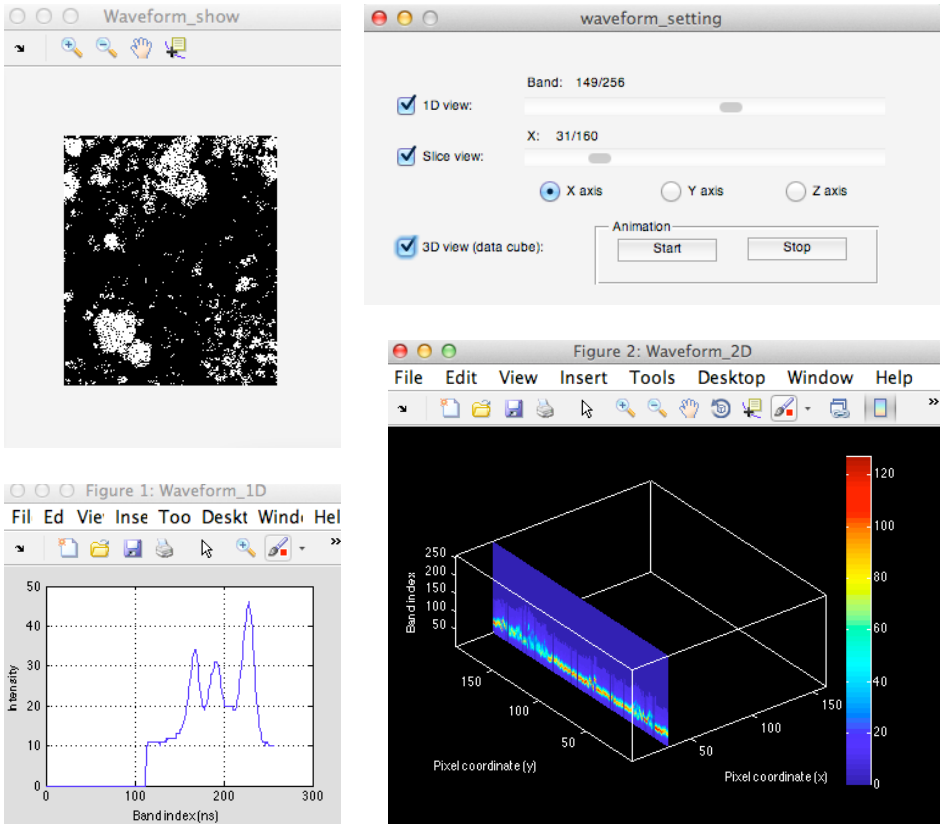

Figure A.5. Waveform LiDAR data viewer

c). Waveform preprocessing:

1. Select or unselect the required step (“Denoise”, “Deconvolution”, Registration”, “Angular Rectification”); then click “run” to launch the preprocessing-chain UI.
2. Depending on the steps you selected, only those required input areas in the preprocessing-chain UI will be activated.
3. Details about the preprocessing parameters can be found in my IEEE paper [42, 43].
4. The processed data can be exported as ENVI readable format.

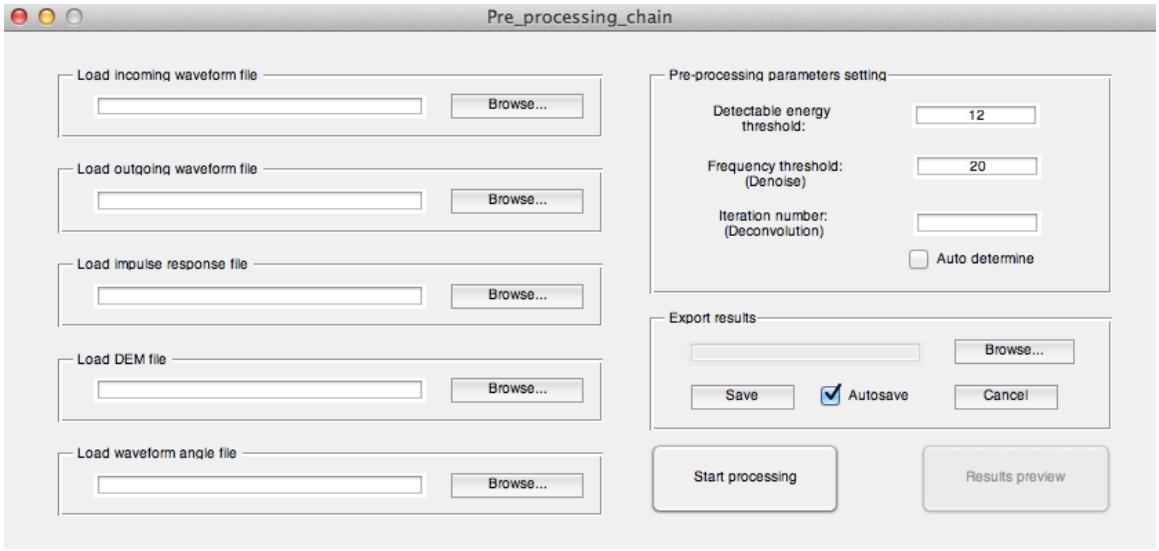

Figure A.6. LiDAR waveform preprocessing window

d). The overall code for the waveform processing chain is in “waveform processing.m”. This file is not included in the GUI tools, since it serves only as a tool for step-wise debugging and testing purposes (all the functionalities in the waveform processing.m was eventually dissected and used to make up the preprocessing section in the GUI).

A.4 Matlab source code

```
%% Smooth the waveform by removing the high frequency components
wf(wf<12)=12;
wf_f=fft(wf-12,[],3); %shift the data
wf_f_raw=wf_f;
wf_f(abs(wf_f)<20)=0; % filter the noise
wf=ifft(wf_f,[],3);
wf(wf<0.5)=0;

%%%%%%%%%%%%%%%%%%%%%%%%%%%%%%%%%%%%%%%%%%%%%%%%%%%%%%%%%%%%%%%%%%%%%%%%%%%%%%%

%% Waveform deconvolution (Richardson-Lucy)
% Intialization of parameters
iter=200;
residual=zeros(1,iter);
y_n=wf;
x_n=wf;
h_n=t0;
Imp_Res=reshape(Imp_Res,1,1,numel(Imp_Res));
Imp_Res=repmat(Imp_Res,[size(wf,1),size(wf,2),1]);
s_h=size(t0,3);
s_i=size(Imp_Res,3);
s_x=size(wf,3);
s_y=size(wf,3);

% compute the system contribution (convolve the impulse response with
% outgoing waveform)
h_n=ifft(fft(h_n,s_h+s_i,3).*fft(Imp_Res,s_h+s_i,3),[],3);
h_n=circshift(h_n,[0,0,-round(s_i/2)+1]);
h_n=h_n(:,:,1:s_h);
% Shift of the system contribution (peak at center)
h_n_temp=reshape(h_n,size(h_n,1)*size(h_n,2),size(h_n,3));
h_n_temp_left=repmat(h_n_temp(:,1),1,10);
h_n_temp_right=repmat(h_n_temp(:,end),1,10);
h_n_temp=[h_n_temp_left h_n_temp h_n_temp_right];
[C,I]=max(h_n_temp,[],2);
for ith=1:size(h_n_temp,1)
    h_n_temp(ith,:)=circshift(h_n_temp(ith,:),[0 30-I(ith)]);
end
h_n_temp=h_n_temp(:,11:50);
h_n=reshape(h_n_temp,size(t0,1),size(t0,2),size(t0,3))+eps;

% Iteratively deconvolove the incoming waveform
tic
for t=1:iter
    temp=ifft(fft(x_n,s_h+s_x,3).*fft(h_n,s_h+s_x,3),[],3);
    temp=circshift(temp,[0,0,-round(s_h/2)+1]);
    temp=y_n./(temp(:,:,1:s_x)+eps);
    temp=ifft(fft(temp,s_h+s_x,3).*fft(h_n,s_h+s_x,3),[],3);
    temp=circshift(temp,[0,0,-round(s_h/2)+1]);
    x_n=abs(x_n.*temp(:,:,1:s_x));
% Calculate the residual
    temp1=abs(ifft(fft(x_n,s_h+s_x,3).*fft(h_n,s_h+s_x,3),[],3));
    temp1=circshift(temp1,[0,0,-round(s_h/2)+1]);
```

```
    temp1=temp1(:,:,1:s_x);
    energy1=sum(wf,3);
    energy2=sum(temp1,3);
    energy2(isnan(energy2))=eps;
    scale=energy1./energy2;
    scale(isnan(scale))=eps;
    temp1=temp1.*(repmat(scale,[1 1 size(wf,3)]));
    temp2=sum((wf-temp1).^2,3);
    temp2(isnan(temp2))=eps;

residual(t)=(sum(sum(temp2))/(size(wf,3)*numel(find(sum(wf,3)>0))))^0.5
;
end
toc
wf_out=x_n;

%%%%%%%%%%%%%%%%%%%%%%%%%%%%%%%%%%%%%%%%%%%%%%%%%%%%%%%%%%%%%%%%%%%%%%%
%%%%%%%%%%%%%%%%%%%%%%%%%%%%%%%%%%%%%%%%%%%%%%%%%%%%%%%%%%%%%%%%%%%%%%%
%% Waveform Registration (from ground to top)
[x,y]=find(sum(wf,3));%find out the non-zero pixels
wf_temp=reshape(wf_out,size(wf,1)*size(wf,2),size(wf,3));
%transform the wf data from 3D to 2D
rows=find(mean(wf_temp,2));% Find nonzero rows
LUT=zeros(size(wf,1)*size(wf,2)*size(wf,3),4);
length=size(wf,3);
index=ones(size(x,1),1);
tic
for i=1:size(x,1)
    % Find the last peak of the nonzero waveform
    [b,a]=lmax(squeeze(wf_out(x(i),y(i),:)));
    if isempty(a)==0
    n=numel(a);
    % If the last peak is too small, we assume it's due to the multiple
    % Scattering and just ignore.
            while b(n)<0.15*max(b)
            n=n-1;
            end
    index(i,1)=a(n);
    % Assign the X Y Z and intensity to each waveform element
    % b1=0;
    b1=theta(x(i),y(i),1);
    b2=theta(x(i),y(i),2);
    b3=theta(x(i),y(i),3);
    % x (row)
    LUT(((rows(i)-1)*length+1):(rows(i)*length),1)=...
     x(i)+b3*sind(b1)*cosd(b2)/0.56+((1:length)'-
index(i,1))*sind(b1)*cosd(b2)*0.15/0.56;
    xp=round(x(i)+b3*sind(b1)*cosd(b2)/0.56);
    if xp<1
        xp=1;
    elseif xp>size(dem,1)
        xp=size(dem,1);
    end
    % y (col)
    LUT(((rows(i)-1)*length+1):(rows(i)*length),2)=...
     y(i)+b3*sind(b1)*sind(b2)/0.56+((1:length)'-
index(i,1))*sind(b1)*sind(b2)*0.15/0.56;
    yp=round(y(i)+b3*sind(b1)*sind(b2)/0.56);
```

```
      if yp<1
        yp=1;
      elseif yp>size(dem,2)
            yp=size(dem,2);
    end
    % z (height)
    LUT(((rows(i)-1)*length+1):(rows(i)*length),3)=...
    dem(xp,yp,2)-((1:length)'-index(i,1))*cosd(b1)*0.15;
    % Intensity
    LUT(((rows(i)-1)*length+1):(rows(i)*length),4)=...
     wf_temp(rows(i),:)';
    end
end
toc

%%%%%%%%%%%%%%%%%%%%%%%%%%%%%%%%%%%%%%%%%%%%%%%%%%%%%%%%%%%%%%%%%%%%%%%%%%%%%%%

%% Resampling to the 3D voxel (interpolation along xy plane)
ind=find(mean(LUT,2));
LUT1=LUT(ind,:);
L=size(dem,1);
W=size(dem,2);
[xi,yi]=meshgrid(1:L,1:W);
top=ceil(max(max(dem(:,:,1))));
bottom=floor(min(min(dem(:,:,2))));
h=bottom:0.15:top;
w=zeros(L,W,numel(h));
tic
for i=1:numel(h);
    Zslice=bottom+0.15*(i-1);
    index=find(LUT1(:,3)>Zslice & LUT1(:,3)<=Zslice+0.15);
    temp=LUT1(index,:);
    x1=temp(:,1);
    y1=temp(:,2);
    v1=temp(:,4);
    F=TriScatteredInterp(x1,y1,v1,'natural');
    w(:,:,i)=F(xi,yi)';
end
w(isnan(w))=eps;
toc




%%%%%%%%%%%%%%%%%%%%%%%%%%%%%%%%%%%%%%%%%%%%%%%%%%%%%%%%%%%%%%%%%%%%%%%%%%%%%%%

%% Tree 3D reconstruction
close all
wf1=enviread('tree4');
num=size(wf1,3);

threshold=3:0.5:5;

for j=1:numel(threshold)
```

```
A=wf1;
A(A<threshold(j)*10^9)=0; % threshold

X=[];
Y=[];
Z=[];

for layer=65:num
A(:,:,layer)=im2bw(A(:,:,layer),0); % Make the binary image
[row,col]=find(A(:,:,layer));
X=[X;col];
Y=[Y;row];
Z=[Z;layer*ones(numel(row),1)];
end

[IDX,type]=dbscan([X,Y,Z],2,2);

clust=max(IDX);
Cl(j)=clust;

end

figure
bar(threshold,Cl)
hold on
plot(threshold,Cl,'--r','LineWidth',2)
xlim([0 threshold(end)])
ylim([0 max(Cl)*1.3])
xlabel('Intensity threshold','fontsize',12)
ylabel('Number of cluster','fontsize',12)

%
[C,I]=max(Cl);
threshold_max=threshold(I);

A=wf1;
A(A<threshold_max*10^9)=0; % threshold

X=[];
Y=[];
Z=[];

for layer=65:num
A(:,:,layer)=im2bw(A(:,:,layer),0); % Make the binary image
[row,col]=find(A(:,:,layer));
X=[X;col];
Y=[Y;row];
Z=[Z;layer*ones(numel(row),1)];
end


[IDX,type]=dbscan([X,Y,Z],2,2);
clust=max(IDX);
```

```
%%
figure
for i=1:clust
scatter3(X(IDX==i),Y(IDX==i),Z(IDX==i),25,[rand rand rand],'filled')
axis([0 60 0 60 0 num])
daspect([1 1 50/15])
grid on
hold on
end
Center=mean([X,Y]);

% Stem of the tree
  maxheight = max(Z);
  nPoints = 8;
  [x,y,z] = cylinder([maxheight/200; maxheight/600], nPoints);
  z = (z+0.2)/1.2 * maxheight; % tree 2

  stem.Vertices = [x(:)+Center(1),y(:)+Center(2),z(:)];
  stem.Faces = convhulln(stem.Vertices);
  handles.Stem =
trisurf(stem.Faces,stem.Vertices(:,1),stem.Vertices(:,2),stem.Vertices(
:,3),2,...
                  'FaceColor',[0.5, 0.4, 0.2],...
                  'EdgeColor','none','FaceLighting','gouraud');

  light
  set(gcf, 'Renderer', 'OpenGL');
  %view(0,0);
  %set(gca,'Visible','off');
  %set(gcf, 'color', 'black');
  axis([0 60 0 60 0 num])
  daspect([1 1 50/15])
 %
clear x0_all x1_all y0_all y1_all z0_all z1_all
for i=1:clust

px=X(IDX==i);
py=Y(IDX==i);
pz=Z(IDX==i);

[C1,I1]=min((px-Center(1)).^2+(py-Center(2)).^2);
[C2,I2]=max((px-Center(1)).^2+(py-Center(2)).^2);

[B,IX]=sort((px-Center(1)).^2+(py-Center(2)).^2);
t=numel(IX);

x0=px(IX(1));
y0=py(IX(1));
z0=pz(IX(1));

x1=px(IX(t));
y1=py(IX(t));
z1=pz(IX(t));

hold on
light
```

```
%line([x0;x1],[y0;y1],[z0;z1],'LineWidth',3,'Color',[0.3, 0.2, 0.1])
x0_all(i)=x0;
x1_all(i)=x1;
y0_all(i)=y0;
y1_all(i)=y1;
z0_all(i)=z0;
z1_all(i)=z1;
end

d=((x0_all-x1_all).^2+(y0_all-y1_all).^2).^0.5;
d0=((x0_all-Center(1)).^2+(y0_all-Center(2)).^2).^0.5;
d1=((x1_all-Center(1)).^2+(y1_all-Center(2)).^2).^0.5;

xyz_branch=[];
z_branch=[];
for i=1:clust
  % Find the longest branches and extend them to the stem
  v0=[x0_all(i)-Center(1), y0_all(i)-Center(2)];
  v1=[x1_all(i)-Center(1), y1_all(i)-Center(2)];
  angle=acosd((v0*v1')/norm(v0)/norm(v1));
if d(i)>max(d)*0.1 & angle<45 & z0_all(i)<=z1_all(i) %for leaf-on
line([x0_all(i);x1_all(i)],[y0_all(i);y1_all(i)],[z0_all(i);z1_all(i)],
'LineWidth',3,'Color',[0.3, 0.2, 0.1])
  ratio=((x0_all(i)-Center(1)).^2+(y0_all(i)-
Center(2)).^2)^0.5/((x1_all(i)-Center(1)).^2+(y1_all(i)-
Center(2)).^2)^0.5;
  z0_temp=(ratio*z1_all(i)-z0_all(i))/(ratio-1);
  hold on
  if (z0_temp>0 & z0_temp<=z0_all(i))

line([Center(1),x0_all(i)],[Center(2),y0_all(i)],[z0_temp,z0_all(i)],'L
ineWidth',3,'Color',[0.3, 0.2, 0.1])
xyz_branch=[xyz_branch; [x1_all(i)-Center(1),y1_all(i)-
Center(2),z1_all(i)-z0_temp]];
  z_branch=[z_branch;z0_temp];
  end
  hold on
  else
index=find(d1<d0(i) & z1_all<z0_all(i));
  [C3,I3]=min((x1_all(index)-x0_all(i)).^2+(y1_all(index)-
y0_all(i)).^2+(z1_all(index)-z0_all(i)).^2);
  temp_x=x0_all(index);
  temp_y=y0_all(index);
  temp_z=z0_all(index);
   hold on
 end

end
close all
```

REFERENCES

[1] F. Ackermann, "Airborne laser scanning – present status and future expectations," *Journal of Photogrammetry and Remote Sensing*, vol. 54, pp. 64-67, 1999.

[2] A. Wehr, U. Lohr, "Airborne laser scanning - an introduction and overview," *Journal of Photogrammetry and Remote Sensing*, vol. 54, pp. 68-82, 1999.

[3] E. Baltsavias, "Airborne laser scanning: existing systems and firms and other resources," *Journal of Photogrammetry and Remote Sensing*, vol. 54, pp. 164-198, 1999.

[4] E. Bradley, D. Roberts, K. Roth, G. Parker, "Forest Vertical Structure from Discrete Lidar, LVIS, and the Idea Tree Distribution Model," *American Geophysical Union, Fall Meeting,* 2008.

[5] X. Sun, P, Jester, J. Abshire and E. Chang, "Performance of the GLAS Space Lidar Receiver through its Seven-Year Space Mission," *in CLEO:2011 - Laser Applications to Photonic Applications, OSA Technical Digest (CD) (Optical Society of America, 2011), paper ATuA2.*

[6] Naidoo L., M.A. Cho, R. Mathieu and G. Asner, " Classification of savanna tree species, in the Greater Kruger National Park region, by integrating hyperspectral and LiDAR data in a Random Forest data mining environment ", *ISPRS Journal of Photogrammetry and Remote Sensing* 69: 167-179, 2012.

[7] Myburgh, H.C., J.C. Olivier, R. Mathieu, K. Wessels, B. Leblon, G. Asner, and J. Buckley, " SAR-to-LiDAR mapping for tree volume prediction in the Kruger National Park. Proceedings of the International Geoscience and Remote Sensing Symposium, Vancouver, 2011.

[8] A. Sampath, J. Shan, "Segmentation and Reconstruction of Polyhedral Building Roofs From Aerial Lidar Point Clouds," *IEEE Transactions on Geoscience and Remote Sensing*, vol. 48, iss. 3, part. 2, pp. 1554-1567, 2010.

[9] J. Han, "A Noniterative Approach for the Quick Alignment of Multistation Unregistered LiDAR Point Clouds," *IEEE Geoscience and Remote Sensing Letters*, vol. 7, iss. 4, pp. 727-730, 2010.

[10] B. Gorte, N. Pfeifer, "3D Image Processing to Reconstruct Trees from Laser Scans." *Photogrammetry and Remote Sensing*, TUdelft.

[11] J. Binney, G. Sukhatme, "3D Tree Reconstruction from Laser Range Data," *Proceedings - IEEE International Conference on Robotics and Automation*, pp. 1321-1326, 2009.

[12] E. Baltsavias, "Airborne laser scanning: Basic relations and formulas," *Journal of Photogrammetry and Remote Sensing*, vol. 54, pp. 199-214, 1999.

[13] C. Brenner, "Airborne laser scanning," *ISPRS, International Summer School " Digital Recording and 3D Modeling"*, Greece, April 24-29, 1999.

[14] C. Hug, A. Ullrich, and A. Grimm, "Litemapper-5600: A waveform-digitizing Lidar terrain and vegetation mapping system," *International Archives of Photogrammetry, Remote Sensing and Spatial Information Sciences*, vol. XXXVI-8/W2, pp. 24-29, 2004.

[15] C. Mallet, F. Bretar, "Full-waveform topographic lidar: State-of-the-art," *Journal of Photogrammetry and Remote Sensing*, vol. 64, iss. 1, pp. 1-16, 2009.

[16] C. Hug, A. Ullrich, and A. Grimm, "Litemapper-5600: A waveform-digitizing Lidar terrain and vegetation mapping system," *International Archives of Photogrammetry, Remote Sensing and Spatial Information Sciences*, vol. XXXVI-8/W2, pp. 24-29, 2004.

[17] G. Sun, K. Ranson, "Modeling LiDAR returns from forest canopies," *IEEE Transactions on Geoscience and Remote Sensing*, vol. 38, no. 6, pp. 2617-2626, 2000.

[18] B. Jutzi, U. Stilla, "Range determination with waveform recording laser systems using a Wiener Filter," *ISPRS Journal of Photogrammetry & Remote Sensing*, vol. 61, pp. 95-107, 2006.

[19] W. Wagner, A. Ullrich, V. Ducic, T. Melzer, and N. Studnicka, "Gaussian decomposition and calibration of a novel small-footprint full-waveform digitizing airborne laser scanner," *ISPRS Journal of Photogrammetry & Remote Sensing*, vol. 60, pp. 100-112, 2006.

[20] S. Kotchenova, N. Shabanov, Y. Knyazikhin, A. Davis, R. Dubayah, and R. Myneni, "Modeling LiDAR waveforms with time-dependent stochastic radiative transfer theory for remote estimations of forest structure," *Journal of geophysical research*, vol. 108, pp. 4484, 2003.

[21] Y. Kraftmakher, “Noise Reduction by Signal Accumulation,” *The Physics Teacher*, vol. 44, pp. 528-530, 2006.

[22] H. Okumura, T. Sugita, H. Matsumoto, N. Takeuchi, “Noise reduction method for lidar echo data based on multivariate analysis method,” *IEEE Geoscience and Remote Sensing Symposium*, vol. 2, pp. 454-456, 1993.

[23] N. Wiener, “Extrapolation, Interpolation, and Smoothing of Stationary Time Series,” *MIT Press*, Cambridge, MA, 1949.

[24] L. Nordin, “Analysis of Waveform Data from Airborne Laser Scanner Systems,” Master thesis, Lulea University of Technology, 2006. (http://epubl.ltu.se/1402-1617/2006/336/LTU-EX-06336-SE.pdf)

[25] L. B. Lucy, “An iterative technique for the rectification of observed distributions,” *The Astronomy Journal*, vol. 79, no. 6, pp. 745-754, 1974.

[26] S. *Silvilaser*, and R. Reuter, “Stable deconvolution of noise lidar signal,” *Proceedings of EARSel-SIG-Workshop LIDAR*, no. 1, pp. 88-95, 2000.

[27] C. L. Lawson, and R. J. Hanson, “Solving least squares problems,” *Prantice Hall Series in Automatic Computation (Prantice Hall)*, pp. 160-165, 1974.

[28] L. B. Lucy, “An iterative technique for the rectification of observed distributions,” *The Astronomy Journal*, vol. 79, no. 6, pp. 745-754, 1974.

[29] A. Persson, U. Soderman, J. Topel, S. Alberg, “Visualization and analysis of full-waveform airborne laser scanner data,” *ISPRS WG III/3, III/4, V/3 Workshop,* pp. 103-108, 2005.

[30] A. Roncat, G.Bergauer, and N. Pfeifer. “Retrieval of the backscatter cross-section in full-waveform lidar data using b-splines,” *International Archives of Photogrammetry, Remote Sensing and Spatial Information Sciences,* vol. 38 (Part 3B), pages 137-142, Saint-MandeÅL, France, 2010.

[31] A. Chauve, C. Mallet, F. Bretar, S. Durrieu, M. Pierrot-Deseiligny, and W. Puech, “Processing full waveform lidar data: modeling raw signals,” *International Archives of Photogrammetry, Remote Sensing and Spatial Information Sciences*, vol. 39 (part3/w52), pp. 102-107, Espoo, Finland, 2007.

[32] D. Marquardt, “An algorithm for least-squares estimation of nonlinear parameters,” *Journal of the Society for Industrial and Applied Mathematics,* vol. 11, no. 2, pp. 431-441, 1969.

[33] A. Dempster, N. Laird, D. Rubin, “Maximum likelihood from incomplete data via the EM algorithm,” *Journal of the Royal Statistical Society,* vol. 39, no. 1, pp. 1-38, 1977.

[34] P. Green, “Reversible jump Markov chain Monte-Carlo computation and Bayesian model determination,” *Biometrika,* vol. 82, no. 4, pp. 711-732, 1995.

[35] J. Cote, J. Widlowski, R. Fournier, M. Verstraete, “The structural and radiative consistency of three-dimensional tree reconstructions from terrestrial lidar,” *Remote Sensing of Environment*, vol. 113, pp. 1067-1081, 2009.

[36] J. Rosette, P. North, and J, Suarez, “Vegetation height estimates for a mixed temperate forest using satellite laser altimetry,” *International Journal of Remote Sensing*, vol. 29, no. 5, pp. 1475-1493, 2008.

[37] A. Farid, D. Goodrich, R. Bryant, and S. Sorooshian, “ Using airborne LiDAR to predict Leaf Area Index in cottonwood trees and refine riparian water-use estimates,” *Journal of Arid Environments*, vol. 72, pp. 1-15, 2008.

[38] J. Anderson, M. E. Martin, M-L. Smith, R. O. Dubayah, M. A. Hofton, P. Hyde, B. E. Peterson, J. B. Blair, and R. G. Knox, “The use of waveform lidar to measure northern temperate mixed conifer and deciduous forest structure in New Hampshire,” *Remote Sensing of Environment*, vol. 105, no. 3, pp. 248-261, 2005.

[39] A. Collin, P. Archambault, B. Long, “Mapping the Shallow Water Seabed Habitat With the SHOALS,” *IEEE Transactions on Geoscience and Remote Sensing*, vol. 46, iss. 10, pp. 2947-2955, 2008.

[40] S. Pe’eri, and W. Philpot, “Increasing the Existence of Very Shallow-Water LIDAR Measurements Using the Red-Channel Waveforms,” *IEEE Transactions on Geoscience and Remote Sensing*, vol. 45, no. 5, pp. 1217-1223, 2007.

[41] L. Muncina, M. Rutherford, L. Powrie, “The logic of the map: approaches and procedures.” In: Muncina, L., Rutherford, M.C. (Eds.), *The vegetation of South Africa, Lesotho and Swaziland*. Strelitzia, Cape Town, pp. 14-18, 2006.

[42] J. Wu, J.A.N. van Aardt and G. Asner, "A Comparison of Signal Deconvolution Algorithms Based on Small-Footprint LiDAR Waveform Simulation," *IEEE Transactions on Geoscience and Remote Sensing*, vol. 49, iss. 6, pp. 2402-2414, 2011.

[43] J. Wu, J.A.N. van Aardt, J McGlinchy and G. Asner, "A Robust Signal Preprocessing Chain for Small-Footprint Waveform LiDAR," *IEEE Transactions on Geoscience and Remote Sensing*, vol. 50, no. 8, pp. 3242-3255, 2012.

[44] F. Venter, R. Scholes, H. Eckhardt, "The abiotic template and its associated vegetation pattern." In: Du Toit, J., Biggs, H., Rogers, K.H. (Eds.), *The Kruger experience: Ecology and management of savanna heterogeneity*. Island Press, London, pp. 83-129, 2003.

[45] L. Muncina, M. Rutherford, L. Powrie, "The logic of the map: approaches and procedures." In: Muncina, L., Rutherford, M.C. (Eds.), *The vegetation of South Africa, Lesotho and Swaziland*. Strelitzia, Cape Town, pp. 14-18, 2006.

[46] Arbaro: an open source tree generation software http://arbaro.sourceforge.net (Last access: Jan 15th, 2011).

[47] Blender: an open source 3-D rendering software http://www.blender.org/ (Last access: Jan 15th, 2011).

[48] J. Wu, J.A.N. van Aardt, G. P. Asner, R. Mathieu, T. Kennedy-Bowdoin, D. Knapp, K. Wessels, B.F.N. Erasmus, and I. Smit, "Connecting the dots between laser waveform and herbaceous biomass for assessment of land degradation using small-footprint waveform lidar data," *IEEE International Geoscience & Remote Sensing Symposium*, vol. II, pp. 334-337, Cape Town, South Africa, 2009.

[49] I. T Jolliffe, *Principal Component Analysis*, *Springer Series in Statistics*, *2nd ed*., Springer, NY, XXIX, 487 p.28, 2002.

[50] S.Theodoridis and K. Koutroumbas, *Pattern Recognition*, 3rd ed. San Diego, CA: Academic, ch.2, pp. 13-20. 2006.

[51] R. Sibson, "A brief description of natural neighbor interpolation," *In V. Barnett. Interpreting Multivariate Data.* Chichester: John Wiley, ch. 2, pp. 21–36, 1981.

[52] Natural neighbor. http://en.wikipedia.org/wiki/Natural_neighbor (Last access: Aug 26th, 2011).

[53] M. L. Stein, *Statistical Interpolation of Spatial Data: Some Theory for Kriging*, Springer, New York, 1999.

[54] C. Harman, M. Johns, "Voronoi Natural Neighbors Interpolation," http://www.cs.swarthmore.edu/~adanner/cs97/s08/papers/harman_johns.pdf, (Last access: Jan 15th, 2011)

[55] R. Yuhas, AFH. Goetz, J. Boardman, "Discrimination Among Semi-Arid Landscape Endmembers Using Spectral Angle Mapper (SAM) Algorithm," *Summaries of the 4th Annual JPL Airborne Geoscience Workshop*, JPL Pub-92-14, AVIRIS Workshop. Jet Propulsion Laboratory, Pasadena, CA, pp. 147-150, 1992.

[56] F. Wilcoxon. Individual comparisons by ranking methods. *Biometrics*, vol. 1, pp. 80-83, 1945.

[57] J. McGlinchy, J. van Aardt, H. Rhody, J. Kerekes, E. Ientilucci, G. Asner, D. Knapp, R. Mathieu, T. Kennedy-Bowdoin, B. Erasmus, K. Wessels, I. Smit, J. Wu, and D. Sarrazin, "Extracting Structural Land Cover Components Using Small-footprint Waveform Lidar Data," *IEEE Geoscience and Remote Sensing Symposium*, pp. 1976-1979, 2010.

[58] J. McGlinchy, "Extracting Structural Vegetation Components from Small-Footprint Waveform LiDAR Data in a Savanna Ecosystem," *Master's thesis*, Center for Imaging Science, Rochester Institute of Technology, 56 Lomb Memorial Drive, Rochester, NY 14623, USA, August, 2010.

[59] [Online Available]:http://www.mathworks.com/matlabcentral/ fileexchange/19084-region-growing

[60] J. Wu, J.A.N. van Aardt, G.P. Asner, T. Kennedy-Bowdoin, D. Knapp, B.F.N. Erasmus, R. Mathieu, K. Wessels, and I.P.J. Smit, 2009. "LiDAR waveform-based woody and foliar biomass estimation in savanna environments," Peer-reviewed proceedings: *Silvilaser 2009 - 9th International Conference on Lidar Applications for Assessing Forest Ecosystems*, October 14-16, 2009, College Station, TX, 10p.

[61] J. K. Vanclay, *MODELLING FOREST GROWTH AND YIELD, Application to Mixed Tropical Forests*, CAB INTERNATIONAL, 1994.

[62] G. Asner. R.F. Hughes, T.A. Varga, D.E. Knapp, and T. Kennedy-Bowdoin, 2009. Environmental and Biotic Controls over Aboveground Biomass Throughout a Tropical Rain Forest. *Ecosystems* 12:261-278

[63] J. MacQueen, " Some methods for classification and analysis of multivariate observations", *Proceedings of 5th Berkeley Symposium on Mathematical Statistics and Probability*. University of California Press. pp. 281-297.

[64] R.T. Ng, and J. Han, "Efficient and effective clustering methods for spatial data mining", *Proc. 20th Int. Conf. on Very Large Data Bases*, pp. 144-155, Santiago, Chile.

[65] J. A. Garcia., J. Fdez-Caldivia, F. J. Cortijo., and R. Molina, " A dynamic approach for clustering data", *Signal Processing*, vol. 44, no. 2, pp. 181-196, 1994.

[66] M Ester, H-P. Kriegel, J. Sander, X. Xu, " A density-based algorithm for discovering clusters in large spatial databases with noise", *Proceedings of 2nd international conference on knowledge discovery and data mining,* KDD-96. Pp.226-231, 1996.

[67] [Online Available]: http://code.google.com/p/dmfa07/ downloads /detail ?name= DBSCAN.M

[68] [Online Available]: http://en.wikipedia.org/wiki/File:DBSCAN-density-data.svg

[69] Q. Chen, D. Baldocchi, P. Gong, and M. Kelly, "Isolating individual trees in a savanna woodland using small footprint lidar data", *Photogrammetric Engineering & Remote Sensing*, vol. 72, no.8, pp. 923-932, 2006

[70] J. Mitchell, N. Glenn, T. Sankey, D. Derryberry, M. Anderson and R. Hruska, "Small-footprint lidar estimations of sagebrush canopy characteristics", *Photogrammetric Engineering & Remote Sensing*, vol. 77, no.5, pp. 000-000, 2011

[71] D. Zimble, D. Evans, G. Carlson, R. Parker, S. Grado, P. Gerard, "Characterizing vertical forest structure using small-footprint airborne lidar", *Remote sensing of Environment*, vol. 87, pp. 171-182, 2003.

[72] R. Burton, J. R. Schott and S. D. Brown, "Elastic LADAR Modeling for Synthetic Imaging Applications," *Proc SPIE*, vol. 4816, pp. 144-155, 2002.

[73] S. D. Brown, D. Blevins and J. R. Schott, "Time-gated topographic LIDAR scene simulation," *Proc SPIE*, vol. 5791, pp. 342-353, 2005.

[74] N. Metropolis and S. Ulam, "The Monte Carlo Method," *Journal of the American Statistical Association*, vol. 44, no. 247, pp. 335-341, 1949.

[75] Carnegie Airborne Observatory. http://cao.stanford.edu/?page=cao_systems (Last access: Jan 15th, 2011).